Mask Edge Eff ects in Optical Lithography and Chip Level Modeling Methods

Marshal Miller

Electrical Engineering and Computer Sciences
University of California at Berkeley

Technical Report No. UCB/EECS-2010-160
http://www.eecs.berkeley.edu/Pubs/TechRpts/2010/EECS-2010-160.html

December 16, 2010

Copyright © 2010, by the author(s).
All rights reserved.

Permission to make digital or hard copies of all or part of this work for personal or classroom use is granted without fee provided that copies are not made or distributed for profit or commercial advantage and that copies bear this notice and the full citation on the first page. To copy otherwise, to republish, to post on servers or to redistribute to lists, requires prior specific permission.

Mask Edge Effects in Optical Lithography and Chip Level Modeling Methods

by

Marshal Miller

A dissertation submitted in partial satisfaction of the

requirements for the degree of

Doctor of Philosophy

in

Electrical Engineering

in the

Graduate Division

of the

University of California, Berkeley

Committee in charge:

Professor Andrew R. Neureuther, Chair
Professor Eli Yablonovitch
Professor James Graham

Fall 2010

The dissertation of Marshal Miller, titled Mask Edge Effects in Optical Lithography and Chip Level Modeling Methods, is approved:

Chair ______________________________ Date ______________

______________________________ Date ______________

______________________________ Date ______________

University of California, Berkeley

Mask Edge Effects in Optical Lithography and Chip Level Modeling Methods

Copyright 2010
by
Marshal Miller

Abstract

Mask Edge Effects in Optical Lithography and Chip Level Modeling Methods

by

Marshal Miller

Doctor of Philosophy in Electrical Engineering

University of California, Berkeley

Professor Andrew R. Neureuther, Chair

This dissertation presents a full framework for modeling transmission effects due to three-dimensional mask topography in optical lithography from solving Maxwell's equations using rigorous simulation through fast-CAD for full chip level aerial image quality characterization in optical projection printing. As the semiconductor industry advances to the 22nm technology node where features are sub-wavelength, lithography imaging must be accurate to the nanometer. Non-ideal transmission caused by scattering off of mask edges has become an increasingly important source of inaccuracies in lithography modeling. Here mask edge effects are treated in two modules: modeling the near field scattering phenomena and then moving that information into fast-CAD first cut accurate simulation.

Phase errors induced by mask edges lead to an asymmetric behavior through focus, which when combined with polarization dependent effects lead to significant loss in the process window. Phase shifting masks, leveraging image benefits of 0° and 180° transmission, further complicate the interplay of partial signal delay and the resulting complex phase errors. It is shown that for even conservative imaging scenarios up to 40% of the focus latitude is lost.

Two methods for characterizing this scattering induced by mask edges are introduced. The first is an experimental approach, which uses gratings to characterize the polarization dependent magnitude of these errors as might be utilized in an inexpensive mask monitoring apparatus. The second method examines the direct near field behavior with simulation, leading to more accurate phase information as well as guidelines for edge-to-edge cross-talk. A MoSi attenuating 180° phase shift mask was characterized in detail, with boundary layer values of about 20 nm ($1/10\ \lambda$) in mask dimensions even for high off-axis illumination. Non-attenuating chromeless masks and complicated mask stacks such as $TaSiO_2$ showed significant electromagnetic errors as high as $1/4\ \lambda$, suggesting that they are not viable for advanced lithography applications. Further, a study of a hypothetical thin phase shifting mask showed that the phase error effects is inherent to the use of neighboring phase wells, and cannot be remedied by material improvements.

The most significant contribution of this dissertation is the development of Source-Pupil Kernel Convolution with Pattern Matching (SP-KCPM) that connects the information gained from boundary layer modeling to fast-CAD pattern matching tools, achieving a 10^4 speedup compared to conventional imaging. SP-KCPM is built on a computational engine

developed by Frank Gennari that optimizes the process of pixel based multiplication of a target pattern across large layouts. The degree of similarity is then used in SP-KCPM to estimate aerial image values. Full complex interactions are included, and along with a pupil-based framework enables more general imaging by including additional phenomena such as defocus, zernike aberrations, measured aberrations, and potentially resist and polarization effects without needing separate kernels or algebraic perturbations. Since the pupil calculation is generated automatically and can combine many effects, the need for deriving and confounding multiple physical phenomena has been eliminated. Proximity effects between features are also accounted for, removing the need for a prior image calculation or restrictions to a specific image contour. A new coherent source model combined with source splitting is used to generalize the aerial image quality assessment to distributed off-axis sources utilized in advanced resolution enhancement techniques.

This distributed source-pupil based convolution method has guaranteed impressive accuracy well beyond that historically reported for kernel convolution pattern matching methods at full chip speeds, thus enabling many new applications. Careful implementation considerations such as pattern size, gridding, normalization, and source clustering guided the development of a very accurate system. For various sources, dipole, annular, quad, and pixelated optimized sources, R^2 correlation is shown to be above 0.99. Additionally, effects of defocus, zernike aberrations, background aberrations, and asymmetric sources have all been shown to be accurate.

As an example of new applications, SP-KCPM was tested on highly pixelated sources used in source-mask-optimization, and accuracy of $R^2 = 0.99$ was achieved on general layouts by splitting the source into 12 regions. This capability is used to demonstrate the ability to make decisions between source distributions and mask blanks. Realtime tracking of mask changes facilitates further applicability in optical proximity correction is sufficiently fact for interoperability as part of an optimization scheme. Hotspot detection is used to quickly make decisions between sources or mask types by assessing the impact an optimized source solution over a larger non-optimized layout region. Real time tracking of mask changes opens the door for SP-KCPM to be used for optimization techniques and optical proximity correction (OPC). SP-KCPM is shown to be a general tool, useful wherever fast imaging is at a premium with applicability in many forms of optical imaging such as inspection and character recognition, in addition to standard projection printing.

To My Parents

Contents

List of Figures v

List of Tables vii

1 Introduction 1
- 1.1 Motivation . . . 1
- 1.2 Problem . . . 2
- 1.3 Major Thesis Contributions . . . 3
- 1.4 Thesis Structure . . . 3

2 Background 5
- 2.1 Evolution of Lithography and its Challenges . . . 5
- 2.2 Lithography Simulation Overview . . . 6
  - 2.2.1 Rigorous Numerical Solution for Maxwell's Equations . . . 6
  - 2.2.2 Aerial Imaging . . . 6
- 2.3 Electromagnetic Effects in Photomask Transmission . . . 7
  - 2.3.1 Intensity Imbalance . . . 7
  - 2.3.2 Modeling . . . 8
- 2.4 Kernel Convolution with Pattern Matching . . . 10
  - 2.4.1 Pattern Matching . . . 10
  - 2.4.2 Conclusions . . . 12

3 Image Tilt Through Focus 13
- 3.1 Rigorous Simulations Demonstrate Through-Focus Asymmetry . . . 13
  - 3.1.1 CD Change for Line Ends and Edges . . . 13
  - 3.1.2 CD Change for Features with a Jog . . . 14
- 3.2 Impact on Imaging Through Focus with Thin Mask Model . . . 16
  - 3.2.1 Low Numerical Aperture Normalized Isolated and Dense Lines . . . 17
  - 3.2.2 193nm Wavelength Isolated and Dense Lines . . . 17
- 3.3 Conclusions . . . 20

4 Method for Experimental Characterization of EMF Effects 21
- 4.1 Grating Based Calibration Method . . . 21
- 4.2 On-axis Simulation Data . . . 24

4.2.1 Chromeless Alternating Phase Shift Mask 25
4.2.2 MoSi Attenuating Phase Shift Mask 25
4.2.3 Summary of On-Axis Edge Contributions 26
4.3 Off-axis Simulation Data 26
4.3.1 Chromeless Alternating Phase Shift Mask 27
4.3.2 MoSi Attenuating Phase Shift Mask 27
4.4 Alternate Mask Stacks 29
4.5 Conclusions 30

5 Simulation Based Modeling of Mask EMF Effects 33
5.1 Direct field Analysis Methodology 34
5.1.1 MoSi Phase Shift Mask Data 34
5.2 Cross-Talk Guidelines 35
5.3 Alternate Mask Stacks 37
5.3.1 Ultra Thin MoSi 37
5.3.2 Thin Binary 39
5.4 Near Field Effects for 3D Corners 39
5.5 Conclusions 40

6 Source-Pupil Kernel Convolution with Pattern Matching 42
6.1 Automatic Kernel Generation for General Mask, Pupil, and Source 43
6.1.1 Complex Mask Transmission 43
6.1.2 Generalizing and Automating Pupil Function Formulation 44
6.1.3 Generic Source Distribution 45
6.2 Novel Formulation for Intensity Estimation with SP-KCPM 47
6.2.1 Calculating Intensity 48
6.2.2 Calculating Change in Intensity 49
6.2.3 Spillover vs. Spillback 49
6.3 SP-KCPM Examples 50
6.3.1 Defocus with Top-Hat Illumination 51
6.3.2 Coma with off-axis illumination 51
6.3.3 Dipole with Background Aberrations 54
6.4 Conclusions 58

7 Source-Pupil Kernel Convolution for General Source Distributions 59
7.1 Calibration Examples 59
7.1.1 Off-axis Illumination 60
7.1.2 Effect of Partial Coherence 60
7.2 Limitation of Coherent Source Assumption 62
7.3 Source Splitting: Hybrid Abbe SP-KCPM 63
7.3.1 Revisit Dipole 65
7.3.2 Annular Illumination: Breakdown vs Normal 67
7.4 Conclusions 67

8 Applications of SP-KCPM **70**
8.1 Application: Evaluating SMO Source Effects on Non-optimized Layouts . . . 70
8.2 Source and Mask Blank Decision Making 72
8.3 Application: Tracking Image Quality with Mask Changes 73
8.4 Application: Tracking Image Quality with Mask Changes 74
8.5 Conclusions 75

9 Conclusions **76**

Bibliography **78**

List of Figures

1.1 Overview of Mask Edge Error . . . 2

2.1 Intensity Imbalance for Alternating Phase Shifting Mask . . . 7
2.2 Example of Domain Decomposition for a 1-D Mask Pattern . . . 8
2.3 Piecewise Deconstruction for Edge DDM . . . 9
2.4 Boundary Layers used to Model Rigorous Transmission . . . 9
2.5 Asymmetry Factor for Calibrating Boundary Layers . . . 10
2.6 Fourier Transform of Zernike Polynomials as Match Patterns . . . 11

3.1 Aerial Image of MoSi Line . . . 14
3.2 CD Data for MoSi Line . . . 15
3.3 Aerial Image of MoSi Jog . . . 15
3.4 CD Data for MoSi Jog . . . 16
3.5 LES for Isolated and Dense Patterns with BLs . . . 18
3.6 LES vs Defocus for Several BL phases . . . 19

4.1 Field Transmission for Chromeless PSM . . . 22
4.2 Grating Based Experimental Methodology . . . 23
4.3 Example of Grating Based Boundary Layer Calibration . . . 24
4.4 On-axis CPL BL Data . . . 25
4.5 On-axis MoSi BL Data . . . 26
4.6 Off-axis CPL Transmission . . . 28
4.7 Off-axis CPL BL Data . . . 28
4.8 Off-axis MoSi Transmission . . . 29
4.9 Off-axis MoSi BL Data . . . 30
4.10 $TaSiO_2$ 0th Order Transmission Data . . . 31
4.11 Field Comparison of MoSi and $TaSiO_2$ . . . 31

5.1 Transmission Intensity and Field vs. Duty Cycle for MoSi Att-PSM . . . 34
5.2 MoSi 0th Order Transmission for Pitch = 200, 400, 1000nm . . . 36
5.3 TE and TM Field Transmission for MoSi Att-PSM . . . 37
5.4 MoSi Compared to Ultra Thin Material . . . 38
5.5 Line End Field Data . . . 40
5.6 Boundary Layer Modeling Schemes . . . 40

6.1 Boundary Layers for KCPM 43
6.2 Typical Pupil Functions 44
6.3 Source and source dependent point response for SP-KCPM 45
6.4 SP-KCPM Block Diagram 48
6.5 Spillover vs. Spillback 50
6.6 45nm Test Pattern. 51
6.7 Source, Pupil, and Influence Functions for Defocus Example 52
6.8 Correlation Data for Defocus Example 53
6.9 Source, Pupil, and Influence Functions for Coma Example 54
6.10 Correlation Data for Coma Example 55
6.11 Source, Pupil, and Influence Functions for Dipole Example 56
6.12 Correlation Data for Dipole Example 57

7.1 Source configurations for off-axis calibration. 60
7.2 Off-Axis Calibration Data 61
7.3 Source configurations for on-axis coherence calibration. 61
7.4 Coherence Calibration Data 62
7.5 Linear Phase Results in Error for Coherence Assumption 64
7.6 Point Response for Several Sources Compared to Airy Function 64
7.7 90 Degree Phase Length vs. Pixel Location 65
7.8 Correlation Data for Dipole Source Splitting Example 66
7.9 Source with Split Configurations for Annular Illumination 67
7.10 Correlation Data for Annular Source Splitting Example 68

8.1 Metal 1 Design Target 71
8.2 Correlation Data for SMO Source 71
8.3 Using Hotspot Detection for Source Decision Making 72
8.4 Quadrapole Source with Split Configuration 73
8.5 Using SP-KCPM to Track a Changing Mask 74

List of Tables

4.1 BL Data for CPL and MoSi mask Blanks 27

5.1 BL Data for MoSi Bask Blanks 34

Acknowledgments

It is hard to put into words the impact that my advisor Professor Andrew R. Neureuther has had on my graduate education, career, and life in general. I find it difficult to imagine getting to this point without his enthusiasm, insight, and overall brilliance. Even in retirement, Andy always had time for meetings in between painting lessons and photography in the backcountry. He always had too many ideas to ever address them all, and each meeting seemed to come up with more questions than it answered.

My colleagues in the Neureuther group, past and present, have had a profound influence on my experience at Berkeley. Though Bob Socha, Kostas Adam, Frank Gennari and Tom Pistor had gradated by the time I arrived, their work and continued contact provided motivation and tools for my research. Michael Lam, Greg McIntyre, and Wojtek Poppe had one foot out the door when I arrived, but helped me get going when I first joined the group, and provided valuable insight from the working world. Dan Cepereley was invaluable in decoding Andy's handwriting and showing me the ropes, whether running simulations, climbing, or playing ultimate frisbee. I spent most of my graduate career with Juliet Rubinstein, Eric Chin, Chris Clifford, and Lynn Wang, whose friendship, support, and difficult questions helped me make it through to the end.

Kenji Yamazoe's lithography expertise was an invaluable addition to our group. In his two short years as a visiting scholar from Canon Inc., Kenji was always able to ask the right questions, provide the right insight, and have the right piece of code ready to get our ideas moving quickly. Having Kenji around was like having a second research advisor in the office.

I made many contacts in industry through the IMPACT grant and interactions at SPIE conferences. I spent two summers at IBM working with the computational lithography group with Alan Rosenbluth, David Melville, Jaione Tirapu-Azpiroz, Kehan Tian and many others, which gave me a great deal of perspective and helped keep my work focused.

I would like to acknowledge the financial support over my graduate career. My early work on shot noise was funded on a DARPA grant. The work in this thesis was initially funded by the FLCC grant which was replaced by the IMPACT grant. Both were part of the UC Discovery project. Support for my final year was also provided by an IBM Ph.D. Fellowship.

In addition to my colleagues, I would like to thank my friends at Berkeley for pushing me to always explore and expand my comfort zone. Thanks to my roommates at CopaColusa for creating a great place to live. There are too many people to list, but for the climbing trips, afternoon tennis, IM basketball, and travel adventures, thank you for making life so exciting, and never letting me slow down.

Most importantly, to my parents, sister, grandparents and other close family members, thank you for your love and support. Your confidence in me was always there when I needed it to keep pushing for this goal. To Belinda, for always being there for me, and bringing out the best in me. Though I loved my time at Berkeley, it will be great being back on the east coast, close to home.

Chapter 1

Introduction

1.1 Motivation

The goal of this thesis is to extend lithography modeling to include non-idealities from photomask transmission in fast-CAD technologies suitable for full chip design in semiconductor manufacturing. Standard simulation tools are accurate, but cannot keep up with the need to guarantee adequate image quality of every feature on a complete chip. Fast, accurate models are required, creating opportunities to extend existing techniques and develop new capabilities in an effort to close the gap between existing methods. Mask transmission irregularities due to 3-D mask topography have emerged as a significant additional source of image degradation, especially through focus, with no simple general model for design compensation. This dissertation proposes a framework which starts by modeling these transmission errors from Maxwell's equations and feeds this information upstream to accurate chip-level tools that are 10^4 faster than conventional imaging methods.

At the time of writing, 32nm features are being printed using 193nm wavelength optical lithography, with the 22nm technology node just around the corner. As devices become smaller, the lithography process must be accurate down to the nanometer to achieve high yield. As resolution enhancement techniques (RETs) have advanced, sources have become more complicated with high off-axis illumination carefully calibrated for specific design patterns, which in most cases have feature sizes below the wavelength of the incident illumination. The picture is further complicated by polarization and vector effects which are not included in a thin mask model. With smaller features, transmission errors caused by mask edges become more pronounced as less averaging takes place over well-behaving larger regions. It is important to be able to account for these mask edge effects in the presence defocus, aberrations, lens heating, and other physical phenomena that impact image fidelity.

With this aggressive scaling the behavior of mask structure due to its 3-D geometry becomes increasingly important. When mask features are large relative to the illumination wavelength, the mask transmission behavior can be handled in a relatively simple way by making approximations, mainly that the mask is infinitely thin. This thin mask approximation (TMA) allows for quick computation of a lithography image, however non-ideal transmission (Figure 1.1) caused by mask edges and phase wells are ignored. These be-

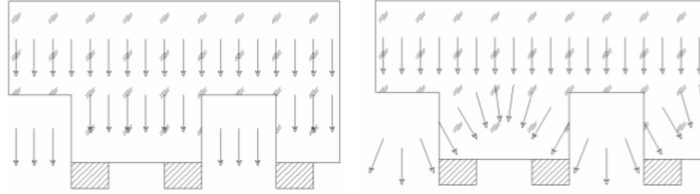

Figure 1.1: Left: Well behaved fields used for thin mask model. Right: More accurate picture of field behavior caused by phase wells. [29]

haviors can be calculated from rigorous simulation by solving Maxwell's equations, but this process requires 3-D simulation grids much smaller than feature sizes and analysis of the billion plus features on modern layouts is not possible. Thus mask modeling has entered a regime where simple models are no longer accurate, and rigorous models are too slow.

1.2 Problem

The overall problem that this dissertation addresses is how to connect and extend the communication between a rigorous electromagnetic field (EMF) analysis and a thin mask model in a new paradigm that accurately analyzes full-chip behavior. There are several well established layers of simulation. On the accurate, slow side of the spectrum is the rigorous solving of Maxwell's equations using Finite-Difference Time Domain (FDTD) or Finite Elements Method (FEM) simulation, which can be extremely accurate, but requires a lot of computational power. The middle ground is a thin mask model using Kirchoff imaging and assuming ideal mask transmission. This leaves out important 3-D field interactions, but is much faster than FDTD. The other extreme is pattern matching, which is a fast-CAD first cut accurate method that involves convolving a target pattern with a given layout and using the degree of similarity to gain some information about image behavior. The state of these methods will be discussed in further detail in Chapter 2.

The goal of this thesis is to increase the information flow between these levels of granularity and accuracy in simulation by taking the physical insight obtained from rigorous simulation and moving it all the way up to pattern matching, which is many orders of magnitudes faster. For example, FDTD could take days to run a layout the size of a few transistors, while pattern matching has been shown to run on an AMD processor layout with 200 million transistors in under an hour [25]. To facilitate this movement of physical information between simulation levels, the thesis is split into two main thrusts. The first is an attempt to bridge the gap between FDTD and thin mask aerial image using new polarization and cross-talk information in boundary layer modeling. The second step is to go from a more sophisticated thin mask model to pattern matching while retaining the physical information gained from rigorous simulation through a new formulation with increased accuracy.

1.3 Major Thesis Contributions

The main contribution of this thesis is a framework that builds from first principles and rigorous simulation up to full-chip aerial image estimation up to 10^4 time faster than conventional methods, with correlation with simulation with generalized transmission of 0.99. This is done in two separate modules. The first module closes the gap between rigorous simulation and aerial imaging by revisiting boundary layer modeling as a way for modeling mask edge transmission errors. This entails a look at the causes and consequences of phase transmission errors through rigorous simulation, which are shown to be as high as 20% of the entire feature to be exposed. In addition, an experimental method and a simulation based method are presented for pulling edge behaviors into a thin mask framework. Other authors have presented on edge modeling [1, 65] but here data is presented for new mask types as well as polarization, off-axis, and edge cross-talk behaviors.

The second module presents a revamped pattern matching algorithm, called Source-Pupil Kernel Convolution with Pattern Matching (SP-KCPM), that improves correlation with aerial image from about 0.90 to 0.99. This pupil-based framework allows for general consideration of any physical behavior that can be expressed as either a complex transmission on the mask or path difference in the pupil. This new algorithm also includes an initial field estimate, which removes any reliance on prior information or need for calibration. General sources are treated through source splitting allowing for full mask, source, and pupil generality. The kernel generation is fully automated and able to capture many effects and their interactions without requiring algebraic perturbations. The mask modeling component and SP-KCPM can be used separately, but together form a framework for calibrating the transmission errors of a mask blank, and taking those behaviors to full chip scale computation.

1.4 Thesis Structure

The original work in this dissertation addresses modeling rigorous scattering off of mask edges and getting that information accurately to full chip scale using pattern matching. Initially, the nature of mask edge scattering behaviors, the resulting transmission errors, and the consequences of phase errors of mask errors are evaluated through rigorous simulation in Chapter 3. The consequences on imaging are also calculated using a thin mask model to show the resulting loss of focus latitude.

Next, Chapter 4 provides a simulation-based, but an experimental friendly, approach for calculating the magnitude of edge effects for a particular mask type using grating structures with the goal of quantifying the size of the complex near fields induced by mask edges. Data is given for several mask blanks, along with mask behavior for off-axis illumination. The methodology is extended to the near-fields to look at field errors, as well as complicated behaviors such as cross-talk and 2-D mask features such as line ends in Chapter 5. A MoSi attenuating phase shifting mask is examined in detail and guidelines for cross-talk behavior are given.

The second half of the thesis addresses Source-Pupil Kernel Convolution with Pattern

Matching. A novel framework for extending the generality and accuracy of pattern matching techniques is presented in Chapter 6. This new approach includes complex mask transmission and automatically generated kernels based on a specified pupil function and source distribution. A nominal field calculation removes the need for any prior information or data training, making SP-KCPM standalone. Chapter 7 carefully treats the challenge of accurately modeling the partial coherence associated with source illumination arriving simultaneously from many angles. By incorporating source splitting, SP-KCPM is shown to be accurate with correlation above 0.99 for a complex mask, a general pupil function, and arbitrary source distribution. The impressive accuracy and speed of SP-KCPM is clearly demonstrated using advanced mask and sources in Chapter 8. This involves accurately modeling pixelated optimized sources, decisions between source configurations and mask blanks, along with tracking a changing mask as in a mask optimization environment.

Chapter 2

Background

Lithography has advanced by achieving balances between many factors and this thesis focus on a growing problem of mask edge effects. Simulation has played a very important role and to meet today's challenges entirely different capabilities are needed. This chapter provides background on the many factors that affect lithography, the tools developed to characterize them and the emergence of needs for fast-CAD techniques capable of quickly examining a full chip layout.

This chapter begins with a brief description of the status of today's projection printing. It then gives background on modeling tools and those used in this thesis for aerial image simulation and rigorous electromagnetic analysis of masks. The nature of mask edge effects is then explored followed by methods for incorporating them in aerial image simulation. Finally pattern matching as a first-cut accurate fast-CAD method is described.

2.1 Evolution of Lithography and its Challenges

Optical lithography with wavelength of 193nm is currently being used to image features as small as 32nm, with the 22nm node readying for production in 2011. Imaging sub-wavelength features leads to a complicated system, which given current technology must be accurate to the nanometer. Because $\lambda = 13.5$nm extreme ultraviolet (EUV) lithography has been delayed by cost and technology issues, 193nm illumination remains the workhorse for high volume lithography.

To print such small features and maintain high yield many factors from tools to design to modeling all must be pushed to squeeze out every bit of resolution. By submerging a wafer in water (immersion lithography), an effective wavelength reduction can be used to increase resolution. Combined with high-off axis illumination effective NA or 1.35 can be achieved.

As Moore's law moves forward additional gain can be achieved from using optimized designs to improve image quality. This has led to a growing need for computational lithography techniques such as optical proximity correction (OPC) and more recently source-mask-optimization (SMO). With SMO, a source and mask are iteratively co-optimized to produce an optimal, and often non-intuitive source mask configuration to produce a given

design.

Currently industry SMO software runs in about an hour for the area of a few transistors or several square microns. There is still a large gap between these advanced computational lithography techniques and bringing it to full-chip scaling. Additionally, to improve runtime, process parameters are often excluded and potential sources of variation, such as mask topography are over-simplified or even left out. The goal of this thesis is to address the issue of modeling scattering from photomask edges by leveraging existing simulation tools, filling in the gaps between them and improved modeling and insight. The result is faster calculation and compensation for full-chip and optimization applications.

2.2 Lithography Simulation Overview

2.2.1 Rigorous Numerical Solution for Maxwell's Equations

There are several common methods used for numerical solution of Maxwell's equations for arbitrary geometries. Finite Elements Methods (FEM), Finite-Difference-Time-Domain (FDTD), and Waveguide Method (WGM). FDTD in particular is commonly used for lithography applications because it is simple, flexible, and easy parallelize. FDTD simulation using a staggered grid was initially proposed by Yee [76, 63]. FDTD operates by defining electric and magnetic field nodes that are spatially and temporally staggered over a three-dimensional topography. An initial stimulus, such as a incident plane wave, can be input into the system and iteratively solved for the full rigorous field solution of Maxwell's equations.

The UC Berkeley FDTD software is called TEMPEST, which stands for Time-domain Electromagnetic Massively Parallel Evaluation of Scattering from Topography. TEMPEST was initially formulated by Guerrieri et. al. [31, 24], and extended by Wong [69, 70]. Pistor extended and optimized the code in version 5.0, adding features to better handle parallelization and including perfectly matching layers [52]. TEMPEST 5.0 was also used in the development of commercial FDTD and imaging software made by Panoramic Technologies [64]. Ceperley made the most recent modifications to include pulsed sources, surface plasmon sources, improved PML, and Floquet boundary conditions in version 7 [14].

TEMPEST version 5 and Panoramic were used extensively for near field calculations in Chapters 3 to 5

2.2.2 Aerial Imaging

Standard aerial image formation is often split into two formulations: Integration over the source (Abbe's method) and integration over pairs of diffracted orders weighted by a mutual intensity function (Hopkins' method).

One implementation of Hopkins' method was done by O'Toole et al. at UC Berkeley [48, 47]. SPLAT was later developed at UC Berkeley by Toh from SAMPLE, and uses transmission cross coefficients to implement Hopkins' method [67]. Sum of coherent systems (SOCS) model for imaging uses singular value decomposition as a method for reducing

imaging kernels [17, 18]. There are many commercial software tools available for image calculation. For example, Panoramic Technologies software connects FDTD with Abbe illumination [64]. Calibre [30] developed by Mentor Graphics is a commercial optical proximity correction (OPC) tool based on SOCS. Kenji Yamazoe and implemented Abbe's method imaging in Matlab was extensively used for algorithm The accuracy of his code has been confirmed by two other algorithms: one is an eigenfunction decomposition method [73] and the other is a matrix calculation method [74].

Aerial images in this dissertation were calculated depending on the concept to be illustrated with SPLAT, Panoramic, Calibre, or Yamazoe's Abbe implementation in Matlab.

2.3 Electromagnetic Effects in Photomask Transmission

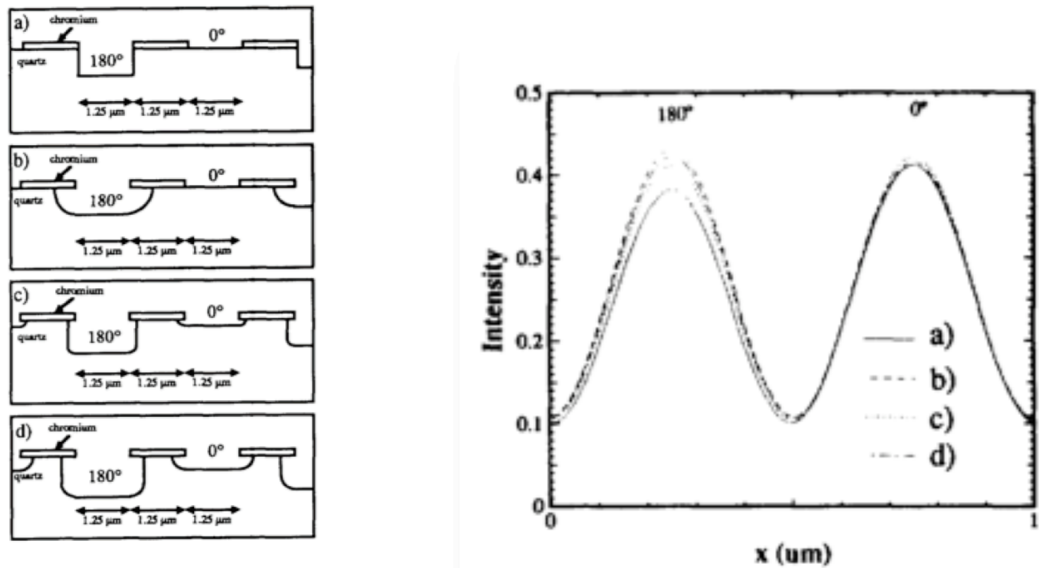

(a) Four geometries for an alternating phase shift mask.

(b) Intensity for 0° and 180° mask openings.

Figure 2.1: Intensity imbalance for alternating phase shifting mask observed by Wong. [72]

2.3.1 Intensity Imbalance

Simulation showed for an alternating phase shifting mask (Figure 2.1(a)) that despite mask openings of equal size, an intensity imbalance was observed such that the 180° etched region had a lower intensity than the un-etched 0° counterpart as shown in Figure 2.1(b) [72, 71]. This behavior, initially thought to be simulator error, was later confirmed by

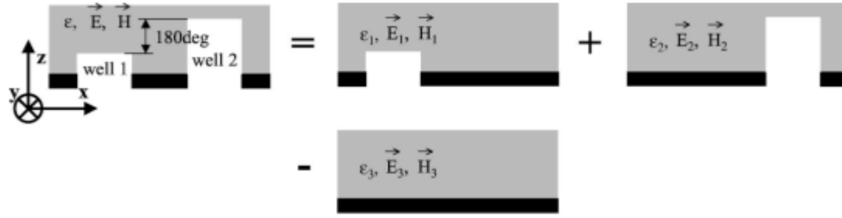

Figure 2.2: Sample breakdown of mask openings into simpler geometries using Domain Decomposition Method (DDM). [1]

experiment [49, 69]. Yuan explored the differences between scalar and vector diffraction theory [77]. These observations led to a large group of authors who began exploring mask topography behaviors.

For two-beam imaging with $\pm 1^{st}$ diffraction orders, a symmetric pattern is created. It has been shown that once 0th order transmission is introduced by an imbalance in the grating pattern due to edges, etch depth, or absorber thickness an intensity imbalance results [35]. Erdmann observed through focus asymmetry [22, 21] in phase shifting masks, and described the mask scattering behavior as a spherical aberration [20]. The edge transmission errors were described as a polarization induced astigmatism by Ruoff et al. [60]. Yan addressed Bossung curve asymmetry for EUV lithography [75].

Friedrich et al. used simulation to optimize trench design of alternating phase shifting masks [23]. Hibbs and Brunner reported that phase shifting masks can be experimentally calibrated by studying this asymmetry induced by 0th order transmission in 3-beam imaging [32]. It was shown by Gleason that the extinction condition for the 0th order transmission can be found by adjusting the etch depth, and therefore resultant phase, of phase shifting masks [29]. This correction was shown to be pitch dependent, and this observation sparked work in this thesis on general pitch dependent characterization schemes.

2.3.2 Modeling

Domain Decomposition Method

Domain Decomposition Method, proposed by Adam and Neureuther [5, 6, 1, 38] is one way to model electromagnetic edge behavior. DDM leverages superposition to break a complicated geometry into simpler pieces as in Figure 2.2. An arbitrary 2-D layout can be broken down into single openings, which can be rigorously simulated offline. This can also be applied to individual edges (edge-DDM), as long as edges are sufficiently far apart that the do not interact [7, 1]. Combined with a lookup table based approach, rigorous transmission can be calculated from the pre-computed values for mask openings and edges. This technique is implemented in Calibre software from Mentor Graphics [2].

With DDM, no mask representation is produced, as the diffraction orders are corrected without an intermediate mask step. Though this works well for imaging, in can be difficult to

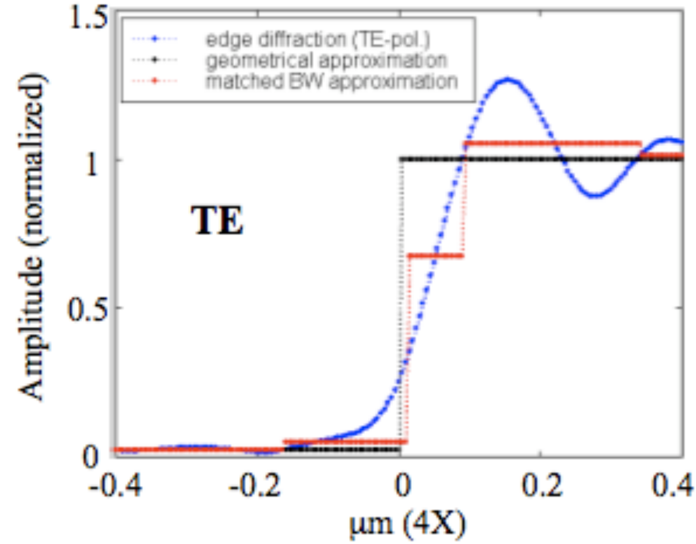

Figure 2.3: Piecewise model proposed to model photomask edge transition. [7]

pass the information from DDM to fast-CAD tools without a new corrected mask geometry.

Boundary Layer Modeling

Adam and Neureuther looked at modeling the edge transition (Figure 2.3) [7]. A piecewise constant model was used to match the scattered field behavior. This was a step toward an on mask representation of the scattered fields.

Tirapu-Azpiroz and Yablonovitch proposed boundary layer (BL) modeling as a way to model and compensate for EMF behavior [66, 65]. By calculating the amplitude transmission error, a real bias was calculated for a square opening. The error in the imaginary field transmission was used to calculate an additional out of phase transmission boundary layer

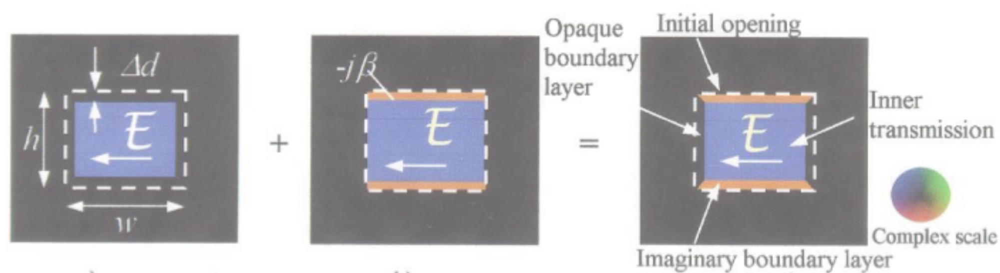

Figure 2.4: Real bias Δd, and imaginary transmission $(-j\beta)$, used to model scattering behavior in an alternating phase shift mask. [65]

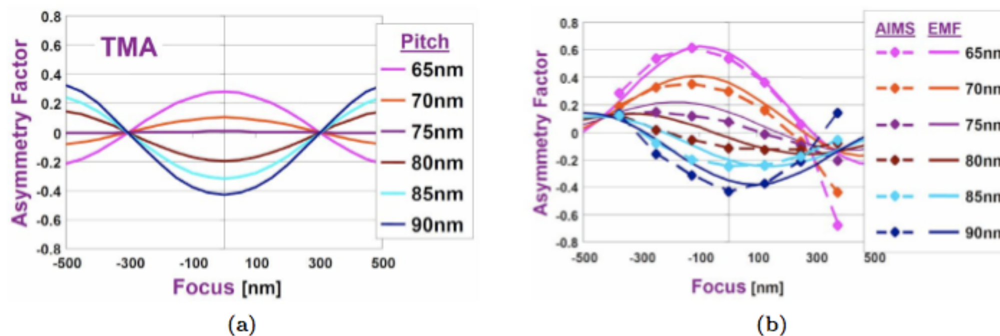

Figure 2.5: Asymmetry through focus used to calibrate boundary layer models to match rigorous simulation and experiment. [8]

as shown in Figure 2.4. This was calibrated for an alternating phase shift mask. BL modeling was continued by several authors [12, 36, 37, 45, 44]. Tirapu-Azpiroz at IBM used the asymmetry factor to calibrate BL models (Figure 2.5) [10, 8]. An isotropic BL solution was also proposed [9]. Boundary layer style models were even used for calculating performance limits for a Terrestrial Planet Finder Coronagraph [14].

Boundary layers operate similarly to DDM, but in the spatial domain rather than modifying diffraction orders. The mask representation fits more naturally with a pattern matching scheme, which relies on comparing layout snipets. For this reason, BL modeling is used rather than DDM throughout this dissertation.

Despite work by many authors, BL modeling needed additional characterization, some of which is undertaken in this thesis. These include modeling crosstalk behavior, calibration for off-axis illumination, and simple characterization schemes for new mask blanks.

2.4 Kernel Convolution with Pattern Matching

2.4.1 Pattern Matching

Pattern matching refers to the technique of assessing the degree of similarity for a layout to a specified pattern. In lithography, this can be used to measure the similarity of layout patterns across a wafer. A pattern matching was engine developed by Frank Gennari at UC Berkeley [26, 25]. The advantage of pattern matching is speed. Since it requires only a simple pixel based multiplication at the target location, and even this can be accelerated by precomputation and look-up of corner quadrant layouts at various shifts from the observation point, it can be used for hotspot detection for specific aberration sensitivities. A full chip aerial image can take days or even weeks to calculate with modern computing tools. Pattern matching can scan a layout and detect hotspots in hours instead of days [26].

Along with Gennari, Robins and Neureuther developed a methodology for assessing sensitivity to specific aberrations using Maximum Lateral Test Patterns (MLTPs) [55]. The

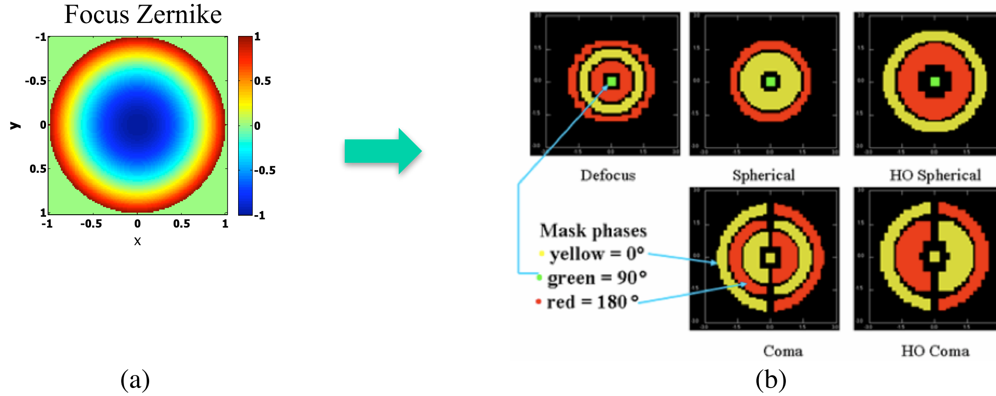

(a) (b)

Figure 2.6: a) Z_3 Zernike polynomial. b) Spillover functions calculated from Zernike polynomials shown for focus, spherical, and coma aberrations. [53]

inverse Fourier transform of the Zernike polynomials [61] is the point response, under coherent illumination, for the specified aberration. By defining a on mask pattern similar to this distribution, these MLTPs are formed to describe the layout that would have maximum sensitivity to the aberration in question. Example patterns are shown for defocus, coma, and spherical in Figure 2.6. These patterns can be used in real masks to monitor aberration behavior [56, 34].

In addition to experimentally monitoring aberrations, these MLTPs can be used as a reference for layout regions highly sensitive to aberrations.Using the pattern matcher the MLTPs can be scanned across a layout in order to find similar, and therefore sensitive areas of the chip. McIntyre added the ability to monitor polarization using similar influence patterns with phase shifting masks [43]. Initially hotspot detection was performed to calculate sensitivity to coma aberrations [33]. Rubinstein [58] expanded pattern matching to be used for detecting sensitivity to defocus aberrations to high accuracy using this method by using both a second order as well as first order terms in the expansion of e^{jOPD}, where ODP is the optical path difference. Further the line edge placement error can be estimated from the change in intensity. Pattern matching can also be used to assist with double patterning split assessment [57]. It has also been shown by Wang that incoherent source effects can be folded in using the mutual coherence (FT[Source]) multiplied by the coherent spillover function [68]. In these schemes, pattern matching in essence gives a measure of how close the layout in question is to the worst-case (maximum spillover) pattern.

One of the challenges undertaken in this thesis is how to extend kernel convolution with pattern matching to complex boundary layers to assess the impact of mask edge effects. Fortunately, the integer implemented complex algebra by Frank Gennari help facilitate this by including complex operations. His pattern matching engine was used to facilitate the methodologies and examples presented in Chapters 6 to 8.

2.4.2 Conclusions

This chapter presented an overview of the current state of lithography and modeling, along with descriptions of the existing tools for simulation and modeling. With the increased importance on previously small physical phenomena, such as electromagnetic mask edge effects, it is necessary to develop capabilities to take information from slow accurate methods like FDTD upstream to fast tools like pattern matching. The opportunity lies in the connections between the well established hierarchy of rigorous simulation, aerial image calculation, and pattern matching.

This thesis initially treats the problem of taking near field information from FDTD simulation to boundary layer modeling and then addresses taking that intermediate result to fast full chip calculation with a new formulation built to leverage the speed of pattern matching. This was to address the specific problem of mask edge effects, and resulted in a novel method for pattern matching, offering additional flexibility and application for modeling aberrations and other behaviors not specific to mask topography effects.

Chapter 3

Image Tilt Through Focus

This chapter illustrates the non-ideal behaviors of 3-D mask geometries, along with the resulting consequences on through focus imaging. In particular, to study near field and image effects, lines of finite length and jogs, as typically found in SRAM, are tested. Through rigorous simulation, a clear asymmetry through focus is observed, and if not properly accounted for leads to a loss in process latitude. The physical nature of the change in the through-focus imaging of these features due to their near-field effects is then explained using general thin mask descriptions. This preliminary study of edges, ends, and jogs then helps determine the characterization strategy for subsequent chapters.

This chapter begins with near fields, followed by imaging to demonstrate the impact of edge transmission errors on through focus imaging. In Section 3.2, a look at intensity calculation is used to demonstrate why imaginary mask transmission leads to asymmetric behavior through focus. Lastly, the consequences of this asymmetry is examined in a thin mask framework. This phenomenon lays the groundwork for further discussion of modeling edge effects throughout the dissertation.

3.1 Rigorous Simulations Demonstrate Through-Focus Asymmetry

FDTD simulation offers a convenient tool for calculating thick mask behavior. By solving Maxwell's equations on a grid, it is possible to calculate the rigorous field transmission, taking into account the true mask geometry. These near-fields are then utilized to determine the far-field diffraction pattern from which the nominal and through-focus image are calculated Rigorous simulation is computationally intensive, and therefore is only practical for small layouts. Here two examples are shown of aerial image simulation with full thick mask simulation for a MoSi Attenuating-Phase Shift Mask (Att-PSM) with a 72nm absorber.

3.1.1 CD Change for Line Ends and Edges

A MoSi line 200nm x 1200nm on mask was simulated with on-axis illumination using TEMPEST [52, 14]. A cut plane of the near fields was then loaded into Panoramic [64] to

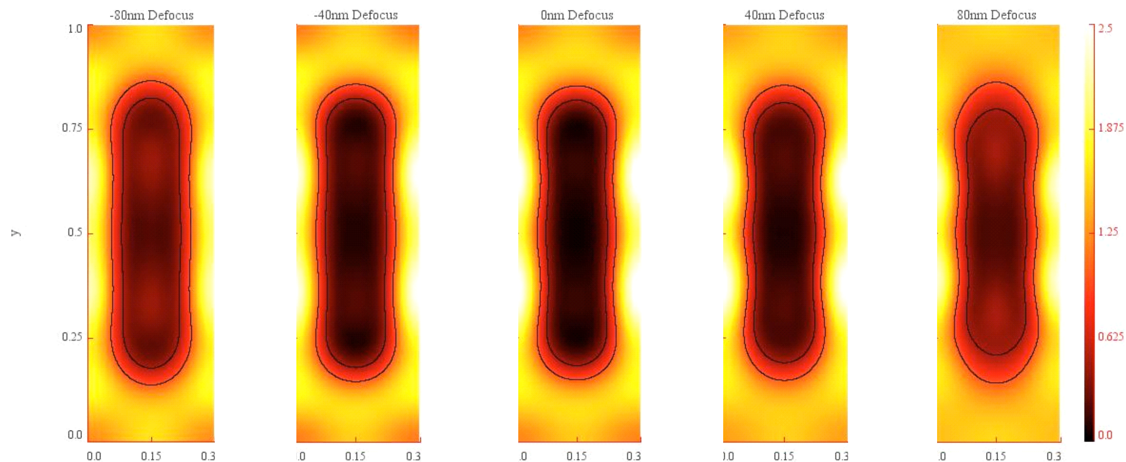

Figure 3.1: Aerial images of a 200nm x 1200nm MoSi line simulated in TEMPEST, with aerial image calculated at 2x reduction and NA = 1.2 in Panoramic [64].

compute the aerial image and observe the on wafer effects through focus. For the aerial image calculation, $\sigma = 0$ was used to emulate coherent illumination with NA = 1.0 and 2x reduction. Figure 3.1 shows the aerial image produced through varying levels of defocus (-80nm, -40nm, 0nm, 40nm, 80nm). The line end regions of the images at -80 nm and +80 nm defocus clearly show asymmetry through focus. Comparing +80 to -80nm defocus, the +80nm image appears more faded at the line ends and wavy on the sides.

Figure 3.2 shows the resulting CD measurements in both the x and y directions taken at the middle of the feature. For the in focus case, the feature was 705nm by 188nm for a threshold of 1.0, and 636nm by 145nm for threshold of 0.5. The threshold values are in arbitrary units of intensity. The data in Fig 3.2 shows the deviation from the in focus values. As expected, the effect is more severe for the line ends (y cuts) compared to the sides (x cuts). All four curves exhibit asymmetry of varying degrees. Comparing the red and blue curves for different contour levels, it is apparent that the nature of the through focus behavior depends on image slope. For the two threshold values, the contours move in the opposite direction, larger for a threshold of 1, and smaller for a threshold of 0.5. This implies more severe degradation in the image contrast for +80nm of defocus compared to -80nm.

3.1.2 CD Change for Features with a Jog

Now we look at a finite feature with a jog, similar to what is often seen in a SRAM layout. An example image is shown in Figure 3.3, with CD data and layout schematic in Figure 3.4. The example pattern is a 1200nm MoSi line with a 100nm jog in the center. The thin end is 200nm, and the wide end is 300nm on mask. The simulation used unpolarized

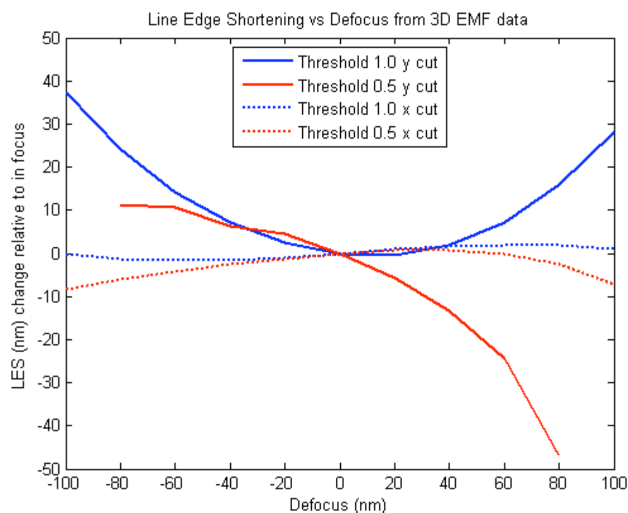

Figure 3.2: CD data for the images in Figure 3.1 in the x and y direction for two threshold levels.

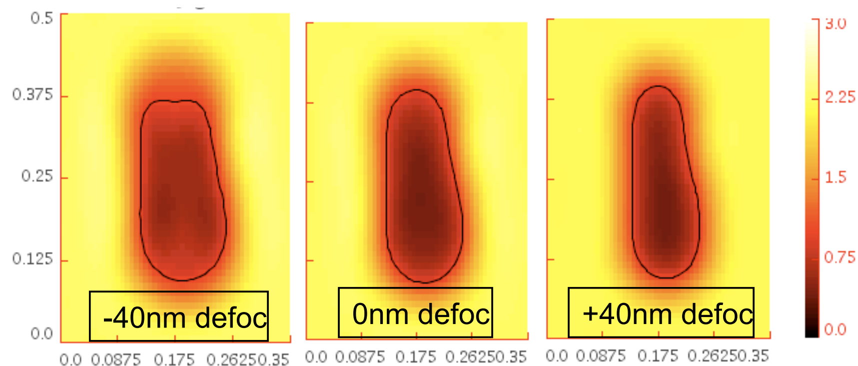

Figure 3.3: Aerial image for 3 focus values from rigorous simulation of 1200nm line with width of 200nm on thin end and 300nm on wide end, and a 100nm jog in center. $NA = 1.35$, $\sigma = .7$, 4x reduction factor. Geometry shown in Figure 3.4

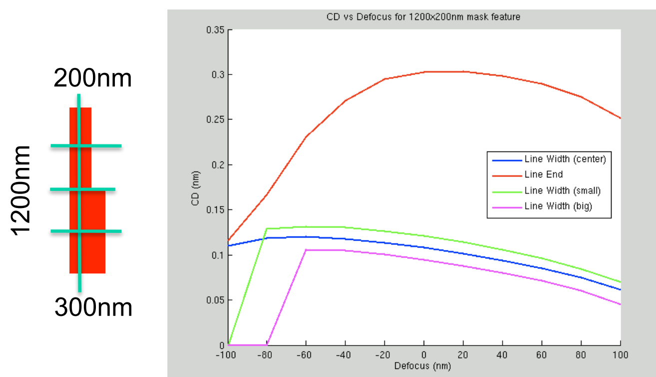

Figure 3.4: CD data for several cross-sections across the jog feature.

illumination with $NA = 1.35$, $\sigma = .7$, and 4x reduction. The asymmetry is clearly apparent in the aerial images at $\pm$40nm defocus. This pattern was chosen because jog patterns are typical in SRAM layouts and extended gradients can amplify alignment errors and alter transistor strengths.

By comparing the aerial image at -40, 0, and 40nm of defocus in Figure 3.3, through focus asymmetry is again apparent. -40nm defocus causes the feature to stretch to become long and skinny. +40nm defocus results in a shorter fatter feature. Looking at the CD data from cutlines in several locations (Figure 3.4) verifies this behavior. One additional complicating factor for non-rectangular features is the alignment. The jog introduces a CD gradient which leads to a change in device size if layers are misaligned. Accurate EMF modeling of the tilt in the process window, and resulting shift in best focus becomes even more important to build into the design flow to avoid magnifying other sources of error like alignment.

3.2 Impact on Imaging Through Focus with Thin Mask Model

One way to model the errors introduced by mask edges are by using boundary layers [65, 9, 44, 45]. The presence of these additional edge sources will affect the imaging and printing of features. The real edge source component will act similar to a bias and still result in symmetric behavior through focus. However, the imaginary edge source component will directly interact with the spillover of the electric field from the surrounding that also has an imaginary phase. In the case of defocus, this will introduce an odd component to the change in either edge placement or line end shortening (LES) through focus.

To test the impact on imaging, SPLAT was used to simulate the aerial images from a thin mask model with and without an imaginary boundary component to examine through focus behavior. For this analysis, both isolated and surrounded line patterns were simulated with boundary layers similar to those observed through FDTD simulation in the previous

section.

3.2.1 Low Numerical Aperture Normalized Isolated and Dense Lines

To simplify the estimate and illustrate the edge effect without contamination by resist and high-NA effects, simulation at a low NA was used. For convenience a NA of 0.5 and a wavelength of 0.5um were used. This makes a $k_1 = 0.5$ feature 0.5 microns in size and the Rayleigh defocus distance 1.0um. An estimate for the 45nm technology was made by noting that a 0.1λ edge source is approximately 10% of the feature size. For a k1 factor of 0.5, the feature size becomes 500nm with a 50nm trim. This mimics the desired 10% edge effect. The simulation was then carried out with an on-axis source with sigma = 0.3. The measure of the focus effect is LES for which the lateral spillover comes from many directions and results in strong focus dependence. A positive LES corresponds to the line end shortening, where negative LES is the expansion of the line end.

Figure 3.5(a) shows the simulated geometry for the isolated line. The line is 500nm wide and the green region is 6.25% transmitting, 180° out of phase with respect to the fully transmitting black background. In Figure 3.5(c), the plot of LES versus defocus is shown. The trim, shown as a thin red layer around the feature, is 50 nm wide with 90° phase and 100% transmission. It should be noted that the trim cuts into and sets to zero the background transmission under this trim.

For the layout without the boundary layer, the LES curve is a symmetric parabola. The out of phase boundary layer for this equivalent source caused the focus curves to rotate, clockwise. Fitting the data in these figures to a polynomial reveals a linear slope of -0.055 (λ/NA per RU defocus). The consequence of this is a shift in the center of the acceptable focal range by about 0.5 RU.

Figure 3.5(b) shows a dense line surround pattern around the isolated line from the previous example. In the layout, the feature widths are 0.5 um and the spacing between them is also 0.5 um. Figure 3.5(d) shows the effect of the imaginary contribution on LES for this pattern. Again, the curve is symmetric with no boundary layer, but with the 90° trim, there is a similar rotation and a linear contribution with slope of -0.54. The magnitude of the square term indicates an increase in sensitivity through focus of about 15% for the dense pattern compared to the isolated line. The overall behavior is still similar for both cases.

3.2.2 193nm Wavelength Isolated and Dense Lines

To follow up on the effect of phase on through focus behavior, a similar study was performed for a binary mask illuminated at $\lambda = 193$nm, with 45nm features, NA = 0.5, and BL = 10nm. In addition to the magnitude of the BL transmissions, the sign is also critical. Figure 3.6 shows CD data for real features with and without bias, as well as BL values of 90° and 270° transmission for the dense layout shown in Figure 3.5(b). Due to calibration of the image plan in the Calibre [30] software, there is a small offset for nominal defocus. For the cases with only real transmission, the bossung curves are symmetric through focus, just

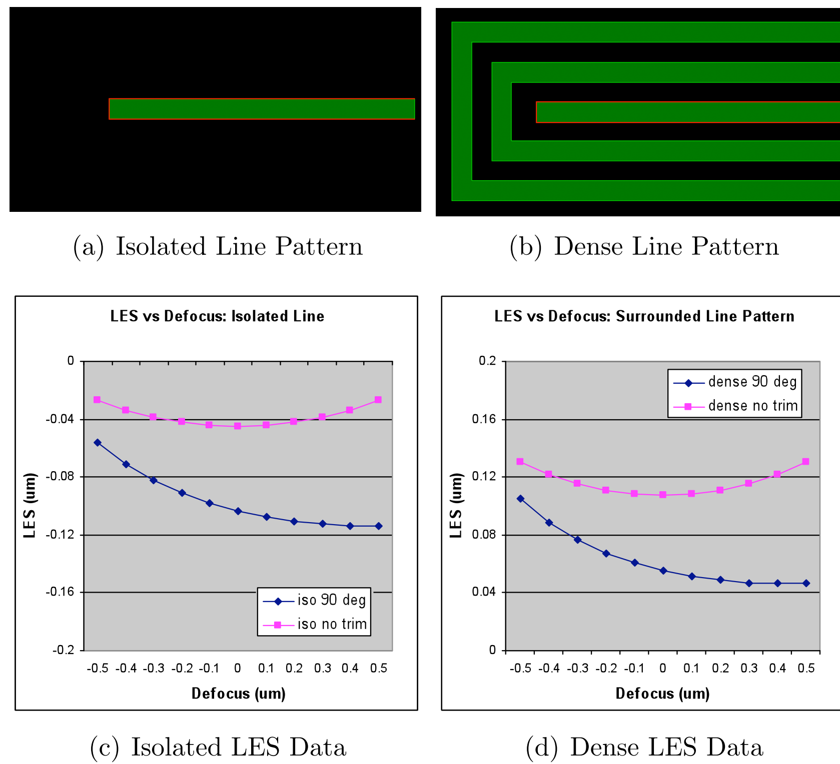

(a) Isolated Line Pattern

(b) Dense Line Pattern

(c) Isolated LES Data

(d) Dense LES Data

Figure 3.5: SPLAT used to calculate image of isolated and dense geometries with and without BLs for an Att-PSM, with transmission of 6.25% intensity at 180°. NA = 0.5, $\lambda = 0.5\mu m$, 50nm trim (10% of feature) and $\sigma = 0.3$ was used. Line End Shortening (LES) data plotted vs. defocus.

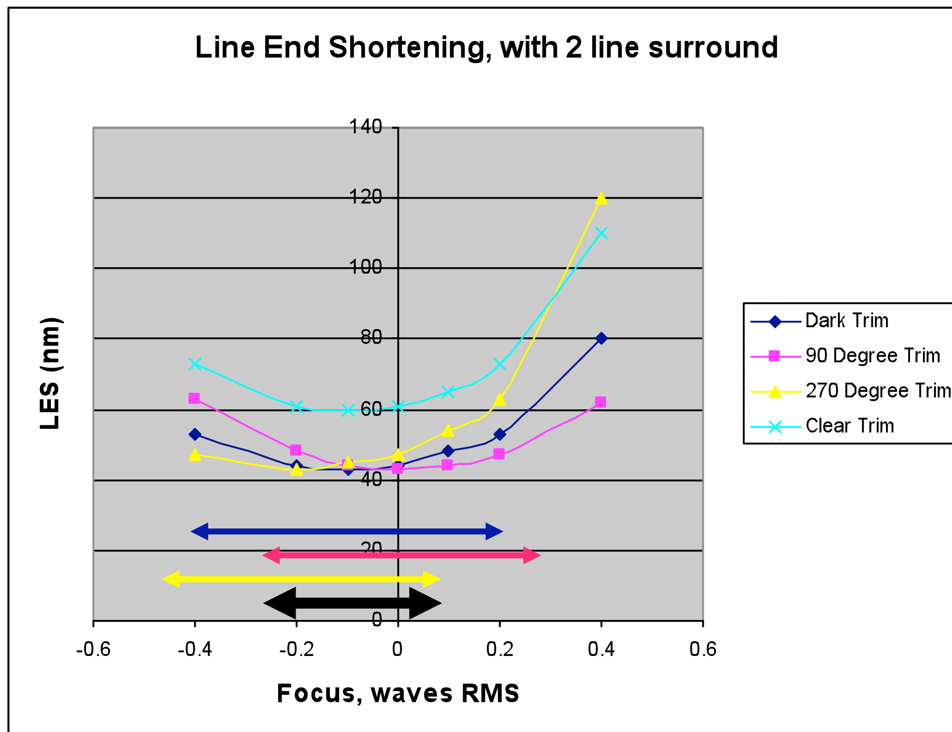

Figure 3.6: For the dense pattern such as in Figure 3.5(b) with a dark field binary mask and 45nm features, LES is plotted vs. defocus for the cases with no BL, 0°, 90°, and 270° trim. $\lambda = 193$, NA = 0.5, and BL = 10nm were used.

shifted vertically because the bias makes the absorber larger. The pink and yellow curves show the tilt induced by the odd component of defocus interaction when imaginary trim is added to the features. What is important to notice is that the curves tilt in opposite directions for 90° compared to 270°.

For a given threshold and CD tolerance, the process window now becomes the overlap of these two curves, which can shrink the process window significantly. Looking at Figure 3.6, the initial acceptable defocus range for a specific CD is represented by the blue arrow. With BLs added, the acceptable CD shifts to the pink and yellow arrows for 90° and 270° respectively. The resulting acceptable focus window is the overlapping area, shown by the black arrow. For a LES level of 50nm, the focus tolerance is reduced from $\pm 0.3\ \lambda$ RMS to about $\pm 0.18\ \lambda$ RMS, for about a 40% reduction in focus latitude. This case is meant to be illustrative, and the true consequence is dependent on several factors such as mask blank, CD tolerance, and feature size.

3.3 Conclusions

Rigorous simulation was used to demonstrate the nature of 3-D mask topography on through focus imaging. One of the most important qualities is the asymmetric behavior which causes a feature dependent shift in best focus, resulting in a loss of focus latitude. This is apparent for line ends, and is enhanced by additional factors such as alignment for more complicated features like jogs. Because of the varying nature of the effect on imaging, proper modeling is especially useful.

The resulting asymmetric through focus behavior was explained by 90° or 270° phase transmission errors interacting with the imaginary component of defocus spillover which is odd. Assuming the edge impact is independent of opening size, as immersion lithography pushes the limits of imaging with 193nm the edge contribution will have a larger overall effect on the image. A 10% wavelength effect on each of the two edges is on the order of 1/10 of the mask opening size for 90 nm technology but becomes 1/5 of the mask opening for 45 nm technology and even larger at 22nm.

By examining typical examples of this behavior in aerial image simulation, the focus latitude of the process window is reduced by 40% for even conservative error estimates. As mask dimensions shrink, these electromagnetic effects, which were previously small contributions, play a more significant role in on wafer imaging. The addition of complex mask materials for various phase shift masks (PSMs) combined with larger angles of incidence further complicates the modeling of photomask field transmission. Complicated layouts with jogs and other features only complicate and magnify the consequences of inaccuracies in image calculation.

Chapter 4

Method for Experimental Characterization of EMF Effects

This chapter introduces a novel experimental, grating based method for quantifying the transmission errors caused by 3-D mask features by observing the diffraction order intensities from the mask. For even well-behaving masks, errors can be as high as 20% of the expected transmission. A study through off-axis illumination demonstrates the potential for maintaining accuracy for general illumination conditions. Edge effects are a growing concern in optical lithography, which leads to the important questions: How big are the edge contributions for various mask blanks? And how could they be measured?

The simple experiment compatible approach described in this chapter is based on observing the transmission intensity for characterizing the effective edge contribution corrections that should appear in a thin mask model. The method and its procedures for interpreting real and imaginary components are described first. Simulation with FDTD is used in Sections 4.2 and 4.3 to show the feasibility of carrying out this experiment, and here the physical size of effects for both Att-PSM and Alt-PSM are calculated and summarized in a Table 4.1. Finally some more complicated mask stacks are analyzed in Section 4.4.

4.1 Grating Based Calibration Method

In order to satisfy boundary conditions for Maxwell's equations and maintain continuous fields, light bends at the edges of mask openings. In the case of a phase shifting mask this results in a continuous phase front across mask boundaries. For an alternating phase-shifting mask (Alt-PSM) or attenuating phase-shifting mask (Att-PSM), by design the mask transmission phases are 0° or 180°. In practice, where these regions meet, there is a mask blank dependent region between the two phase wells where the phase lies somewhere between. The designed 0° or 180° transmission can be interpreted as real transmission of $+1$ or -1. When any other phase in introduced, an imaginary transmission component is introduced. For example, transmission of 90° or 270° would correspond to $+j$ or $-j$ transmission respectively. Separating the real and imaginary transmission leads to a convenient way of analyzing these error transmissions, as well as correcting them with boundary layer

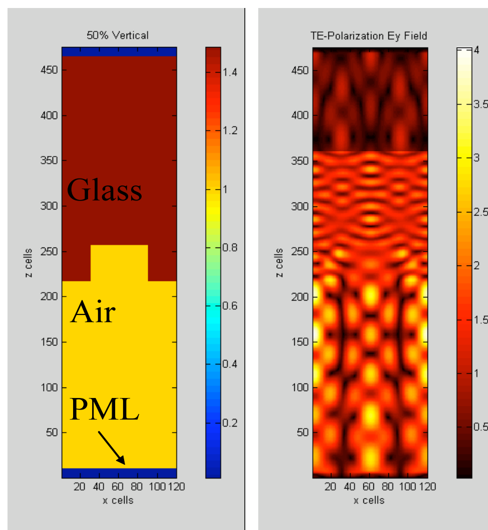

Figure 4.1: Left shows a 2-D mask opening for a Chromeless Phase Shift (CPL) mask. Right shows the field transmission for on-axis illumination with the E field going into the page. Perfectly matched layers (PML) are used at the top and bottom of the simulation domain to minimize reflections.

modeling.

When manufacturing a mask, there are two basic parameters that can be adjusted: etch depth and mask bias. Modifying etch depth provides a way to compensate for phase transmission errors, but leads to a feature dependent behavior [29]. Here, we focus on the latter, modifying mask biases, which acts as a knob to trade off the transmitted field through various phase openings. As shown in Figure 4.2, for a grating pattern the relative weight of the phase regions can be expressed as a function of duty cycle. The example shown here is for a Chromeless phase-shifting lithography mask (CPL). For this mask, the extended glass has transmission of 0°, while the etched region is made to provide 180° transmission. For the case where none of the mask is etched, the entire transmission is in phase at 0°. When a small bit of the mask is etched, some 180° transmission is introduced. When exactly half of the mask is etched, half of the field is transmitting at 0° (+1), while the other half at 180° (-1). These regions are equal and opposite, therefore the theoretical average (or 0th order) field transmission is zero.

When dealing with a Kirchoff or thin-mask approximation (TMA), the calculation of the 0th order transmission is straightforward and well behaved. For CPL, the values of the 0th order for various duty cycle values are shown in red in Figure 4.3. To calculate the transmission considering thick mask interactions, the value of the 0th order field can be calculated from FDTD simulation (Figure 4.1). From a cutline taken below the mask opening, the Fourier transform of the field reveals the diffraction order spectrum. In the same figure, the blue curve describes the 0th order field transmission from FDTD simulation for various opening sizes in terms of duty cycle. The important features to notice are the the

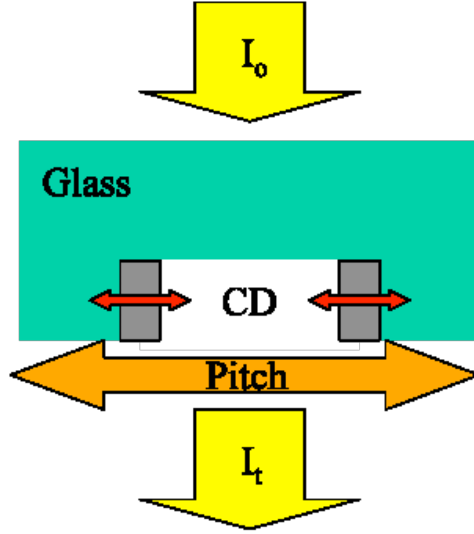

Figure 4.2: Schematic of the edge calibration experiment. Pitch and CD are varied to cancel 0° and 180° regions.

shift in minimum location as well as the non-zero minimum of the rigorous data. The shift indicates a bias in the true size or electromagnetic size of an opening. What happens for CPL is that field is pulled from the etched opening into the higher index extended region. This causes openings to appear electromagnetically smaller, while extensions appear larger. By changing the duty cycle, it is possible to find the minimum 0th order transmission, which describes the point of maximum cancellation between the 0° and 180° transmitting regions. From the shift in minimum location, we can calculate the effective bias required to compensate the thick mask effect in order to match TMA. The bias required is calculated as:

$$Bias = (min_{TMA} - min_{EMF})\frac{Pitch}{2} \tag{4.1}$$

where min_{TMA} describes the minimum location of the TMA maximum cancellation and min_{EMF} the shift observed from FDTD simulation or EMF data in percent. Multiplying by pitch brings the units to nm, and the value is divided by two to take into account the effect of both edges.

In addition to the shift in minimum location, in the EMF data does not drop to zero at any point of the duty cycle sweep. When adjusting duty cycle, we are only able to control the real component of field transmission by trading off ± 1 transmission. At the minimum of the FDTD data, the point is reached where the real components have cancelled out maximally, which leaves the imaginary field component directly observable. By assuming the real component of the 0th order transmission is zero, the non-zero value of the minimum can be attributed to the imaginary transmission created by phase errors at the edges. These values can be treated in a number of ways, but the most simple way is to attribute the imaginary field errors as imaginary transmission sources located at the edges, calculated in

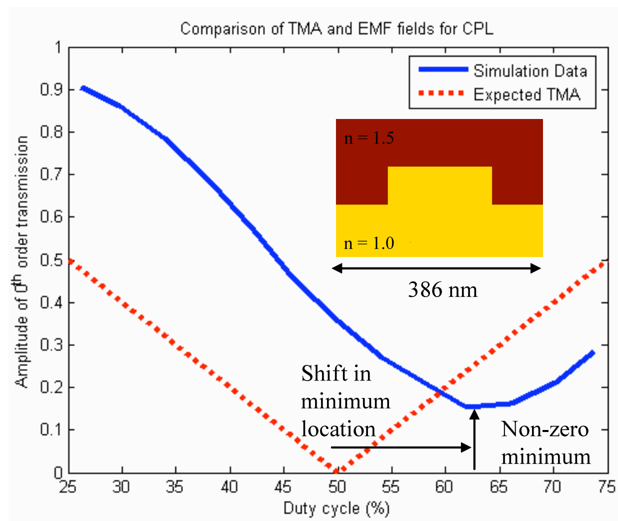

Figure 4.3: Plot of 0th order field transmission for a chromeless phase-shifting mask (CPL) for a pitch of 386 nm, for varying duty cycle. TMA and EMF fields intensities are shown in red and blue respectively.

the form of boundary layers (BLs). The values are calculated as:

$$BL = E_{min} \frac{Pitch}{2} \tag{4.2}$$

where E_{min} is the minimum field value from the duty cycle sweep, normalized by pitch and taking into account two edges. This yields an imaginary BL value normalized to transmission one with a width given in nanometers.

4.2 On-axis Simulation Data

Edge effects were analyzed for a CPL Alt-PSM and a MoSi Att-PSM. The simulations were run with periodic boundary conditions forming gratings of period 386, 579, 965, and 1930nm ($2\lambda, 3\lambda, 5\lambda, 10\lambda$) for 193nm illumination. The source was excited in the glass portion of the mask. Perfectly matched layers (PML) was used on the top and bottom boundaries to minimize reflections. Duty cycle values were simulated in 1% increments within the limitations of a 40 cell per wavelength grid in the FDTD simulations. From these simulations the real and imaginary edge contributions were extracted from the location and value of the minimum 0th order field transmission. Additionally edge contributions are calculated in mask dimensions and would be reduced accordingly for a 4x or 5x reduction projection system.

4.2.1 Chromeless Alternating Phase Shift Mask

The simplest geometry is a lossless glass CPL mask (Figure 4.4(a))with refractive index of 1.5 and a 193nm etch to produce an 180° shift. For this mask type, TMA predicts a null in the 0th order magnitude at the 50% duty cycle point. As seen in the plot, all of the minimum locations are shifted from the 50% point towards a larger opening. Also these minimum values are as high as 20% of the field transmission for the smallest period.

For the example where pitch is 2λ, we observe the minimum at roughly 62% of the mask etched. This corresponds to a 6% shift per edge, with a period of 386nm. This implies an edge contribution of about 23nm (0.1λ) per edge for the real component. At this minimum location, the field amplitude is roughly 20%. Assuming all of the transmission is due the imaginary components, we have a contribution of 10% per edge or 39nm (0.2λ). This implies that in going from a TMA model to a vector, thick mask version, the difference is a 23nm shift in the edge location, as well as a 39nm edge source of 90° or 270° phase.

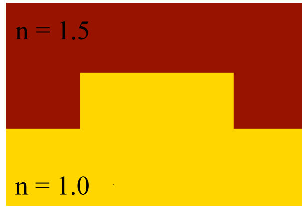

(a) CPL mask blank with refractive index 1.5 and 193nm etch for 180° transmission

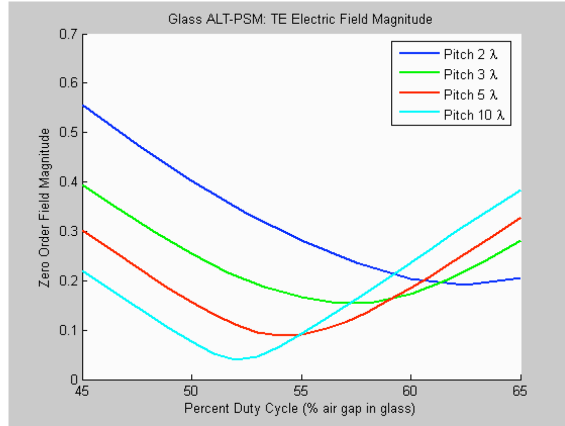

(b) Plot of 0th order field transmission for a chromeless phase-shifting mask (CPL) for a pitch of 386nm, 579nm, 965nm, and 1930nm on mask for varying duty cycle.

Figure 4.4: FDTD simulation data for 0th order transmission intensity for CPL mask at pitch of 2, 3, 5, and 10λ.

As the pitch increases, the minimum location shifts towards 50% and the field value drops closer to zero. This is the behavior we expect to see if each edge has a fixed contribution to the transmission perturbation. At a larger pitch, the same magnitude edge effect is spread over a wider region, reducing the overall effect of the edge fields. This highlights the growing importance of edge behavior as mask dimensions become smaller and smaller.

4.2.2 MoSi Attenuating Phase Shift Mask

A similar analysis of a MoSi Att-PSM is shown in Figure 4.5. For the data shown, the MoSi layer is 77.2 nm thick, which causes a phase shift of 176.8^o and transmission of 22.4%

of the electric field. By taking the ration of the intensities, we expect to see the minimum field value when 18.3% of the mask is air gap. As before, we see the minimum values shifted toward a larger air space, as well as an offset from zero. For the 2λ pitch, there is a shift of about 10% duty cycle, implying about a 20 nm real contribution. Similarly the 10% field transmission signifies a 20 nm quadrature component. As in the previous section, we observe that at wider pitches, the edge effect is less pronounced.

(a) MoSi mask blank with refractive index 2.343 + 0.586j and 77.2 nm thick

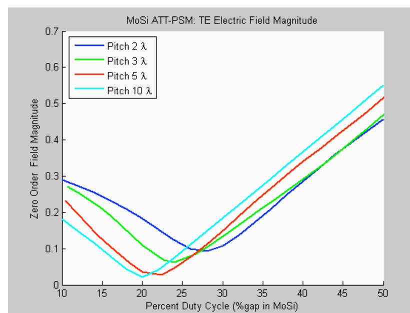

(b) Plot of 0th order field transmission for a MoSi Att-PSM for a pitch of 386nm, 579nm, 965nm, and 1930nm on mask for varying duty cycle.

Figure 4.5: FDTD simulation data for 0th order transmission intensity for MoSi mask at pitch of 2, 3, 5, and 10λ.

4.2.3 Summary of On-Axis Edge Contributions

The analysis described in the previous section was carried out for 3 periods and both polarizations. A summary of the data is shown in Table 1. There is clear polarization dependence with respect to the real correction. For both types of masks, the real shift was roughly double for TE compared to TM. This can complicate biasing in practice when using unpolarized light. As pitch is changed, the edge effects remain almost constant. This implies that the edges are acting independently. Down to pitches of about 200nm, 50nm at 4x on wafer, there is little or no edge interaction. Especially for the CPL mask, the imaginary fields produced were significant. For TM polarization, the edge contributions were as high as 44nm per edge. This is significant for smaller pitches, and can strongly influence the projected image.

4.3 Off-axis Simulation Data

The real and imaginary edge contributions were calculated for chromeless Alt-PSM and MoSi Att-PSM. Each mask was evaluated at pitch of 2, 3, and 5 wavelengths through incidence angles ranging from on-axis to 20° in air, which is about the maximum angle

Table 4.1: BL values for CPL and MoSi mask blanks for pitches of 2, 3, 5, and 10λ and TE and TM polarization. Values describe a border of transmission 1 with width given in nm.

Mask Type	Pol	Re/Im	2λ	3λ	5λ
CPL	TE	Real	27.1	22.4	24.2
		Imag	33.0	39.6	42.7
	TM	Real	15.9	9.0	10.5
		Imag	37.1	42.3	43.9
MoSi	TE	Real	19.1	16.1	16.6
		Imag	8.1	6.9	6.8
	TM	Real	8.4	7.5	6.4
		Imag	14.1	15.4	18.8

incident on a mask in a 4x reduction system. All simulations used a 2nm cell grid with periodic boundary conditions on the sides and perfectly match layers (PML) on the top and bottom. As described above, for each combination of pitch and angle, the duty cycle was varied to locate the minimum E-field transmission. The incident wave source was located in the Quartz mask and normalized to amplitude of 1. The edge data calculated for each mask follows.

4.3.1 Chromeless Alternating Phase Shift Mask

An example of the 0th order field amplitude plotted through duty cycle is shown in Figure 4.6 for a pitch of 2 wavelengths at several different incident angles. The dotted grey line shows where the expected TMA minimum should be. The actual value falls roughly 7% higher in terms of duty cycle. For a pitch of 386nm (2λ), 7% corresponds to a per edge effect of 14nm (0.07λ). Additionally the observed leakage at the null actually occurs between 20% and 23%. The result is an equivalent 90° boundary per edge of 38 nm to 45nm (0.23λ). The exact biases for the chromeless mask are shown in Figure 4.7.

The real bias for CPL is not strongly dependent on angle; however, there is clear polarization dependence. TE (E-field parallel to the lines) requires about twice the real bias correction compared to TM (H-field parallel to the lines). Additionally, the pitch dependence is weak, showing only a 5 nm spread within polarization. The imaginary correction term is larger with BL values from 30 to 45nm per edge. This effect is significant, up to 0.2λ per edge, but there is less distinction between polarizations. The TE polarization shows more variability than the TM. The large imaginary contribution from edges in CPL masks makes it difficult to work with at small sizes.

4.3.2 MoSi Attenuating Phase Shift Mask

The same analysis was carried out for the MoSi Att-PSM. Here a MoSi layer of 72nm was used for the phase shifting and attenuating element. The phase shift calculated from

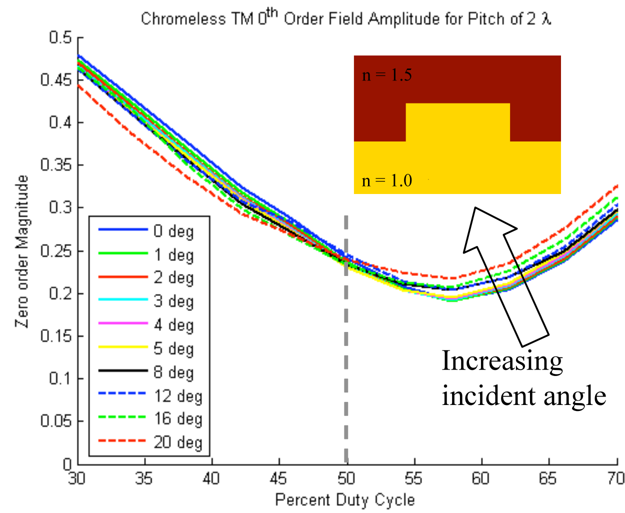

Figure 4.6: Plot of 0th order field transmission for a chromeless phase-shifting mask (CPL) for a pitch of 386 nm, for varying duty cycle and incident angle up to 20°.

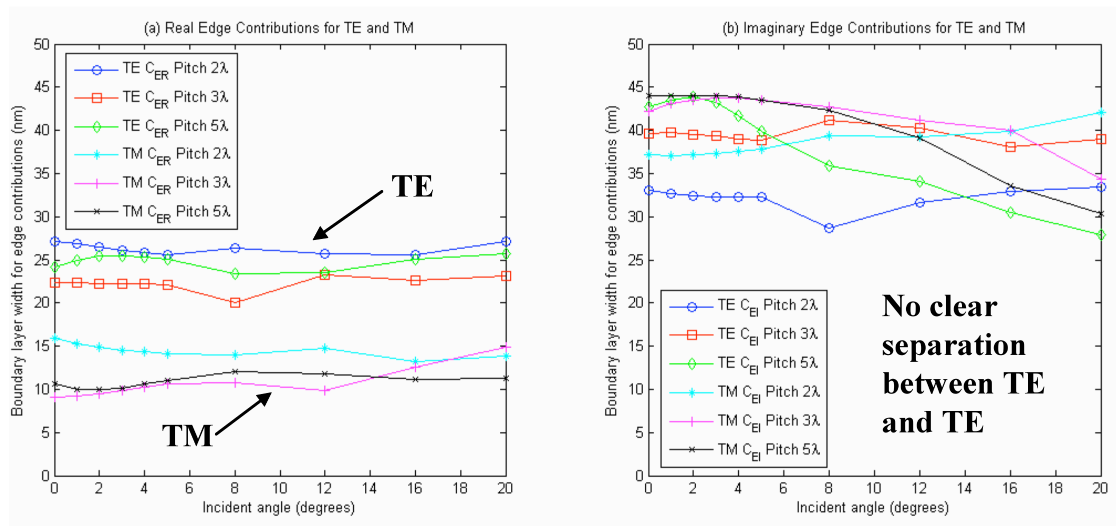

Figure 4.7: Plot of the boundary layer values for CPL up to 20° off-axis for pitches of 2, 3, and 5λ.

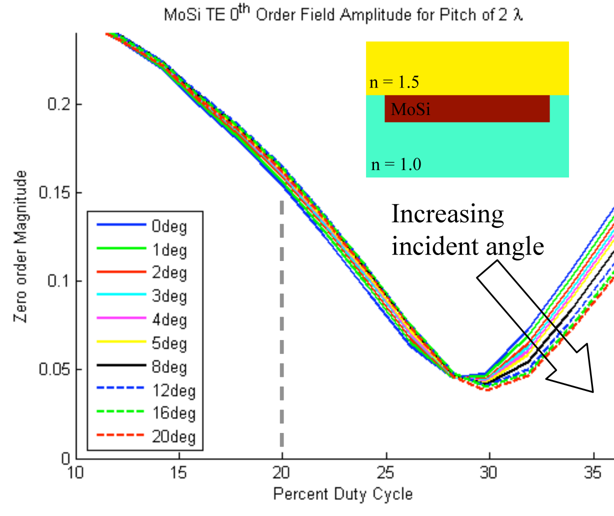

Figure 4.8: Plot of 0th order field transmission for a MoSi Att-PSM for a pitch of 386 nm, for varying duty cycle and incident angle up to 20°.

an on-axis simulation is 175.73^o, with a transmission through MoSi of 23.2% field amplitude or 5.4% intensity transmission. The phase shift was calibrated to slightly less than 180° to counteract the slightly further path difference for off-axis incidence. In practice, the phase shift can only be correct for one incident angle. By calculating the ratio of transmission between the 2 regions (100% for air, 23.2% for MoSi) the expected minimum would occur at a duty cycle where 18.9% of the pitch is air gap, with the rest covered by MoSi. Figure 4.8 shows a plot of the 0th order field amplitude for a pitch of 2λ. Here the observed 10% shift in the minimum transmission duty cycle with a 386nm pitch corresponds to a real edge bias of 19nm per edge. The 5% minimum field transmission translates to a 9nm per edge imaginary bias.

A summary of the real and imaginary biases for various incidence angles and polarization are given in Figure 4.9. The MoSi mask shows little change through angle for both polarizations. Also, the spread remains less than 5 nm through pitch. There is clear polarization dependence for both the real and imaginary bias terms. TM requires a smaller real bias, but a larger imaginary bias. Compared to chromeless, MoSi requires smaller corrections, especially for the quadrature component.

4.4 Alternate Mask Stacks

One proposed mask blank used Ta and SiO_2 to independently control attenuation and phase shift. This intensity transmission analysis was carried out for proposed Ta-SiO_2 mask stacks of 6% and 1% transmission. The 6% mask had 18nm of Ta and 144 nm of SiO_2, while the 1% had 30nm thick Ta and 138nm of SiO_2. Even for on-axis illumination, the plots for varying duty cycle, shown below in Figure 4.10, do not show the clear trends present with

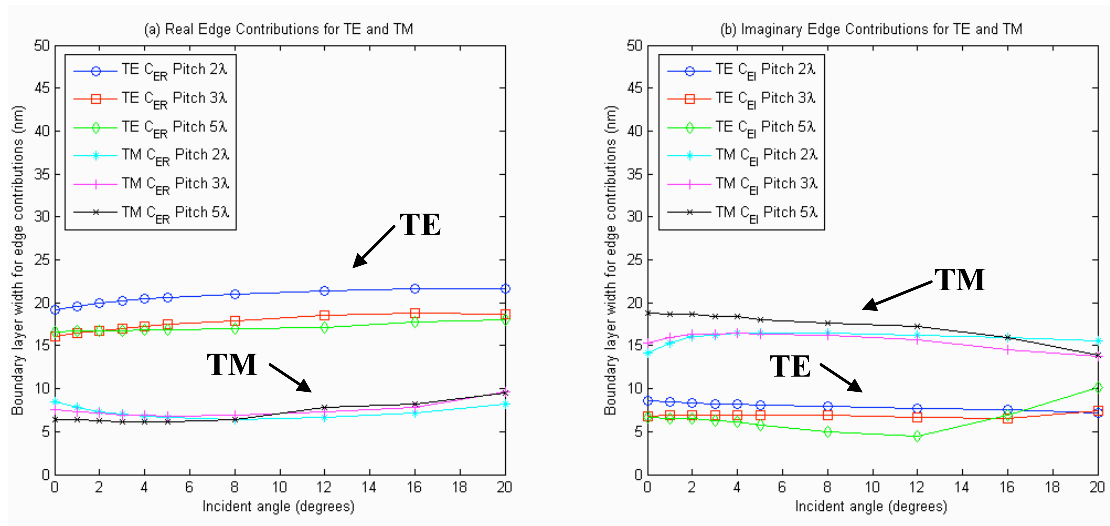

Figure 4.9: Plot of the boundary layer values for MoSi up to 20° off-axis for pitches of 2, 3, and 5λ.

the other mask geometries. This implies that there are additional effects complicating the transmission through the mask stack.

There are a couple possible explanations. Unlike the other masks, Ta-SiO_2 is made up of multiple layers which could produce wave guiding effects carrying energy laterally through the structure. Additionally, compared to MoSi, Ta is a better conductor, which attenuates the fields in a shorter distance. This could lead to large current sources appearing at the edges in the Ta layer and producing cross-talk across the gap. Figure 4.11 shows a field comparison for the Ta mask compared to MoSi for a pitch of 3λ and duty cycle of 30% air gap. A thin mask model would predict the exact same transmission for the MoSi and $TaSiO_2$ masks. In the radiation zone several wavelengths away from the mask bottom, the field structure for both types of masks appear somewhat similar; however, within the mask stack, there are far more high frequency components present in the Ta mask.

4.5 Conclusions

A proposed experiment was simulated with FDTD analysis of diffracted mask orders to quantify the values of mask edge effects for several mask blanks. By adjusting the duty cycle of grating structures, the real bias and imaginary transmission errors can be calculated by observing the 0th order field transmission. This method was tested for off-axis illumination and for relatively well behaved masks like MoSi Att-PSM. The off axis change was minimal, and could be modeled with one mask correction.

For the MoSi Att-PSM, the edge errors were under 20nm for both real and imaginary errors in mask dimensions and did not change much up to 20° off-axis incidence. The CPL mask required larger real biases, up to about 27nm and significantly larger imaginary

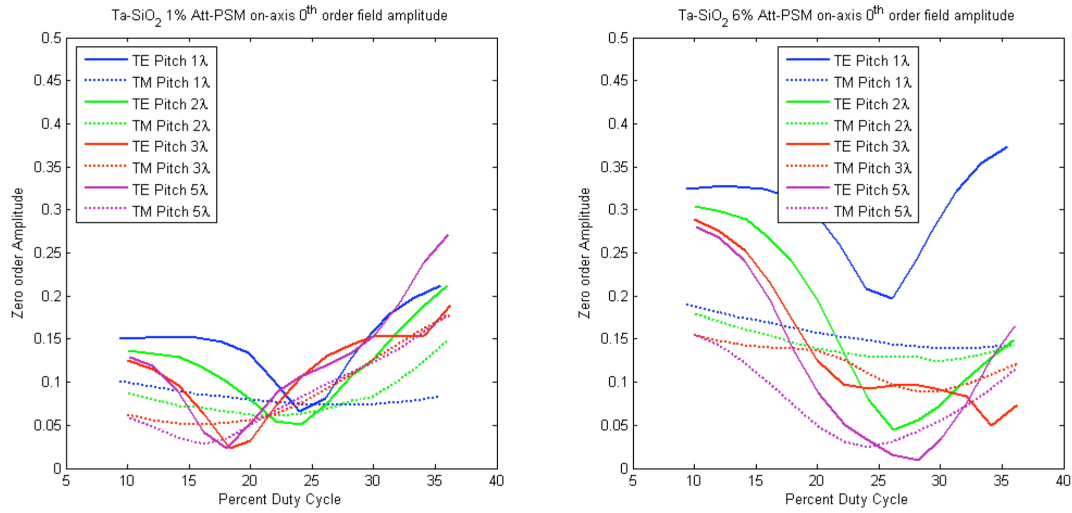

Figure 4.10: Plot of 0th order field transmission for a $TaSiO_2$ Att-PSM for a pitch of 1, 2, 3, and 5λ, for varying duty cycle and both TE and TM polatization.

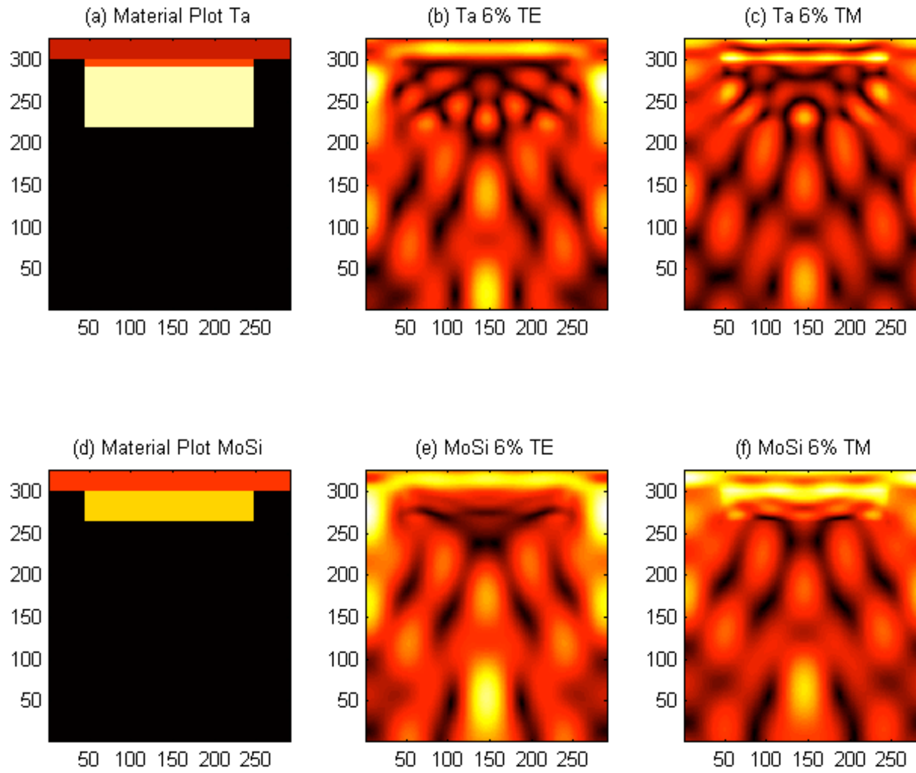

Figure 4.11: Top: $TaSiO_2$ mask blank, TE and TM near fields. Bottom: MoSi mask blank, TE and TM near fields.

transmission errors, which were as high as 44nm. The simulation data indicates that MoSi is better behaved than CPL. Conceptually this makes sense, because for CPL, no absorption takes place, which allows scattered fields to come out at full strength. With MoSi, at least some of the effects are damped by the absorbing mask material, but the transmission errors are still large enough to require proper modeling.

One observation of note is that despite the different style of masks, both $TaSiO_2$ and CPL masks performed poorly. $TaSiO_2$ offered a theoretical benefit of adjusting amplitude and phase independently, but ultimately resulted in a complicated mask stack with poor EMF quality. As a result, $TaSiO_2$ was not able to challenge MoSi as an attenuating phase shifting mask. Even though CPL offers the simplest geometry, the EMF performance is still worse than MoSi because of the full transmittance of scattered fields. At the time of this work, CPL masks were still under consideration, but has since been abandoned for better EMF performing attenuating and even binary masks. EMF effects essentially led to the discontinuation of CPL for the most aggressive patterning nodes, despite throughput and imaging benefits of a fully transmitting mask.

Chapter 5

Simulation Based Modeling of Mask EMF Effects

This chapter presents a revised method for analyzing the near fields of mask transmission, by looking directly at field amplitude instead of transmitted intensity. The near field behavior reveals more accurate phase information, eliminates the reliance on 0° and 180° transmission, and offers a more detailed picture of cross-talk across small features.

Using 0th order intensity provides a useful way of monitoring edge effects in both a simulation and experimental setting; however, this technique is limited for several reasons. The analysis relies on a trade-off between 0° and 180° transmission, which is not present in binary masks. Additionally, phase information is left out of when observing only intensity. As will be apparent, the sign of the transmission errors plays a significant role in calculating correction terms. Field analysis allows for a more detailed picture of mask edge behaviors when gaps and absorber widths become extremely small. Other authors have explored correcting edge transmission errors [6], and boundary layer models have been proposed for alternating phase shift masks [65]. Further models were later developed based on a through focus asymmetry factor [8]. Here a simple method using two-dimensional simulations of gratings help provide a clear picture of polarization dependent behavior, while clearly illustrating when varying cross-talk effects limit the applicability of boundary layers. Three-dimensional simulation of line ends reveal a method for correcting for corner transmission errors.

From the near fields, a amplitude based analysis presents a mask blank independent method for examination of field transmission errors. The revised simulation-based analysis is presented in Section 5.1, along with BL data that supports and expands upon the data from Chapter 4. Section 5.2 addresses cross-talk which occurs when thick mask effects become unpredictable due to small mask dimensions. Next, in Section 5.3 an analysis of an ultra thin mask using theoretical materials shows that the 3-D geometry effects are not the only complicating factor. Lastly, Section 5.4 looks at extending grating based analysis to general 2-D patterns.

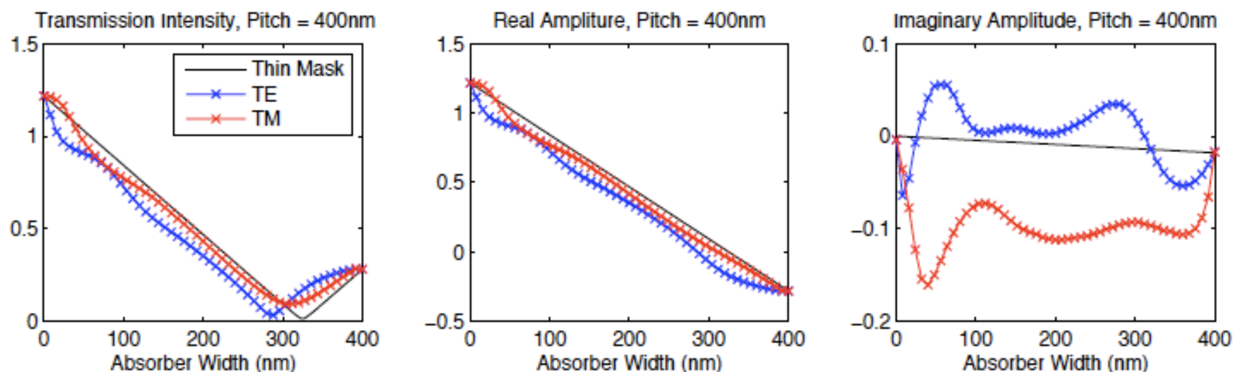

Figure 5.1: From left to right, intensity, real amplitude, and imaginary amplitude are plotted vs. absorber width for Thin Mask (TMA), TE and TM polarized illumination.

Table 5.1: Boundary Layer values for a MoSi Attenuating PSM for pitches of 400 and 1000nm for TE and TM polarization.

Mask Type	Pol	Re/Im	400nm	1000nm
MoSi	TE	Real	23.8	26.7
		Imag	4.2	4.3
	TM	Real	10.6	8.9
		Imag	-20.0	-18.0

5.1 Direct field Analysis Methodology

Using a similar methodology as presented in Section 4.1, we can gain even more insight into the field behavior by abandoning the experimental mindset. With FDTD simulation, the near fields are directly output, and give detail than cannot be gained from observing only intensity. By adjusting the duty cycle (Fig 4.2), in addition to intensity, similar plots can be created for the real and imaginary field transmission.

5.1.1 MoSi Phase Shift Mask Data

An example of this analysis for a MoSi Att-PSM with a 400nm mask pitch is shown in Figure 5.1. The plot on the left shows the intensity presented as in Chapter 4. The center shows the real field component, and imaginary is on the right. The black line shows the expected transmission for TMA, calibrated to the calculated expected transmission from a full mask blank. In this case, due to FDTD gridding, the MoSi was 72nm thick. The clear field transmission is 1.22, with dark field -0.28-0.0179j (23.1%, 176.35^o), resulting in a slight tilt in the non-zero expected imaginary transmission. Using the tools from the previous chapter, based on the minimum shift and location of the 0th order intensity transmission,

TE appears to have larger real errors, and TM has larger phase errors.

When looking at the field components directly, these intensity observations are confirmed. The boundary layer data is summarized in Table 5.1. For both polarizations, the field transmission data is shifted from the expected TMA in the same direction, indicating an effective shrinking of mask opening. The more interesting observation comes from the imaginary analysis. The magnitude of the imaginary transmission errors matches what is observed in the intensity, but now it is apparent that the errors are of opposite sign, indicated by the upward shift of TE and downward shift of TM. This behavior is confirmed by other authors [8]. The consequence of this was demonstrated in Chapter 3. There is a slight difference between the data presented here and that in Table 4.1, which can be attributed to increased accuracy by separating field components as well as subtracting out the imperfect 176° transmission (as opposed to 180°). Calculating and correcting for the correct direction of the phase error is necessary. In addition to the opposite sign for each polarization, the other important observations are that the oscillations in the tails of the plots where absorbers are either very small or very large. This offers insight into cross-talk behavior.

5.2 Cross-Talk Guidelines

The term cross-talk is used to describe the condition where an edge can no longer be treated as isolated. The non-ideal transmission from an edge interacts with another edge across a small gap or extension. This leads to a more difficult to model, pattern dependent source of error.

In Figure 5.2, a side-by-side comparison of the intensity, real, and imaginary 0th order field transmission, with data for pitches of 200, 400, and 1000nm is shown. All pitches show the trends of the MoSi absorber appears electromagnetically larger than the physical dimensions as field travels from the gap into the absorber, illustrated by EMF data shifted to the left of TMA. All pitches also show that TE and TM illumination cause edges to introduce imaginary transmission with opposite signs. The BL values from the 1000nm pitch simulations are roughly 26.7 + 4.2j for TE and 10.6 - 20.0j for TM, found by taking the average difference between the thin mask and EMF calculations normalized over the pitch. For the 400nm simulations, the boundary layer contributions were 23.8 + 4.3 for TE and 8.9 - 18.0j for TM. There is a slight difference in the values calculated due to pitch dependent effects as well as selecting the appropriate well-behaved interval. Looking at the 0th order field plots, the edge contributions is clearly not identical for all feature sizes, as periodic oscillations are apparent. These feature size dependent effects limit the accuracy of a BL model, but still serve as a good guide for fast CAD modeling.

For the large 1000nm pitch, there are clear trends in the center of the plots where both the gaps and absorbers are sufficiently large ($\geq$200nm). Here adding a simple bias to the thin mask layout could be used to reconcile the real errors, and imaginary boundary layers would correct the imaginary transmission. There are interference effects on the order of 1λ, but for sufficiently large features, the the oscillations are small in comparison to the overall deviation. This effect is most clear in the imaginary data. Near the extremes, where

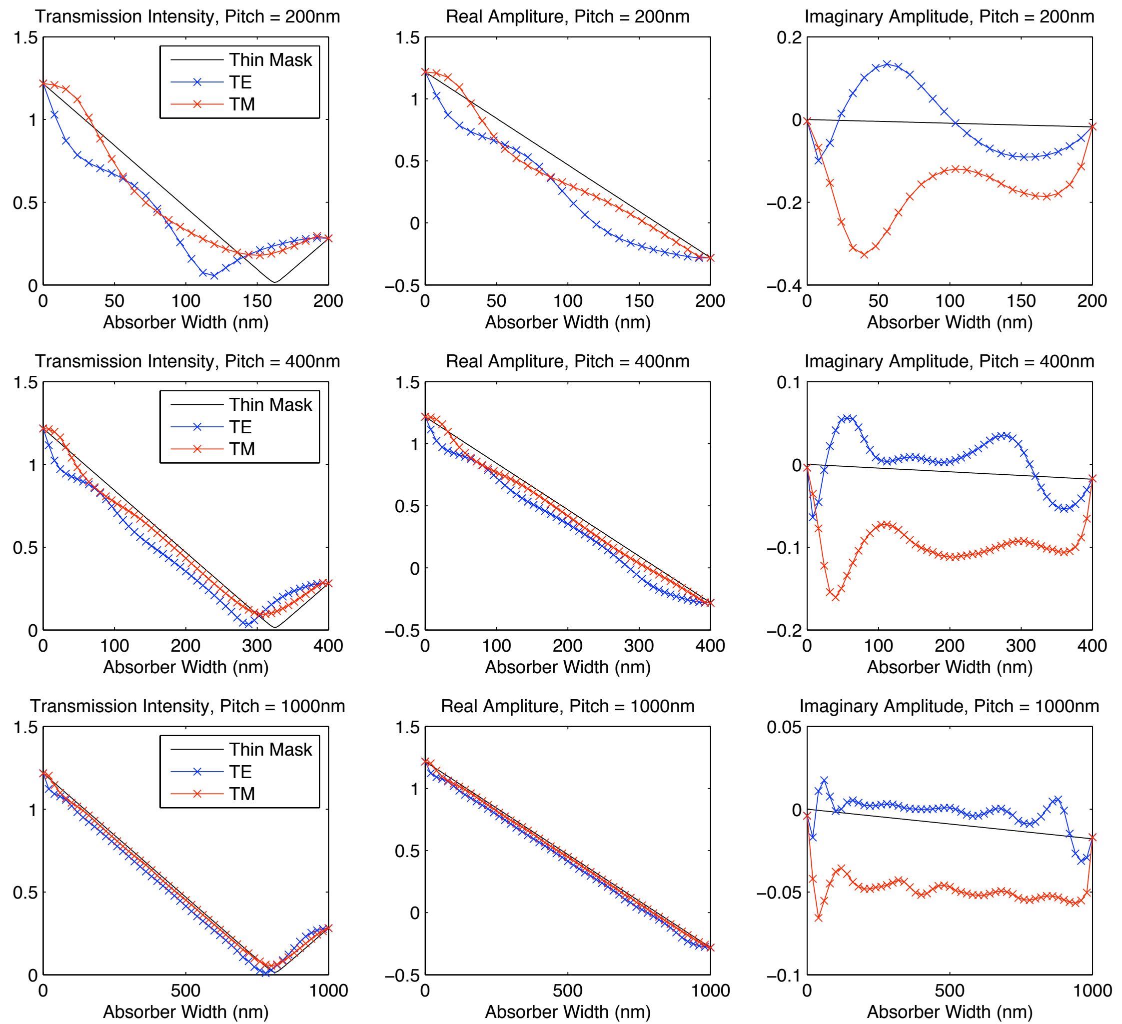

Figure 5.2: 0th order field transmission are shown. From left to right, the plots show intensity, real, and imaginary transmission. From top to bottom, 3 pitches are shown 200, 400, and 100nm with duty cycle changed along the x-axis.

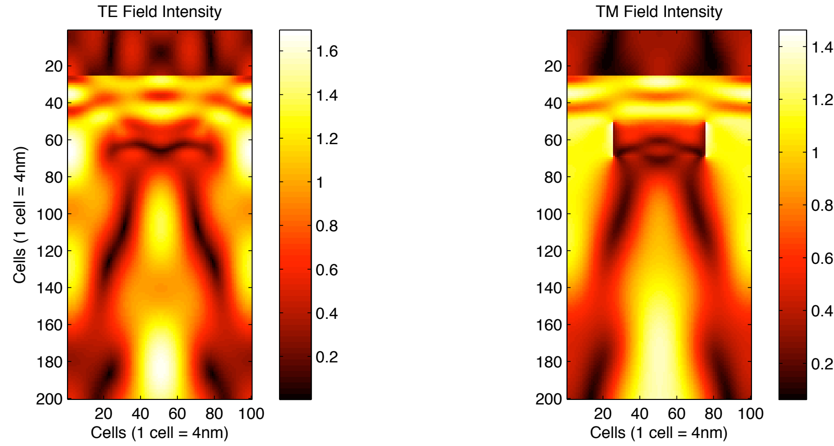

Figure 5.3: Field transmission intensity for TE and TM polarization.

absorbers and gaps are small, there is an additional jump in the fields. This implies that a BL approximation is very well suited for large features and gaps, but there is a limit. Looking at the imaginary fields, for small absorbers, the edge fields are well behaved for absorber widths larger than 100nm; however, for small and gaps there appears to be a polarization dependence on the transmission errors. The TM transmission is predictable for gaps as small as 30nm, but for TE the edge-to-edge interaction is closer to 150nm.

When comparing the vertical plots through pitch in Figure 5.2, one encouraging feature is that the tails of misbehaving field appear to have a feature dependence rather than pitch dependence. The ability to look at gap and absorber sizes alone without worrying about pitch is a step in the right direction to simplify BL modeling for general cases. However, BL modeling loses appeal once it is no longer simple. Once edge interaction dominates edge effects, modeling in this manner becomes more complicated. It appears that for a MoSi Att-PSM, at a pitch of 200nm (on mask), the absorber or gap is always too small for a simple model to apply, and for this blank is about the limit of simple BL modeling. With 4x reduction, a 200nm mask pitch corresponds to 25nm features. This is beyond what is targeted on wafer for single exposure using 193nm lithography, but with advanced RET techniques such as OPC, SMO, and SRAF, 25nm features well within the range of mask structure dimensions.

5.3 Alternate Mask Stacks

5.3.1 Ultra Thin MoSi

Mask materials are important to determining the transmission properties and resulting EMF effects, and the imaging capabilities mask materials through n/k space has been explored [16]. To test the effect of mask thickness on edge transmission, simulation was used to compare the transmission properties of 72nm MoSi to a made up material with twice

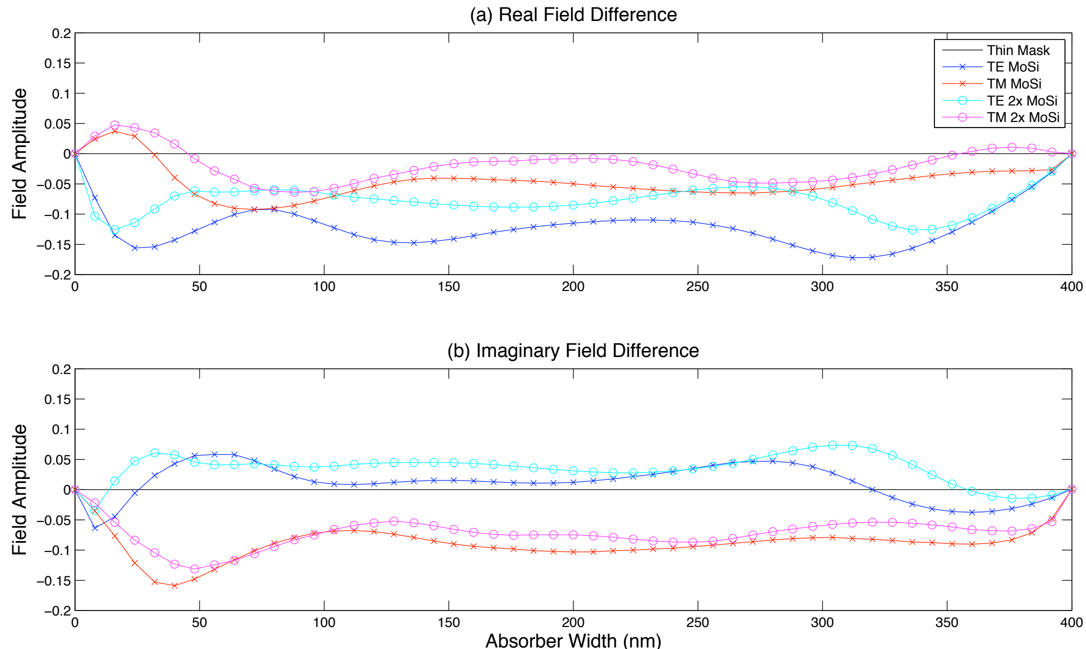

Figure 5.4: The deviation from TMA is plotted for MoSi and 2xMoSi (n = 4.686, k = 1.172).

the refractive index of MoSi (4.686 + 1.172j). With this material, a 28nm absorber is sufficient for transmission of 20.7% with a phase shift of 172.7^o. In this analysis, the error in diffraction orders were compared to the thin mask transmission calibrated through FDTD simulation, so the non perfect 180° transmission of the absorber was taken into account. By making the absorber thinner, there is a clear benefit in the shift of the real offset which makes the feature more true to the layout. This hold for both TE and TM polarization, shown in Figure 5.4(a).

The effect on the imaginary transmission is less straightforward. The non-idealities from very small gaps and absorbers are present in both and follow roughly the same trend. Both curves trend in the same direction, making the imaginary component of the TE boundary later more positive, while the TM component is less negative. With the thinner absorber, the TE and TM imaginary boundary layers are closer to being equal and opposite. Perhaps this edge cancellation can help to cancel out the unwanted quadrature transmission. A quick aerial image study shows that asymmetry through focus is less for TE and TM illumination together than for each individually. However, there is one clear conclusion which is that even though ultra thin absorbers may help with EMF effects, they do not resolve the issue of neighboring phase regions. For PSMs, there appears to be a fundamental phase behavior that cannot be fully engineered away using materials.

5.3.2 Thin Binary

At the time of writing, industry has moved toward replacing PSMs with ultra-thin binary masks. On mask proposed is called Opaque MoSi on Glass (OMOG). OMOG has been shown to perform better in terms of EMF effects [42, 11]. Because of proprietary information, it is unclear exactly what imaging tradeoff is made by no longer using PSMs to increase imaging flexibility and throughput. Because OMOG is a recently published material and a source of industry competition, index values were not available for comparison with existing MoSi Att-PSM mask blanks.

5.4 Near Field Effects for 3D Corners

Once edge behavior is understood for grating structures, the next steps is to address 2D layouts. FDTD simulation of a 3D line is required to see the effects of corners and the line end. 0th order transmission data is shown in Figure 5.5. For a long line test case, the simulation dimensions were 400x3000nm, with a MoSi line of 200x1800nm. All dimensions are on the mask, intended for 4x reduction on the wafer. Periodic boundary conditions were used, representing a dense line equal space pattern. Near the center of the line, the structure closely resembles a periodic grating. The values from the full 3D line pattern (blue and red curves) match those of 2D grating simulations (cyan and pink curves) when more than 400nm from the line end, but there is a ringing effect with periodicity of 1λ, and other non-idealities are introduced at the ends. By taking the average 0th order transmission at the center, and comparing it to the thin mask, the BL contributions are -23 + 3j for TE and -11-20j for TM. For long lines, the BL approximation holds.

One of the keys to extending the modeling to 2D layouts is assessing the agreement of the data form grating simulations. To see the extension from gratings to contacts and lines, several simulations were run with mask features of 200x200nm, 200x400nm, and 200x600nm. Several BL model schemes were then tested to see how closely they matched the EMF fields. The different BL schemes are shown in Figure 5.6. Ideally, the EMF effects can be accurately predicted by a single boundary layer to save time with imaging calculations and OPC. The simplest tests were with only TE, TM, or average BL values. The next was to use a dual BL, which takes into account that for any feature where one edge is exposed to TE light, the perpendicular edge sees TM polarization and vice versa. For unpolarized illumination, an average BL could match the 0th order transmission, but often polarized illumination is used for grating structures, where a single BL would apply [37]. Thus, in general the BL must be aware of the source and take into account different polarizations on each edge.

When comparing the simulation data to each model, for a single polarization the dual BL model was necessary to match the field transmission. The BL methods did not include corner sources, but an interesting commonality appeared for all 3 geometries and both polarizations. With the dual BL scheme, the real TMA transmission matched to within .8% transmission for all 6 simulations. The difference in imaginary transmission, when normalized over the entire area came out to a contribution on the order of a 30x30nm imaginary transmission source on the corner. For this set of simulations, adding this additional corner source made

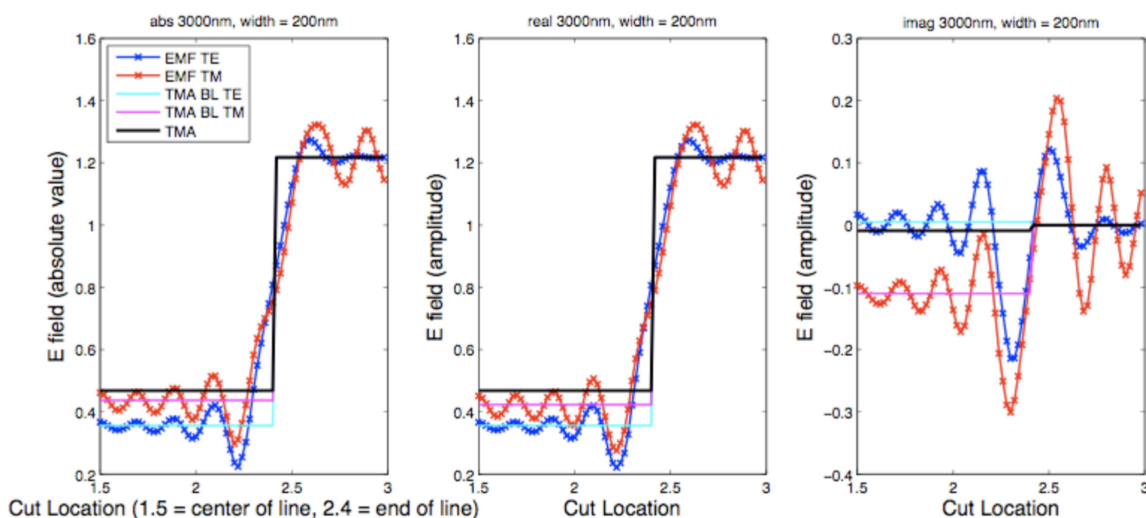

Figure 5.5: Field plots from a 3D simulation of a 1800x200nm line in a 3000x400nm simulation domain with periodic boundary conditions. 0th order field transmission taken at slices moving from the center of the line to the gap between line ends. EMF, TMA, and BL solutions are shown.

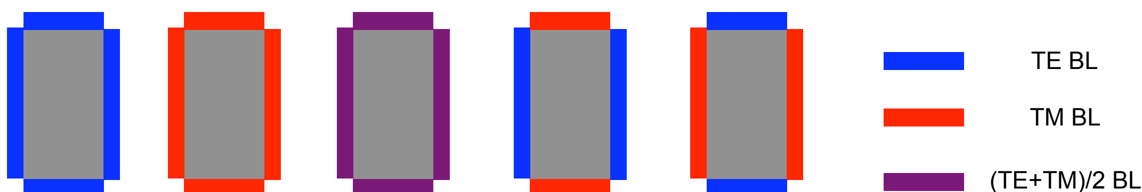

Figure 5.6: Different boundary layer schemes were compared to observe the importance of polarization dependence.

the fields match. More work is required to validate the generality of this type of modeling, but compensating corners with an additional source may be able to tie together 1D and 2D patterns.

5.5 Conclusions

Simulations of gratings and lines were used to characterize the real and imaginary edge contributions to EMF field discrepancy compared to a thin mask approximation, with the goal of developing a first order understanding for use with fast CAD modeling. Direct near-field analysis offers increased accuracy and a clearer look at feature dependent behaviors. By altering the duty cycle for a fixed pitch, the deviations in field transmission are directly observable and limitations are apparent. For a pitch smaller than 1λ on mask, boundary

layer approximations lose their predictability and usefulness. For TE polarization features larger than 100nm and gaps larger than 150nm appear to deviate from thin mask models in a predictable way. Similarly, for TM polarization absorbers larger than 100nm and gaps greater than 30nm show a consistent deviation and are characterizable.

From 3D simulations of 2D lines, it appears that for general illumination polarization must be taken into account because perpendicular edges see opposite polarization. A single BL is valid for unpolarized light, but more advanced illumination schemes require polarization aware boundary layers. With a small imaginary field correction of 30x30nm for corners, the dual BL model does well recreating the overall field transmission. The CD behavior for EMF and BL modeling are shown to match the opposite tilt from TE and TM polarization due to differences in sign of the imaginary field transmission. A test on the effect of mask thickness on the edge disturbances show that simply shrinking the absorber height does not resolve the phase mismatch and resulting out of phase transmission.

Chapter 6

Source-Pupil Kernel Convolution with Pattern Matching

This chapter extends full-chip kernel convolution to electromagnetic effects at mask edges as a fast-CAD tool, and more importantly develops a new formulation that overcomes the accuracy issues in the historical formulation, as well as automates the process of generating the kernels themselves. This revised method is called Source-Pupil Kernel Convolution with Pattern Matching (SP-KCPM). The generalization is made by including complex masks and complex spillover functions. The new formulation is based on coherent imaging, but includes off-axis source distribution, accounting for linear phase progressions. The automation is achieved by utilizing image simulation software to generate the pupil functions from which the kernels are determined. SP-KCPM incorporates a complex mask, flexible pupil function, and pixelated source distribution. This allows for aerial image estimation up to 10^4 faster than conventional imaging, with R^2 correlation above 0.99 in most cases, while adding a great deal of flexibility by building a general pupil-based platform. In particular, the pupil-based formulation can incorporate many aberrations, complex mask transmission, and no longer requires any previous information about the image.

SP-KCPM evolved from earlier and concurrent pattern matching work [25, 53, 55, 54, 33, 57, 58, 59] to satisfy the need for incorporating electromagnetic effects into full-chip image calculation. Studying the error trends with various sources led to the discovery of a new source and pupil based method. The complex nature of the phase error introduced by mask edges created the need for fully complex pattern matching, diverging from earlier methods where only real mask transmission was required. One of the initial goals of this work was to extend the algebraic formulation to mask transmission that contained complex phase in the presence of complex phases in the lateral spillover. During this research, however, a novel formulation was developed that is superior to the previously used Taylor series expansion of the pupil function.

The components and methodology of SP-KCPM will be discussed in the following sections. Section 6.1 explains the changes made to the three main lithography elements: Mask, Pupil, and Source. Next, the methodology for calculating intensity and change in intensity is presented. Finally, the capabilities of pattern matching are shown through several

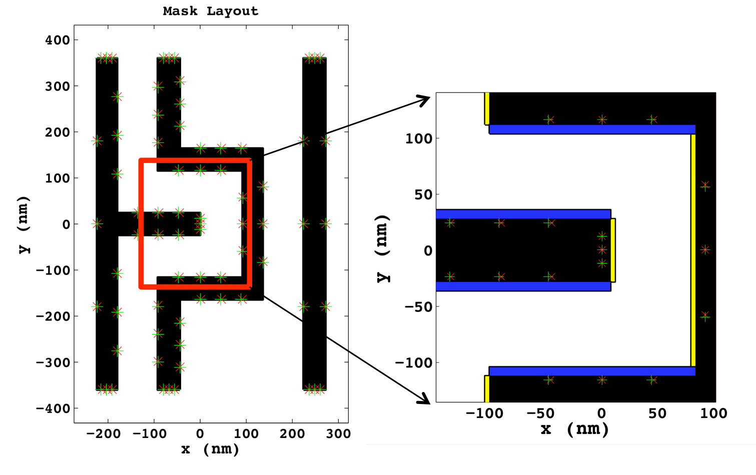

Figure 6.1: Boundary Layers for KCPM

examples in Section 6.3.

6.1 Automatic Kernel Generation for General Mask, Pupil, and Source

6.1.1 Complex Mask Transmission

As described in previous chapters, with shrinking mask dimensions relative to transmission wavelength, mask transmission can no longer be treated as ideal. For even the best behaving mask blanks like binary and attenuating PSM, edge effects can still become detrimental if not built into the design and simulation flow. As shown in Chapter 3, these imaginary phase mask effects result in a tilt of the process window and loss of up to 40% of the focus latitude.

In order to include EMF behaviors, it no longer makes sense to split the real and imaginary calculation, as has previously been done, since the interactions taking place are between complex mask transmission and complex spillover from aberrations. The pattern matching engine had been designed with the capability to handle real or imaginary patterns with multiple layer gds files, but to unlock the full functionality, additional investigations into normalization behavior was required. Complex mask transmission is addressed by attaching boundary layer transmissions to mask edges with both real biases and imaginary transmission corrections, described in earlier chapters. Additionally, pattern matching is now executed with complex math, enabling real and imaginary interactions to be calculated with only one match calculation. The result of this is mask edge effects can be pulled into the fast pattern matching framework, as well as the ability to include any effect that could be expressed as a transmission on the mask such as a buried defect in EUV lithography.

6.1.2 Generalizing and Automating Pupil Function Formulation

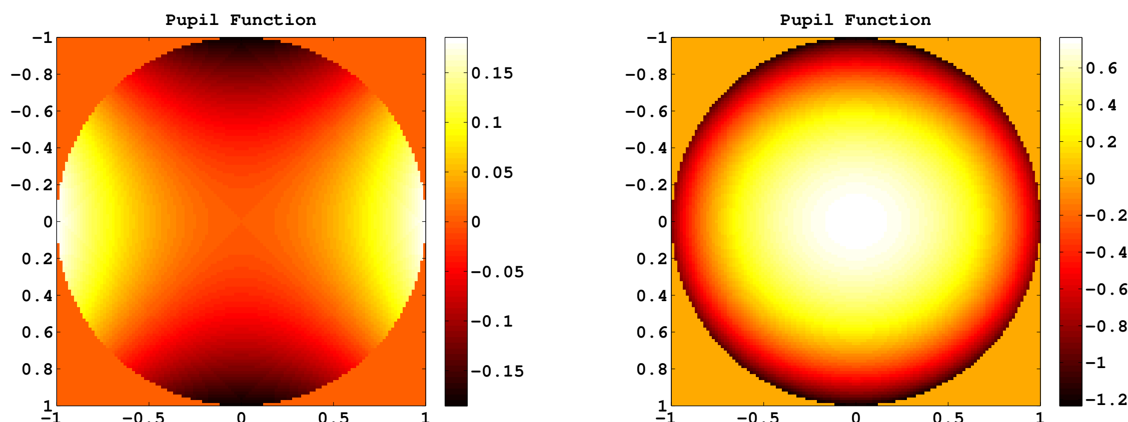

(a) (P): Pupil function for $.03\lambda$ RMS Astigmatism

(b) (P'): Pupil function for $60nm$ defocus and $.03\lambda$ RMS Astigmatism

Figure 6.2: Typical Pupil Functions

The pupil function is used to describe the path difference between light traveling at different angles through the projection system optics. The most common behaviors to be modeled are aberrations present in the system and defocus, which in modern steppers is significantly larger. Zernike polynomials are commonly used to describe these aberrations. As shown by several authors [53, 58], the Fourier transform (FT) of a specific Zernike polynomial can be used to describe the spillover of a point onto the surrounding area. This function describes the field distribution caused by a point source on the mask from the aberration in question. The spillover function can then be scanned over a layout to determine where the layout is similar to the spillover. When a high match is returned, the layout is similar to the maximum lateral interaction function, indicating high sensitivity to the aberration.

The new formulation for SP-KCPM generalizes this behavior to deal with the pupil directly, rather Zernike polynomials. In this revision, a path difference described by defocus, Zernike aberrations, or even measured tool errors can be directly combined into the pupil function. This allows for a great deal of flexibility because a set of aberrations can be expressed by the pupil function. In an unaberrated system, the FT of the pupil function is an airy disc, which is the field distribution created by a pinhole on the mask under coherent illumination. When aberrations are present, the resulting distribution becomes an aberrated airy function.

One important difference between FT[Pupil] and FT[Zernike] is that the pupil method includes proximity effects in addition to aberrations, while the Zernike analysis only calculates the behavior caused by the aberration. However, the pupil-based method can be used in a similar way to monitor process changes by taking the difference of the FT of two pupils.

$$E_{nominal} = FT[P] \tag{6.1}$$

$$\text{Spillover} = FT[P'] - FT[P], \tag{6.2}$$

where P' includes aberrations, and P does not. In the context of SP-KCPM, the term spillover is used to describe the field interaction or spillover caused by the change pupil. The initial pupil configuration is described as $E_{nominal}$.

Furthermore, this allows for the additional flexibility where P' and P can be expressed as P_{N+M} and P_N. In this context, it is possible to look at the effect of some changing aberrations while other aberrations are present. An example of this is calculating sensitivity to defocus in the presence of background aberrations. In this notation, P_N represents the default pupil with N aberrations from the projection system included and P_{N+M} describes the path difference of that system out of focus, where the subscript M is the focus effect. The fully general pupil representation can describes the electric field spillover from a point source as:

$$\text{Spillover} = FT[P_{N+M}] - FT[P_N] \tag{6.3}$$

By leveraging components from custom aerial image simulation tools, pupil-based kernel generation is automated and can be used with rigorous defocus, zernike aberrations, and measured aberrations in the current implementation. There is potential for including more effects such as polarization and resist into the pupil function in the future.

6.1.3 Generic Source Distribution

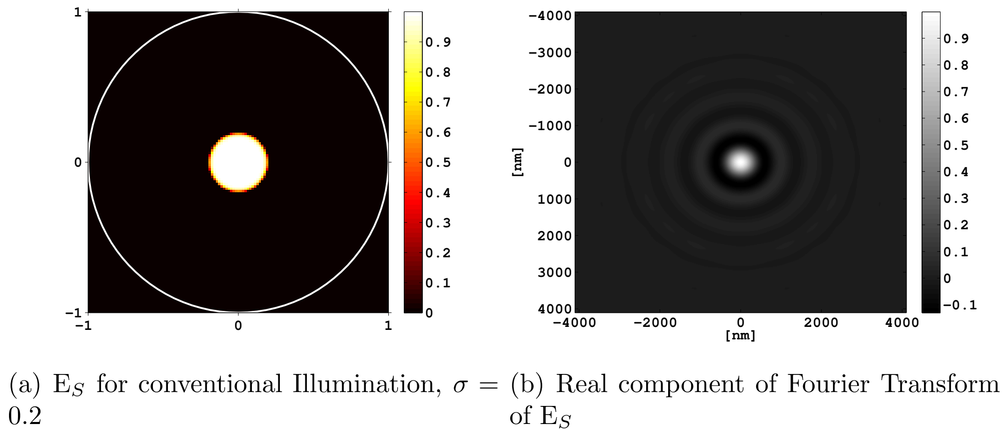

(a) E_S for conventional Illumination, $\sigma = 0.2$

(b) Real component of Fourier Transform of E_S

Figure 6.3: Source and source dependent point response for SP-KCPM

The description of the pupil analysis in the previous section implies a coherent on-axis point source. Having a coherent source makes the calculation simpler because a point

source fills the pupil uniformly. However, in practice as wafer dimensions shrink, all modern sources have some degree of partial coherence via dipole, quadrapole, annular or more extreme optimized illumination schemes. The conventional method for including the source behavior in KCPM is to use the FT[S], where S describes an intensity map of incident angle transmission [68]. In this context, FT[S] is the mutual coherence function, which describes the spatial field interaction in the mask plane.

For SP-KCPM, the source is treated in a slightly different way. Here, the source is expressed as field transmission, instead of intensity. This is described as $\mathrm{E}_S = \sqrt{S}$. The main consequence of this is that correlation is introduced among the pixels. In practice Köhler illumination insures that each source pixel is uncorrelated; therefore, they do not interact with one another and their intensities can be added. The correlation introduced in this new formulation creates a cross-term that introduces systematic source dependent inaccuracies.

For a single pixel stepped off axis, a linear phase is introduced from the off-axis incidence. With sources made up of a cluster of points, such as in Figure 6.5(a), the Fourier transform of the source ($\mathrm{FT}[\mathrm{E}_S]$), can be used to sum up each of these linear phase components to produce a point response incorporating the various source incident angles. For the purposes of SP-KCPM, when sigma is small (< 0.4), the correlation is not problematic to the algorithm, as will be shown in 7.1. This propagation model simplifies the source component of the field transmission, and the new transmission function is now described as:

$$\begin{aligned} E_{total} &= FT[E_S]FT[P_{N+M}] \\ &= FT[E_S]FT[P_N] + FT[E_S](FT[P_{N+M}] - FT[P_N]) \\ &= E_{nominal} + \Phi \end{aligned} \tag{6.4}$$

where:

$$\begin{aligned} E_{nominal} &= FT[E_S]FT[P_N] \\ \Phi &= FT[E_S](FT[P_{N+M}] - FT[P_N]) \end{aligned} \tag{6.5}$$

$E_{nominal}$ describes the initial field distribution before process changes are introduced. Φ describes the lateral field interaction caused by introducing the additional M effects. E_{total} describes the point response for all N and M effects incorporated into the pupil. These patterns can then be convolved with the mask to produce a SP-KCPM estimate of the field for the initial, total, and difference cases.

One additional issue is raised by the intensity vs. field view of the source. Take a simple example with two source pixels with identical strength and angle ($E_1 = E_2 = E$). In a lithography tool the intensities of the pixels can be added:

$$I_S = |E_1|^2 + |E_2|^2 = 2|E|^2 \tag{6.6}$$

But given the coherent assumption in SP-KCPM, fields are instead added resulting in:

$$E_{total} = E_1 + E_2 = 2E \tag{6.7}$$

And the corresponding intensity:

$$I_{E_s} = |E_{total}|^2 = |2E|^2 = 4|E|^2 \tag{6.8}$$

For this simple case, simply dividing the SP-KCPM result by two results in the desired value. By extending this logic to multiple pixels ($E_{s,i}$) of varying strengths, a general formula can be used to normalize the amplitude of an arbitrary pixelated source:

$$\text{Aerial Image} = [\text{SP-KCPM}]\frac{\sum_i |E_{S,i}|^2}{(\sum_i |E_{S,i}|)^2} \tag{6.9}$$

The normalization factor to recover the actual aerial image value from the SP-KCPM calculation simplifies to:

$$\text{Source Normalization Factor} = \frac{\sum \text{pixels}^2}{(\sum \text{pixels})^2} \tag{6.10}$$

This normalization factor is exact for pixels of the same incidence angle, but does not take into account the vector addition that takes place when pixels have different incident angles. Discussion of the angular consequences is discussed at length in Chapter 7. At first glance, moving from an intensity model to a field distribution appear to introduce unnecessary complications in normalization, but it is important to remember that the process variations of concern, such as edge effects, defocus, and other aberrations all interact with one another in field, not intensity. Additionally, by moving the errors to the source in the form of coherence, we can treat the behavior systematically (Section 7.3). With the intensity and mutual coherence source model, errors were layout dependent, making it extremely difficult to predict and control.

6.2 Novel Formulation for Intensity Estimation with SP-KCPM

The components described in the previous section are the main elements that were modified in the KCPM flow. A diagram of the full SP-KCPM flow is shown in Figure 6.4. An initial lithography condition is defined with source, pupil, aberration, λ, NA and other information. From here, the change pupil is created with the designated process changes. From this information, lateral interaction (or spillover) functions are produced and sent to the pattern matching engine. At the same time, a GDS can be given boundary layer values and sent to the engine. The resulting output from the pattern matcher is a single complex

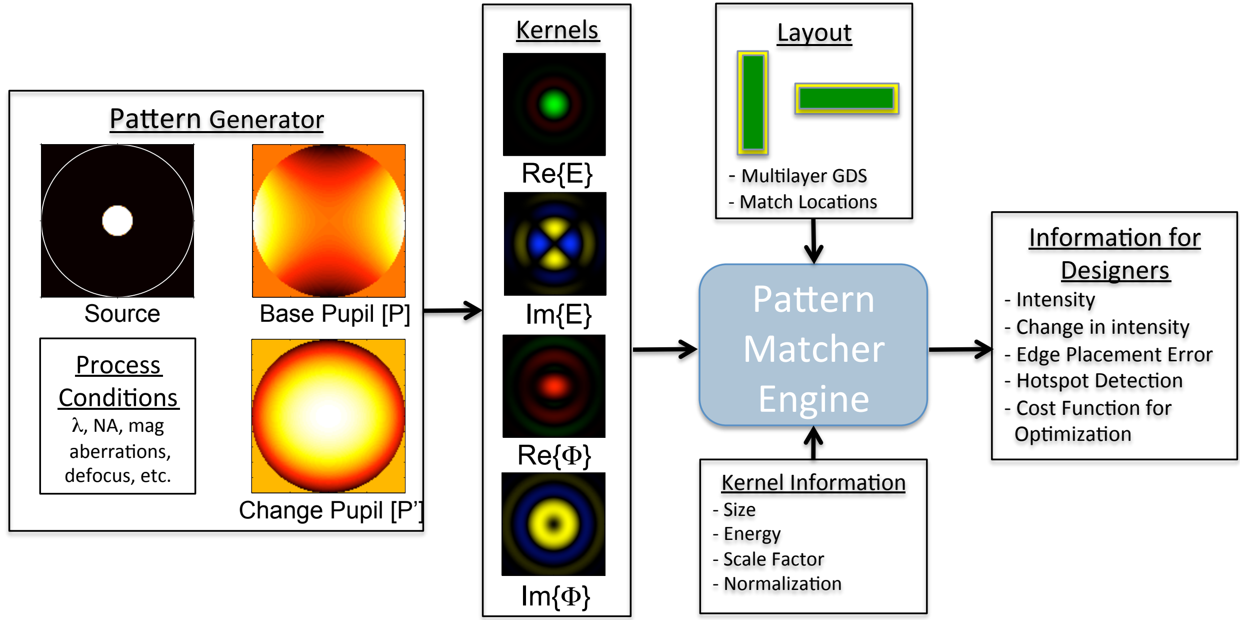

Figure 6.4: Block Diagram of SP-KCPM

value for each pattern at each match location describing the degree of similarity between the spillover patterns and the GDS layout. Alone, the match factor (MF) returned is of limited usefulness, but with careful normalization, scaling, and thresholding can be made to correspond to intensity directly.

6.2.1 Calculating Intensity

The new match factor (MF) describes field interaction, and therefore the square of the match factor is the value required for intensity prediction. The field at a particular location is calculated by:

$$\begin{aligned} \text{Field Transmission} &\approx FT[E_S]FT[P_{N+M}] \otimes Mask \\ &= E_{total} \otimes Mask \\ &= \text{MF}_{total} \end{aligned} \tag{6.11}$$

To calculate intensity, this value is multiplied by its complex conjugate, leaving:

$$\text{Intensity} \approx \text{MF}_{total}\text{MF}^*_{total} = \mid \text{MF}_{total} \mid^2 \tag{6.12}$$

As will be shown through examples in the following sections, this acts as an extremely accurate estimation of the aerial image. This process only requires 1 match pattern per location, making it extremely fast.

6.2.2 Calculating Change in Intensity

SP-KCPM has another operating mode more analogous to the classic pattern matcher formulation, which calculates change in intensity. Calculating intensity directly may be a more natural computation, but looking at the change in intensity can offer insight into sensitivity to different process conditions. For this, the difference of two pupil functions is required, as well as two match patterns. Starting with the result from Eq. 6.12:

$$\begin{aligned} \text{Intensity} &\approx \text{MF}_{total}\text{MF}^*_{total} \\ &= (\text{MF}_{nominal} + \text{MF}_{\Phi})(\text{MF}_{nominal} + \text{MF}_{\Phi})^* \\ &= \text{MF}_{nominal}\text{MF}^*_{nominal} + \text{MF}_{nominal}\text{MF}^*_{\Phi} + \\ &\quad \text{MF}^*_{nominal}\text{MF}_{\Phi} + \text{MF}_{\Phi}\text{MF}^*_{\Phi} \end{aligned} \tag{6.13}$$

Now the total intensity can be de-coupled into the nominal field and the spillover. By removing the nominal self interaction, change in intensity is calculated as:

$$\Delta I \approx \text{MF}_{nominal}\text{MF}^*_{\Phi} + \text{MF}^*_{nominal}\text{MF}_{\Phi} + \text{MF}_{\Phi}\text{MF}^*_{\Phi} \tag{6.14}$$

The significance of Eq. 6.14 is the inclusion of the nominal-spillover interaction terms. In earlier manifestations of pattern matching, only the spillover term was incorporated. With this formulation ΔI can be calculated directly. Additionally, the $\text{MF}_{nominal}$ term can be reused. For example, to calculate one focus level, two patterns are required, but to calculate two focus levels, only three patterns are needed. One of the important implications of the initial field estimate described by $\text{MF}_{nominal}$ is that the calculation of ΔI does not require any external information. Without this component, an initial estimate of the field would be needed from a prior simulation. This adds the flexibility to monitor points that do not fall on a specific contour in the image plane.

6.2.3 Spillover vs. Spillback

The intensity calculation as formulated in the previous section relies on convolution of the point response across the layout to generate an aerial image estimate. When dealing with a subset of target points rather than the full image, there is a trick to enable faster calculation of the same quantity. As shown in Figure 6.5, this can be captured in the subtlety between spillover and spillback. For the purposes of this thesis, spillover describes the convolution of the match pattern with the entire layout. For a given value, the spillover must be calculated from every neighbor to add up the field interaction from the surrounding points. Spillback is used to describe the flip through the origin (left-right and up-down flip) of the spillover pattern. When the pattern is simply flipped in this manner, one multiplication centered at the target location can be used to calculate and add up the field from all of the neighboring points in one computation. This change in pattern orientation maximizes the efficiency of the pattern matcher engine, which excels at pixel-based multiplication. Of course, in the limit of matching at every grid location, the spillover and spillback views converge to the

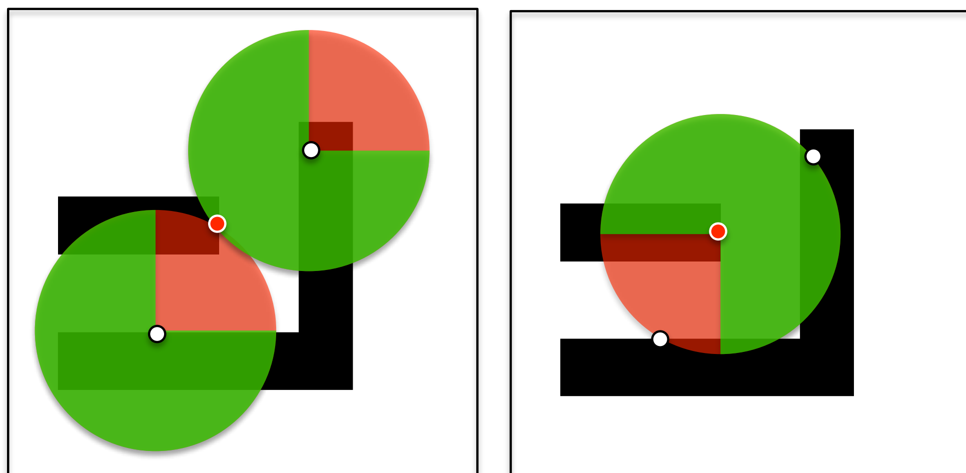

(a) Spillover: Field from neighboring pixels calculated through convolution. Each point spills onto target location.

(b) Spillback: Flip spillover through origin and pixel by pixel multiply. Spillback from all neighboring pixels calculated at once.

Figure 6.5: Spillover vs. Spillback

same computation, but many applications of SP-KCPM can leverage spillback to reduce computation time.

6.3 SP-KCPM Examples

For the following examples, the pattern shown in Figure 6.6 inspired by Dai [19] is used. The pattern has 45nm features and is designed to have a wide range of feature types: dense, isolated, line ends, jogs, and T-junctions. Three hundred sixty points were examined on all segments of the layout to capture performance across all of these layout features. The goal is to make sure SP-KCPM is robust enough to handle both good behaving and bad behaving layout sections. For the examples in this chapter, a binary mask model was used.

For the case with boundary layers, polarization dependent corrections are added to the features. The vertical edges see TE illumination, and the horizontal edges TM. The representative boundary layers attached to the layout include real biases of 8nm and 4nm for TE and TM respectively, where the features are grown to reflect the absorber region appearing electromagnetically larger than the physical drawing. Additionally, imaginary transmission boxes are drawn on the outside of the features of 4nm at 90° for TE and 8nm at 270° for TM. The points monitored are the same for both cases with and without boundary layers, thus because the real bias leads to larger absorbers, the overall intensity is often lower. For the comparisons between SP-KCPM and aerial imaging, the goal is to have them match one another rather than match rigorous FDTD simulation. Therefore, the boundary layer corrections are merely representative and not meant to model the exact rigorous solution.

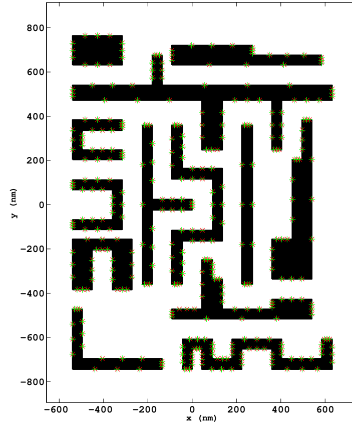

Figure 6.6: 45nm Test Pattern

6.3.1 Defocus with Top-Hat Illumination

For this case, on-axis illumination with $sigma = 0.15$ was used, shown in Figure 6.7(a). The base case for $E_{nominal}$ is the unaberrated case. The process conditions monitored are 6 different focus steps of -60nm, -40nm, -20nm, 20nm, 40nm, and 60nm. A representative pupil with 60nm of defocus is shown in Figure 6.7(b). For this scenario, to look at change in intensity 7 patterns are required, one for $E_{nominal}$ and six to calculate the six focus levels. $E_{nominal}$ is shown in Figures 6.7(c) and 6.7(d). Real and imaginary spillover functions for 60nm of defocus are shown in Figures 6.7(e) and 6.7(f). The imaginary part of $E_{nominal}$ is essentially zero, but numerical noise leads to a pattern on the order of 10^{-17}, which is treated as zero.

The results comparing SP-KCPM to full Abbe aerial image calculation are shown in 6.8. For all cases with and without boundary layers and for intensity and change in intensity, correlation is greater than 0.997. The most significant result is that the horizontal axis is calculated about 10^4 faster than the vertical axis. In general, the speedup is dependent on many factors such as number of match locations and match patterns. One important result is that the six defocus levels all fall on the same trend-line, demonstrating that calibration to specific conditions is not required. Additionally, SP-KCPM was given no prior knowledge of the feature type or initial imaging contour. All the information required for accurate results are contained in the $E_{nominal}$ match pattern.

6.3.2 Coma with off-axis illumination

For this example, SP-KCPM is run in a mode analogous with the classic formulation of matching zernike targets. Here small $\sigma = 0.1$ illumination with a rounded profile (Figure 6.7(a)) was used. Like the previous example, the nominal case is unaberrated. Instead of calculating defocus, this example looks at the image sensitivity to zernike coma, by adding

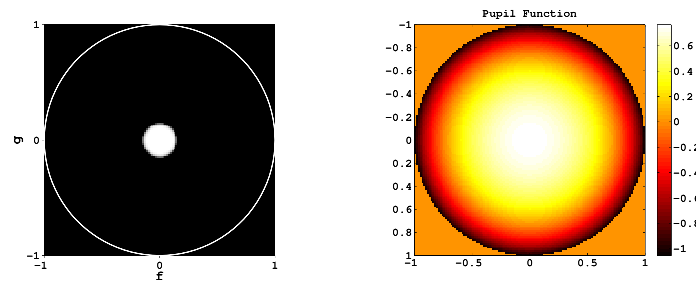

(a) Conventional Illumination, $\sigma = 0.15$ (b) Pupil function for $60nm$ defocus

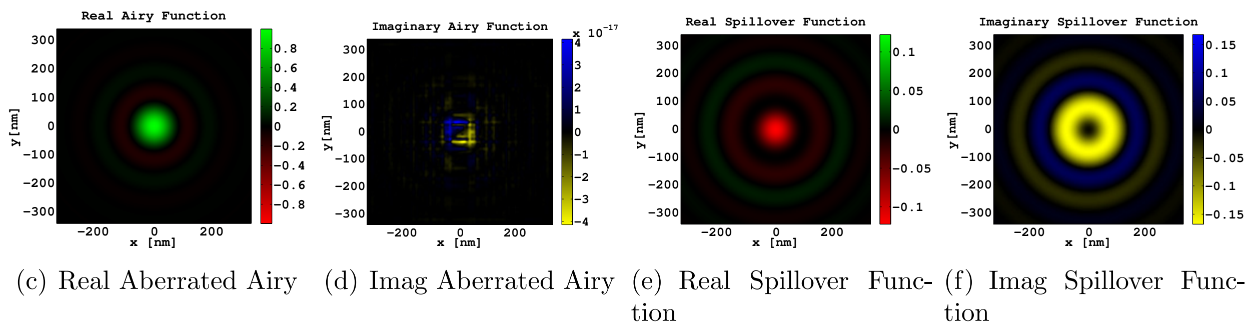

(c) Real Aberrated Airy (d) Imag Aberrated Airy (e) Real Spillover Function (f) Imag Spillover Function

Figure 6.7: Simulation conditions for observing defocus with conventional small σ illumination

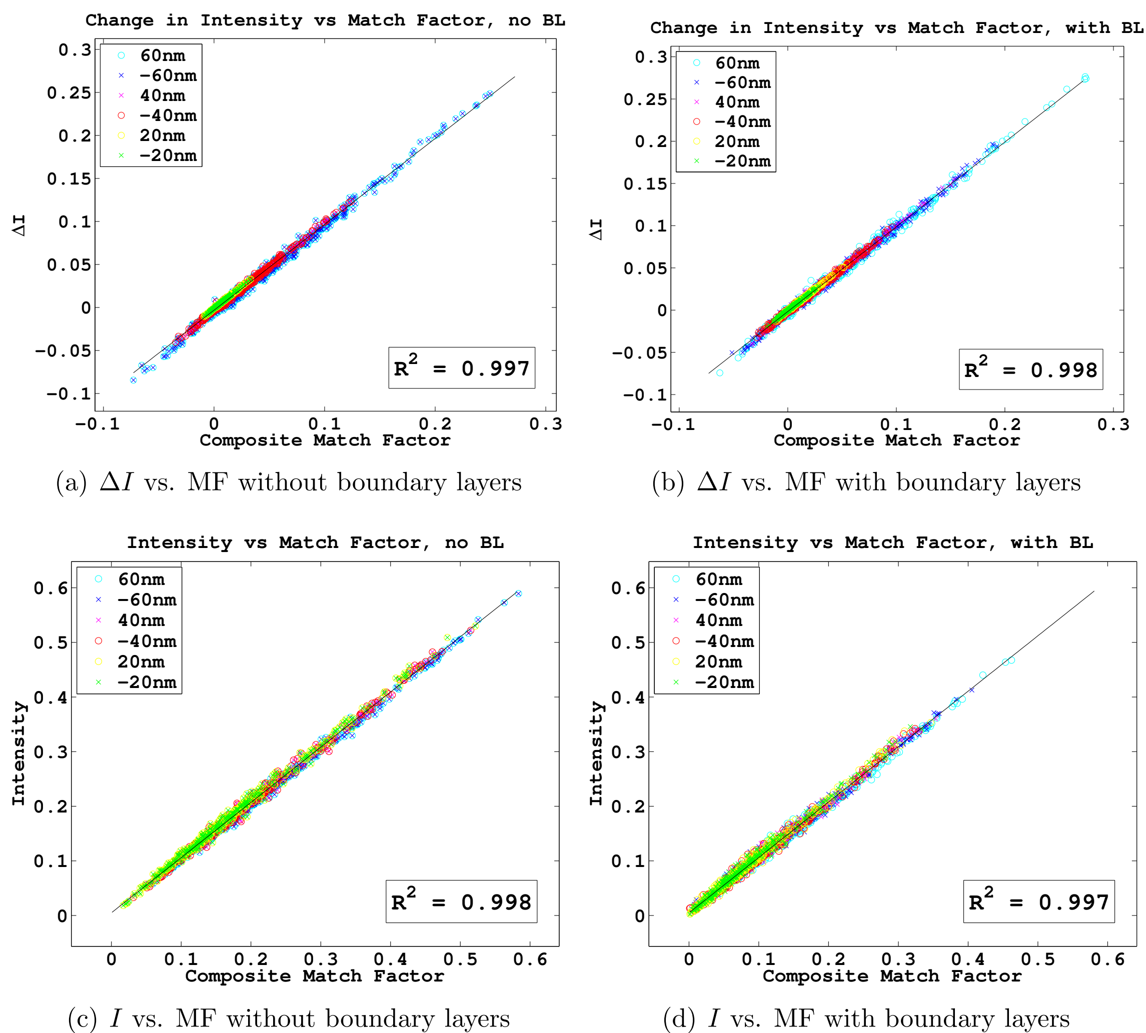

(a) ΔI vs. MF without boundary layers

(b) ΔI vs. MF with boundary layers

(c) I vs. MF without boundary layers

(d) I vs. MF with boundary layers

Figure 6.8: Correlation Data for Defocus Example

0.05 λ RMS of coma to the aberrated pupil function. Here one pattern represents $E_{nominal}$, and a second contains the Φ behavior caused by coma. On interesting note about coma is that unlike defocus, the imaginary component of Φ is zero, as demonstrated in early pattern matching work.

The correlation between SP-KCPM and aerial image is shown in Figure 6.10. Correlation in calculating coma is above 0.997, similar to the previous defocus example. This demonstrates an additional operating mode where zernike or other aberrations can be monitored in addition to defocus. Another variable added to this example is the rounded source, where the center transmission is 1, but gradually rolls off instead of a sharp boundary.

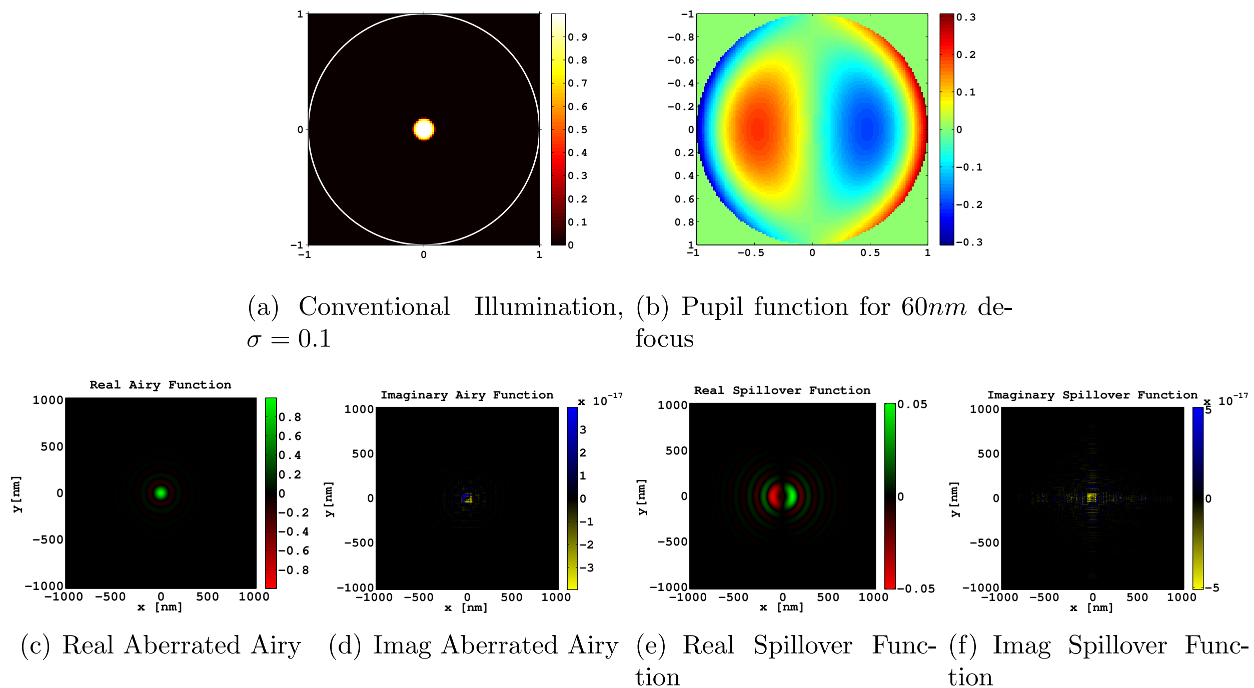

(a) Conventional Illumination, $\sigma = 0.1$

(b) Pupil function for 60nm defocus

(c) Real Aberrated Airy

(d) Imag Aberrated Airy

(e) Real Spillover Function

(f) Imag Spillover Function

Figure 6.9: Simulation conditions for observing defocus with conventional small σ illumination

6.3.3 Dipole with Background Aberrations

The final example in this section adds in more complexity. The source (Figure 6.11(a)) is now an asymmetric dipole, where the two poles are asymmetrically located and of unequal strength. Additionally, the nominal pupil function contains 0.03λ RMS coma and astigmatism (Figure 6.11(b)). Here we look at the pattern sensitivity to defocus in the presence of these zernike background aberrations (Figure 6.11(c)). As shown in Figures 6.11(d) to 6.11(g), the $E_{nominal}$ and Φ interaction functions are far more complicated and less intuitive than the simpler symmetric cases.

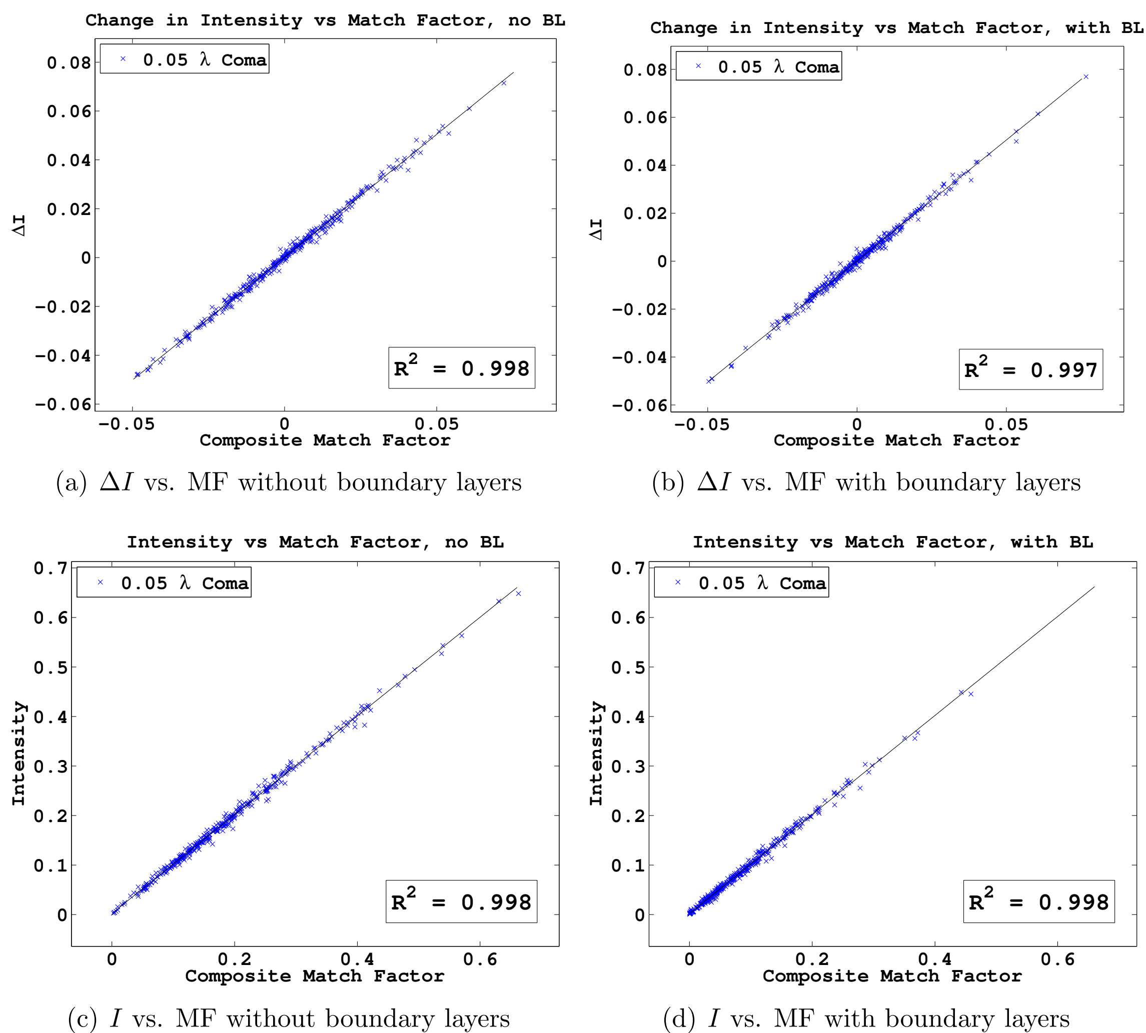

(a) ΔI vs. MF without boundary layers

(b) ΔI vs. MF with boundary layers

(c) I vs. MF without boundary layers

(d) I vs. MF with boundary layers

Figure 6.10: Correlation Data for Coma Example

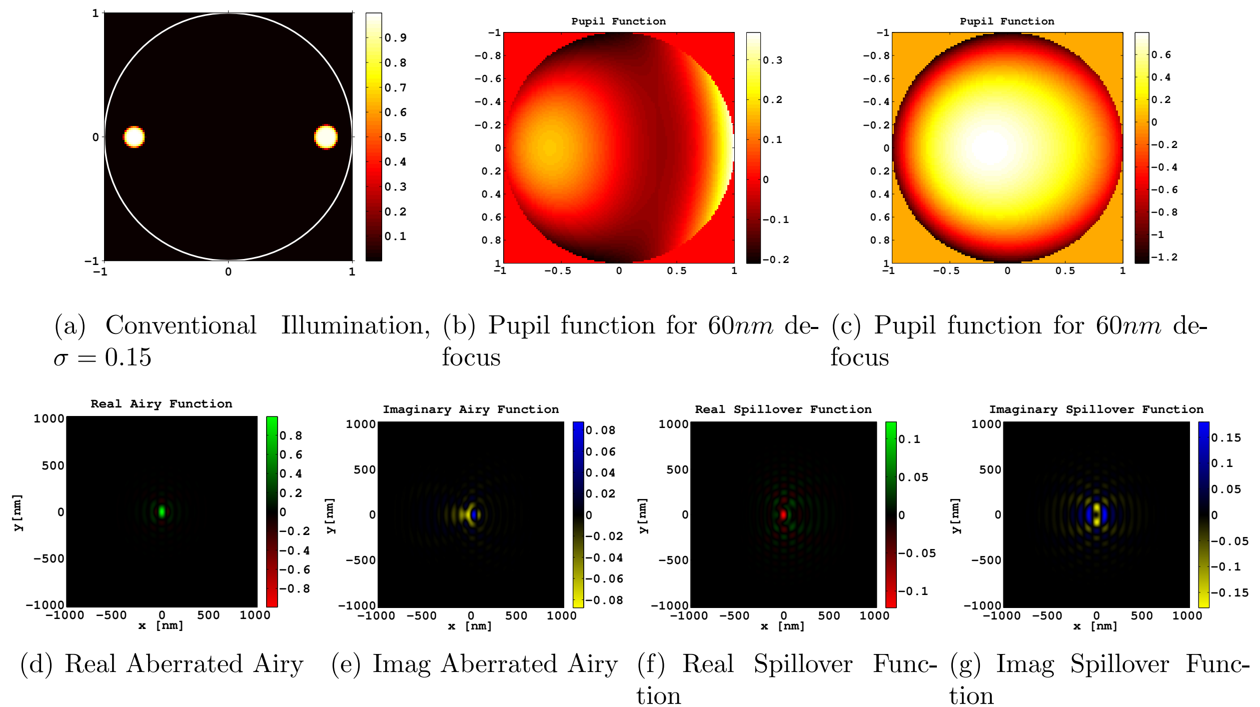

(a) Conventional Illumination, $\sigma = 0.15$

(b) Pupil function for $60nm$ defocus

(c) Pupil function for $60nm$ defocus

(d) Real Aberrated Airy

(e) Imag Aberrated Airy

(f) Real Spillover Function

(g) Imag Spillover Function

Figure 6.11: Simulation conditions for observing defocus with conventional small σ illumination

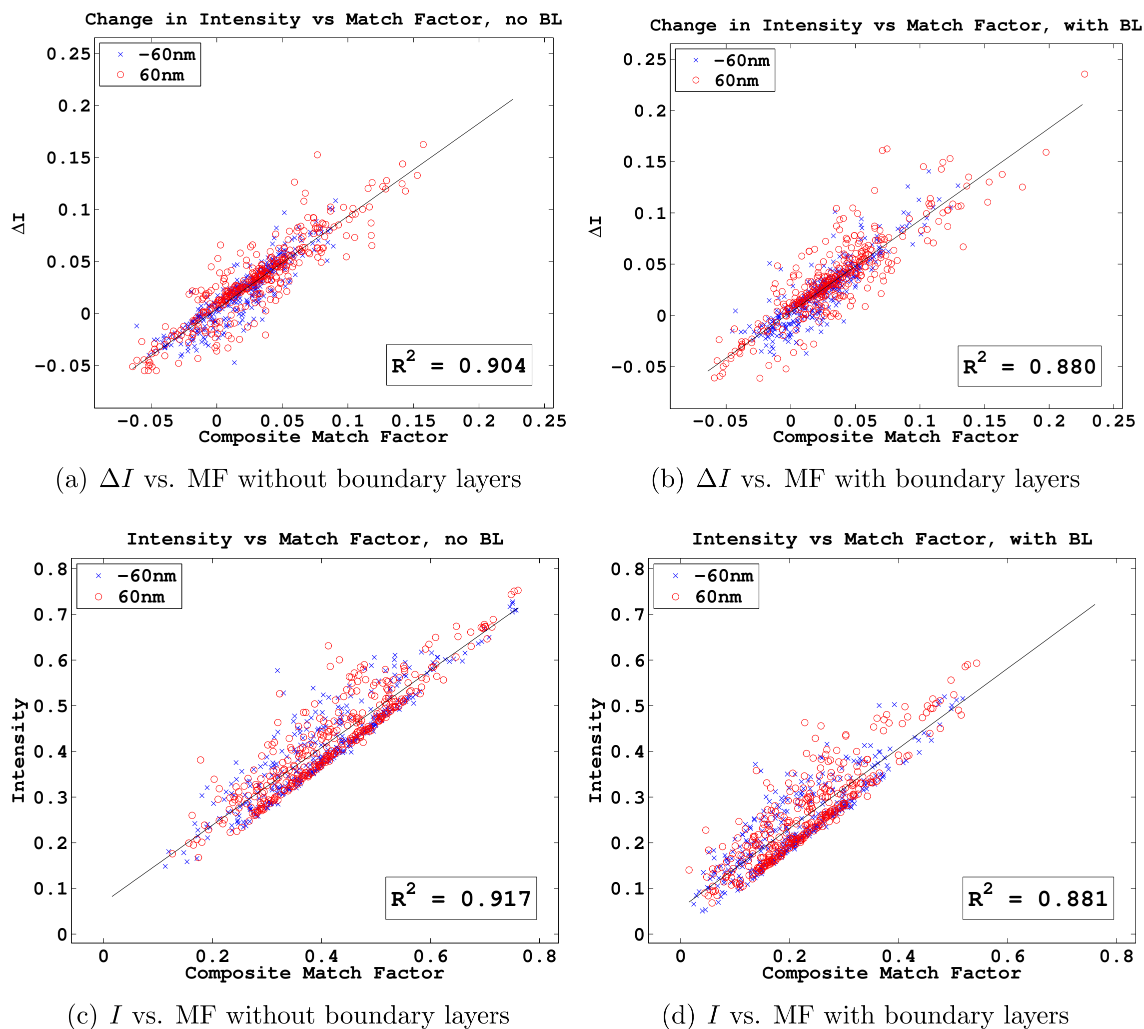

(a) ΔI vs. MF without boundary layers

(b) ΔI vs. MF with boundary layers

(c) I vs. MF without boundary layers

(d) I vs. MF with boundary layers

Figure 6.12: Correlation Data for Dipole Example

The results shown in Figure 6.12 are far less accurate than the previous 2 cases. For the ΔI calculation (Figures 6.12(a) and 6.12(b), the R^2 correlation is on the order of 0.90, which is reasonable for hotspot detection applications. Similarly, for the total intensity calculations, Figures 6.12(c) and 6.12(d), correlation is around 0.90, but a systematic error appears. There is a group of well-behaving points that would nicely fit on a trend-line, but there are many outliers away from the main mass. This is caused by a source dependent issue with the initial SP-KCPM source approximations. This problem is examined and treated in detail in the following chapter. This example is revisited in Section 7.3.1 once the cause of this behavior is discussed further. A solution is also presented.

6.4 Conclusions

The capability of Source-Pupil Kernel Convolution with Pattern Matching (SP-KCPM) to calculate image variation in the presence of defocus and other aberrations with R^2 correlation of 0.99 compared to full aerial imaging was demonstrated for sources of $\sigma \leq 0.2$. The complex formulation seamlessly integrates mask edge effects via boundary layer modeling. Using pupil function directly provides the ability to look at M variations in the presence of an existing scenario with N effects. This also includes proximity effects, which when combined with an initial $E_{nominal}$ estimate remove the need for any prior information about feature type or restriction of the calculation to a specific image contour.

At about 40 μs per match per kernel on a 2.4 GHz laptop, SP-KCPM offers orders of magnitude speed improvement over full image calculation. When using small sigma illumination, correlation is above 0.99. Introducing dipole style illumination strays further from the initial coherence assumption, leading to correlation closer to 0.9. However, the trends in the dipole data indicate that there is a physical reason for this. The next chapter explores the shortcoming exposed by dipole illumination and develops a highly accurate solution for even the most challenging high-off axis sources such as those used in source mask optimization.

Chapter 7

Source-Pupil Kernel Convolution for General Source Distributions

A solution for handling partial coherent effects from advanced off-axis sources in the Source-Pupil Kernel Convolution with Pattern Matching framework is presented. Dipole and other sources with a wide range of incident angles confound the coherence assumption in the basic SP-KCPM formulation. The coherence assumption is treated more carefully to determine the usefulness and limitations. By splitting the source into smaller regions which behave more like coherent illumination, we can regain the high correlation of 0.99 already demonstrated for small sigma illumination.

We begin by examining two calibration examples to observe source dependent behaviors in KCPM to clearly demonstrate where the coherence assumption breaks down. In Section 7.2, the theory of source modeling is treated. Lastly, several new examples are shown with the revised source splitting method.

7.1 Calibration Examples

For the calibration examples the test pattern shown in Figure 6.1.1 was used to look at typical layout concerns. Three hundred sixty points were examined on all segments of the layout. For all cases, layouts were simulated for a binary mask both without and with BL additions to model EMF effects. Representative polarization dependent boundary layers were used to illustrate SP-KCPM flexibility. On vertical segments, TE boundary layers with 8 nm bias and 4nm 90° transmission were added. On the horizontal edges, TM values of 4 nm bias and 8nm 270° transmission were used. All BL values are in wafer dimensions. Various source configurations are explored in the following sections, with simulation conditions of $\lambda = 193nm$, with 1.35 NA immersion lithography. For all tests, SP-KCPM was compared to full aerial image simulation.

For the following two examples in this section, the match patterns used were 512x512 4nm pixels, making the patterns span 2048nm. For the first two cases, there are no background aberrations, so the N initial case is the unaberrated pupil function. The M effects in this case are $\pm 60nm$ rigorous defocus, each described by its own spillover function.

7.1.1 Off-axis Illumination

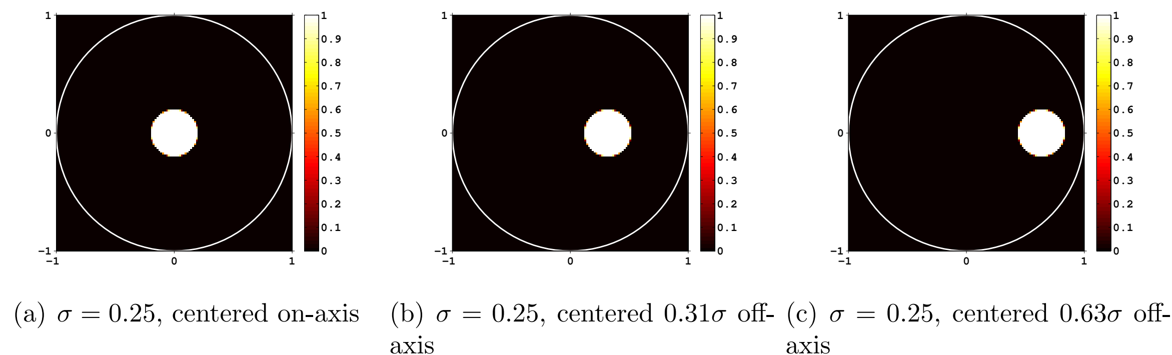

(a) $\sigma = 0.25$, centered on-axis (b) $\sigma = 0.25$, centered 0.31σ off-axis (c) $\sigma = 0.25$, centered 0.63σ off-axis

Figure 7.1: Source configurations for off-axis calibration.

The characterization of how the accuracy depends on illumination begins with the case of a small monopole, $\sigma = 0.15$, that was shifted off axis (Figure 7.1). The aggregate R^2 correlation factor is shown in Figure 7.2 for each source configuration. On this plot, each data point comes from a scan of 360 match locations, from which the correlation was extrated. For this off-axis test, $R^2 > 0.99$ even as the source incidence is moved to the edge of the source plane. The correlation values for the cases with and without boundary layers are nearly identical. The source approximations presented in Section 6.1.3 accurately models an off-axis incident illumination.

7.1.2 Effect of Partial Coherence

Next, SP-KCPM was evaluated for several partially coherent top hat sources (Figure 7.3), where the source was varied from very small, nearly coherent σ of 0.05, in steps of .05 up to 0.80. The results for the R^2 correlation factor are shown in Figure 7.4. Unlike the previous off-axis example, the results were not well behaved when the source size is increased. At $\sigma \approx 0.6$, the correlation has dropped to .95, and then falls off sharply when increased further. The positive result from this plot is that correlation remains high, even for source distributions approaching $\sigma = 0.5$. However, there is a problem with sources of larger angular distributions, and this must be treated to maintain high accuracy.

There are also a few other subtle features in Figure 7.3. For extremely small σ, there was a drop in correlation, which in this case is related to the kernel size. For a small, nearly coherent source, the spillover function decays more slowly as features interact from a greater distance. For this example, when the kernels were cut to 2048nm, information was lost from the edge of the spillover function leading to reduced correlation and larger ΔI. Once σ was increased slightly, the $FT[S]$ became more compact resulting in the spillover interaction distance becoming smaller and a larger portion was captured by the 2048nm pattern. This illustrates an important quality of SP-KCPM, where the source influences the necessary conditions for kernel size to obtain a given error tolerance.

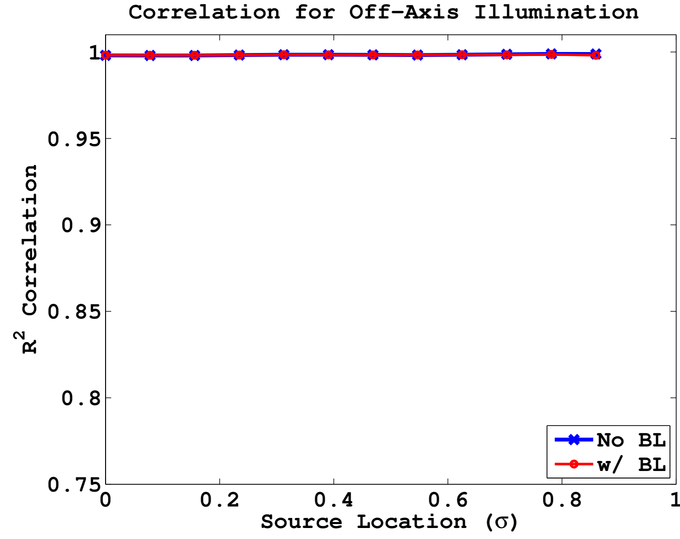

Figure 7.2: Left, R^2 correlation and right ΔI error plotted vs center location of monopole source.

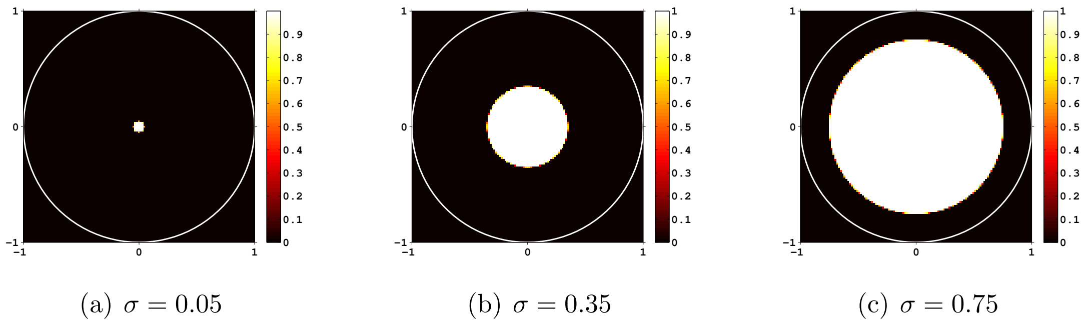

(a) $\sigma = 0.05$ (b) $\sigma = 0.35$ (c) $\sigma = 0.75$

Figure 7.3: Source configurations for on-axis coherence calibration.

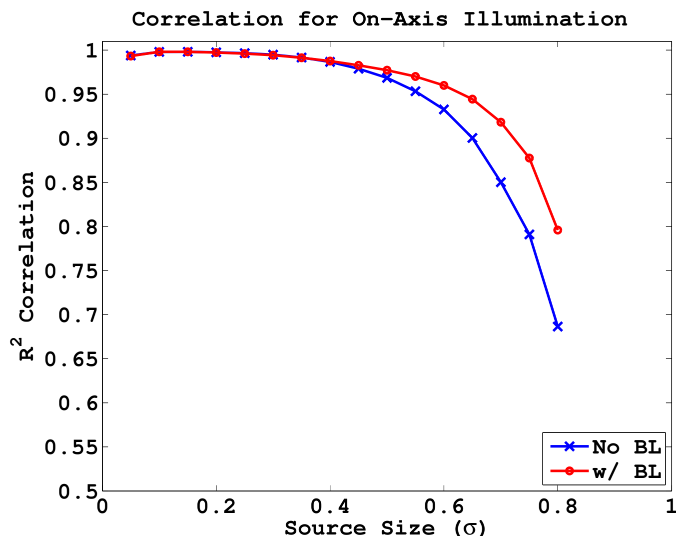

Figure 7.4: Left, R^2 correlation and right ΔI error plotted vs degree of partial coherence for sources centered on-axis.

Additionally, the correlation drops off faster for the case with no boundary layers. When real biases are added, the match location occurs inside the feature, leading to a darker image. When the approximations breakdown, for the case with boundary layers, the overall field is lower at the match locations making the change due to focus smaller in absolute terms. This indicates some potential mask dependence in the correlation factor, but in practice pattern matcher would be used along relatively similar image contours, making this a minor issue.

7.2 Limitation of Coherent Source Assumption

As described in Section 6.1.3, in the formulation of SP-KCPM, the source is modeled as a field distribution. This leads to an implied, and unwanted, coherence introduced between pixels. When a source pixel is moved off axis, a linear phase is introduced (Figure 7.5). In the case of two pixels with similar incidence, this linear phase is small, and the error can be normalized away by Eq. 6.10. However, it is important to be aware of this behavior as it differs source pixel by source pixel. This difference in linear phase behavior becomes more profound for large sources and can give insight into the correlation roll off behavior in Figure 7.4.

The spillover patterns are built from the source and the pupil (Eq. 6.5). Figure 7.6 compares the field distribution for a pinhole on the mask for top-hat source configurations of several σ sizes, and the relationship to the Airy function, calculated from the diffraction limited pupil for NA = 1.35. Here for small $\sigma = 0.02$, the field pattern created by the source is almost constant. This indicates that the source approximation is working well because the Airy pattern drops off before the source field distribution. As σ increases up to 0.4, the

source field collapses, reducing the accuracy of the coherent assumption.

An alternate way of looking at this phenomena is in the parallel to Rayleigh's quarter wavelength rule [13]. The rule states that for aberrations, most often defocus, the condition $|\Phi_{max}| = \lambda/4$ serves as a rule of thumb for estimating the tolerance of aberrations in an optical system. For defocus, this situation occurs where the phase difference from the center to the edge of the pupil is 90°. In this scenario, most of the fields are interacting well or in the case of SP-KCPM calculated correctly, and the errors are small relative to the well behaved region. As depicted in Figure 7.5, for two pixels in phase at point X_o, there is a phase error induced at a point X some distance away. By comparing the wave number of the incident plane waves, it is straightforward to calculate a distance from X_o where the waves will be 90° out of phase. For on axis illumination of a disc with radius σ, Figure 7.7 shows the distance where the outermost pixel would be 90° out of phase with the reference center pixel. A reference line shows where the peak of the third lobe of the Airy pattern falls. These curves intersect at about $\sigma = 0.27$, which matches roughly the location where the correlation falls off for increasing σ. The Rayleigh rule is an approximate criteria, but offers insight into the limitations of the coherent source model by viewing it as an aberration behavior.

By assuming that the source is coherent, the amplitude and linear phase of each pixel is calculated and the FT[S] represents the sum of the field from each source pixel. This helps maintain accuracy for sources of non-standard pixelated distributions and of varying pixel weights. However, in the real world, each pixel response is added in intensity, not field. Because aberrations and EMF effects are all errors in field, it is necessary to operate in a field regime when calculating their impact, but there is a tradeoff when modeling general illumination conditions. Understanding the phase behavior in the source distribution gives insight into where the errors are coming from, a metric to monitor them, and even a solution to reduce them for complicated source distributions.

7.3 Source Splitting: Hybrid Abbe SP-KCPM

Given the source view in 7.2 and supporting data from Figure 7.4, as long as a source-induced phase errors are small enough, the coherent source model provides high accuracy and correlation. The straightforward way to remedy this is to make sure that the source distribution being modeled satisfies the Rayleigh rule or simply the calibration data, which implies that $\sigma = 0.2$ is accurate to R^2 of 0.99, $\sigma = 0.3$ should be accurate to R^2 of 0.98, and $\sigma = 0.4$ is accurate to R^2 to 0.97. Because of the wide range of source, mask, and pupil configurations there is some problem-dependence built in to deciding on what size source is required. For sources that would not fit in a circle of 0.4 in σ space, we can treat different source regions as separate image calculations. This modification can be viewed as a Hybrid Abbe-KCPM, as the source is split into smaller more coherent regions, and the intensity from each section can be summed as in Abbe imaging. This is related to the approach of Adam and Lam for EMF and SOCS simulation [4].

In the current implementation of SP-KCPM, k-means clustering is used to cluster the source into the regions of a given size with minimum distance from the center of the clusters.

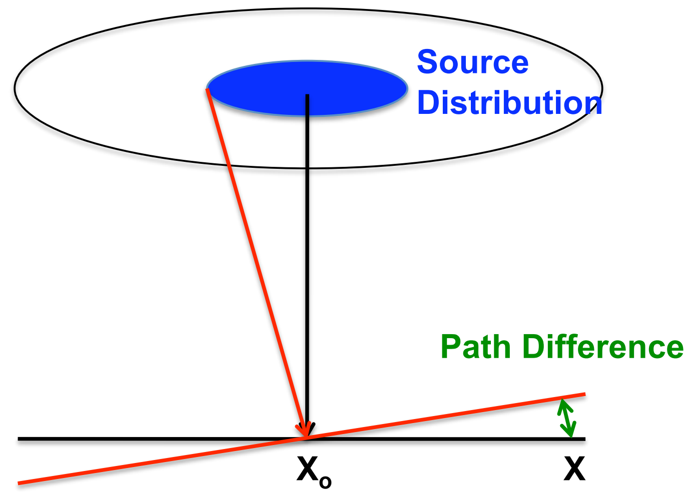

Figure 7.5: Off-axis illumination induces linear phase error. Two plane waves in phase at point X_o are out of phase at X

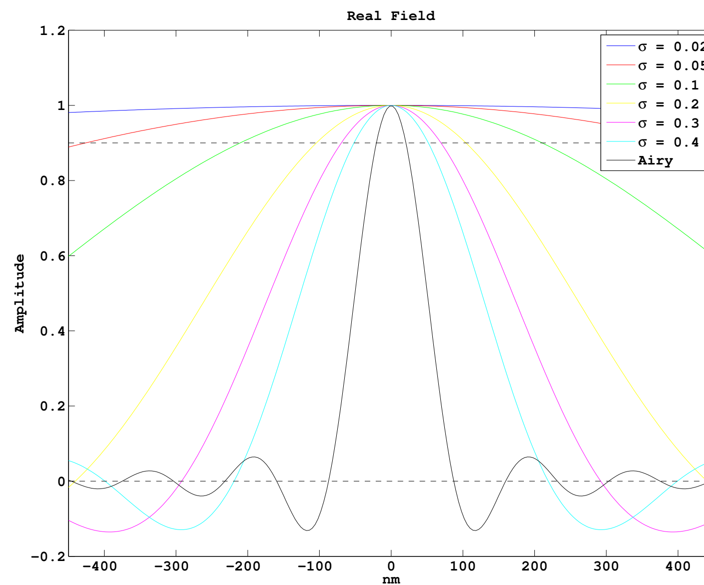

Figure 7.6: Point response for on-axis centered sources ranging from $\sigma = 0.02 to \sigma = 0.4$. Black curve describes Airy function for 1.35 NA pupil.

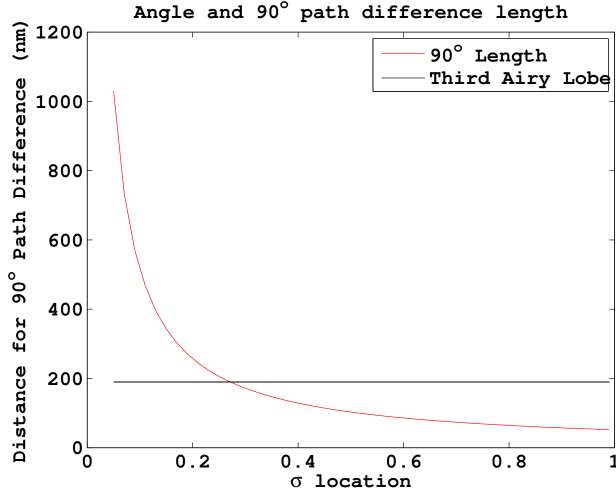

Figure 7.7: Plot of the range at which an off-axis pixel will be 90° out of phase with a reference on-axis incident wave.

The criteria can describe the spatial radius in the source plane or in a slightly more sophisticated version accounts for the actual angles of incidence for a given pixel distribution in σ space. Clustering can be performed iteratively, where the number of clusters is increased until a specified size of σ is reached for each subregion. Alternatively, it can be manually set to a specific number, and the k-means algorithm will do the best it can for the specified value. For example like dipole or quadrapole illumination, it might make sense to just use 2 and 4 kernels respectively. Something like annular or optimized pixelated sources are less intuitive, and can be treated by iteratively solving for a split configuration satisfying the coherence criteria. Unfortunately, splitting the source adds to the computational cycles for SP-KCPM, but as will be shown through the following examples, depending on the necessary accuracy tolerances, this step may not be needed.

7.3.1 Revisit Dipole

With source splitting available as a tool for correcting the errors caused by the source, we are now able to revisit the dipole example from 6.3.3. When simulating the full source, the correlation was about 0.9, and there were some odd looking trends in the intensity prediction caused by the cross-term normalization issue described in Section 7.2. Figure 7.8 shows a significant improvement achieved by breaking the two poles of the dipole into separate pattern matching calculations. Here, the same exact source was split as shown in Figure 7.8(b). This doubles the number of kernels required (and therefore computation time), but as shown by Figures 7.8(c) to 7.8(f), the accuracy improvements are significant. R^2 correlation is now improved from 0.9 to well over 0.99.

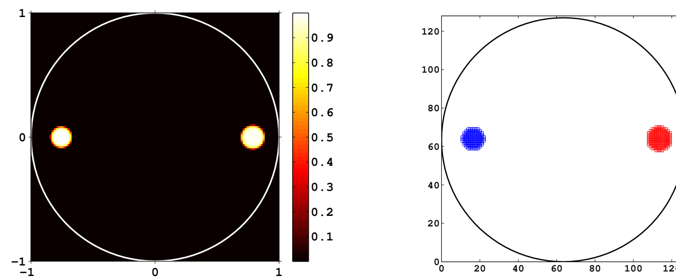

(a) Conventional Illumination, $\sigma = 0.15$

(b) Pupil function for 60nm defocus

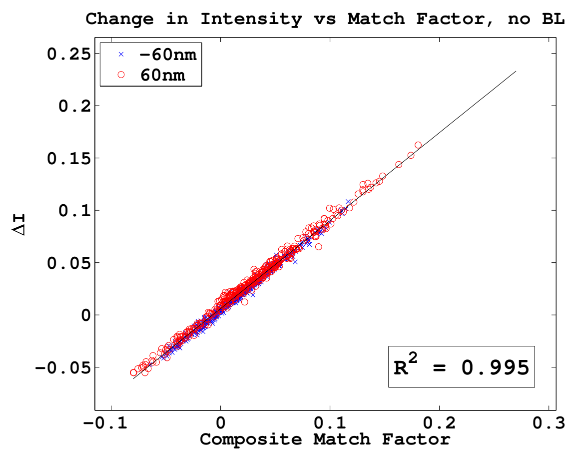

(c) ΔI vs. MF without boundary layers

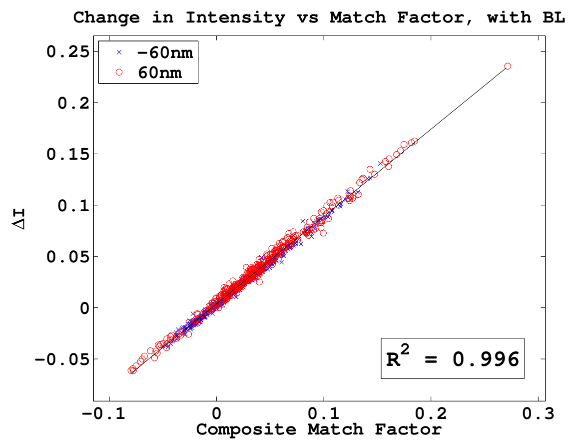

(d) ΔI vs. MF with boundary layers

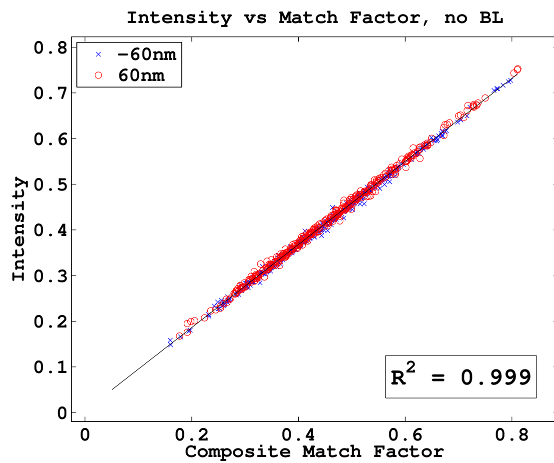

(e) I vs. MF without boundary layers

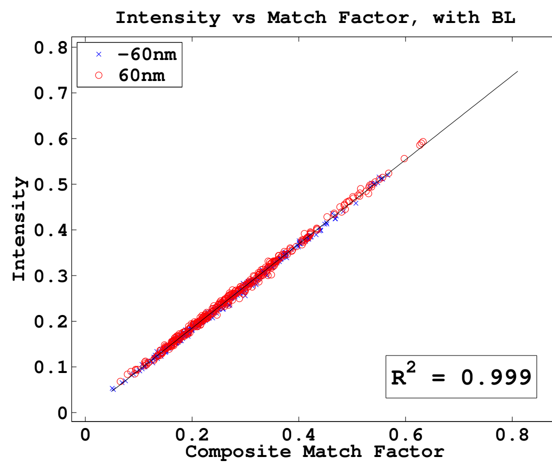

(f) I vs. MF with boundary layers

Figure 7.8: Correlation Data for Dipole Source Splitting Example

7.3.2 Annular Illumination: Breakdown vs Normal

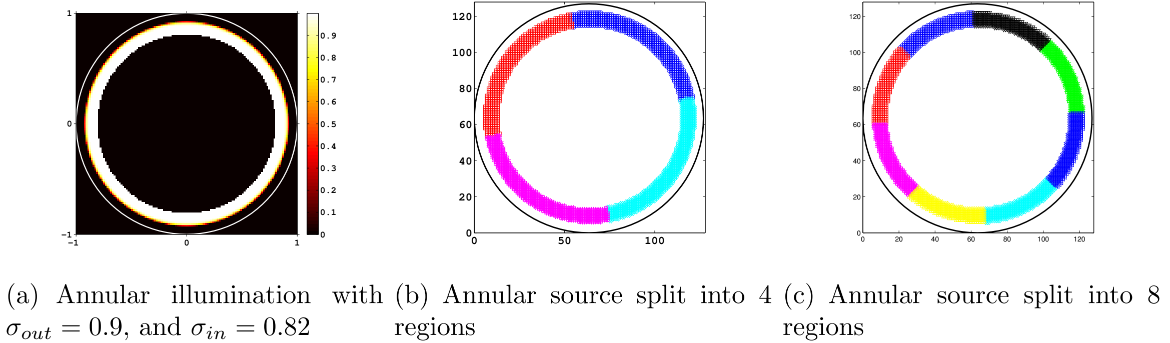

(a) Annular illumination with $\sigma_{out} = 0.9$, and $\sigma_{in} = 0.82$ (b) Annular source split into 4 regions (c) Annular source split into 8 regions

Figure 7.9: Simulation conditions for observing defocus with conventional small σ illumination

Now that one of the main culprits for inaccuracies in SP-KCPM has been discovered, we need to evaluate the capabilities of the source splitting solution. A second test for SP-KCPM is to look at modeling annular illumination, where the source splitting is not as straightforward as the previous dipole example. For this example, annular illumination with $\sigma_{out} = 0.9$, and $\sigma_{in} = 0.82$ was used. The source was split into four and eight regions to examine the accuracy vs. computation tradeoff of source splitting. Four and eight were chosen somewhat arbitrarily, and splitting can be performed with arbitrary distributions and numbers of splits. For full annular, two match patterns are needed to monitor one process change: one is for the initial field estimate ($E_{nominal}$) and the other is for the spillover Φ. In comparison, splitting the source into four regions requires four kernels for $E_{nominal}$ and four for Φ , therefore there are eight patterns for one focus level and twelve for two focus levels.

The comparison of KCPM to aerial image are shown in Figure 7.10. Only ΔI data is shown, but intensity prediction provides comparable accuracy. Comparing the full annular (Figures 7.10(a) and 7.10(b)) case to the split into four regions (Figures 7.10(c) and 7.10(d)), there is a significant increase in correlation from 0.91 to 0.99, already providing highly accurate matching. Going a step further, increasing to eight source regions (Figures 7.10(e) and 7.10(f)) increases correlation to 0.993 and 0.996 for the cases without and with BL corrections respectively. We could go further and split the source smaller, but even at four accuracy for just about any pattern matching application is achieved. Clearly a 4x or 8x increase in computation is undesirable, but if high accuracy is needed, source splitting has been demonstrated to be a useful tool. The necessity of source splitting is both source and application dependent.

7.4 Conclusions

With a clear understanding of partial coherent illumination in the SP-KCPM, combined with the source splitting solution, any source can be fully modeled. For $\sigma \leq 0.4$, correlation

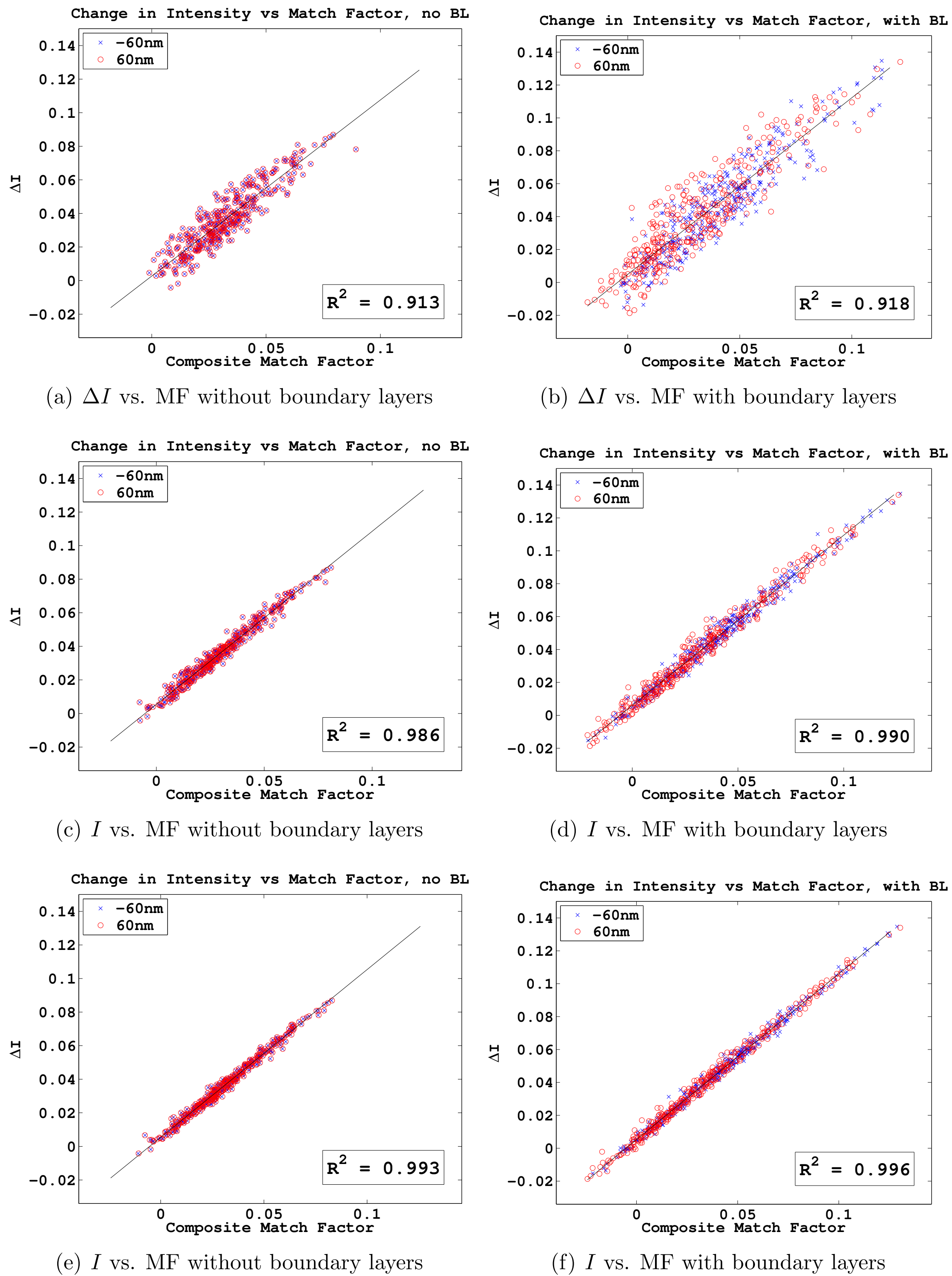

(a) ΔI vs. MF without boundary layers

(b) ΔI vs. MF with boundary layers

(c) I vs. MF without boundary layers

(d) I vs. MF with boundary layers

(e) I vs. MF without boundary layers

(f) I vs. MF with boundary layers

Figure 7.10: Correlation Data for Annular Source Splitting Example

is above 0.98 and off-axis incidence is modeled well all the way to the edge of the source plane. When using two kernels instead of one for dipole illumination, correlation increases from 0.90 to 0.99, though double the kernels means double the runtime. Annular illumination can be modeled with correlation of 0.99 using only four kernels.

Source splitting does introduce an additional runtime cost, but because of the overall computational speed, a 2, 4 or even 10x runtime increase still retains a speed advantage over full image calculation. The need for source splitting is both source an application dependent. For example, first cut accurate hotspot detection may only require correlation of 0.90, which is achieved with one kernel for annular. A more demanding optimization application would require four or even more kernels for accuracy above 0.99. The important result is that now there is a knob to increase accuracy when needed, which requires a minimal increase in computation.

Chapter 8

Applications of SP-KCPM

Source-Pupil Kernel Convolution with Pattern Matching is evaluated for applications at the cutting edge of lithography. Source-Mask Optimization (SMO) has emerged as a computational tool for pushing the limits of optical lithography. By grouping the mask-source determination as a co-optimization, it is possible to extend the process window, and resolve layouts which were too aggressive for traditional OPC. The resulting sources are often pixelated and have seemingly arbitrary distribution across the source plane. With source splitting, SP-KCPM is still highly accurate for SMO sources with correlation above 0.99.

Using hotspot detection, SP-KCPM has the ability to assess the impact of a SMO source on regions of the layout which cannot be optimized because of computational runtime. It can also be used to monitor changes made to a mask in an OPC or mask optimization environment.

8.1 Application: Evaluating SMO Source Effects on Non-optimized Layouts

SMO is typically applied to limited layout areas such as that of an aggressive SRAM cell. Ideally other layouts such as logic can be printed with the same source, otherwise an additional, and expensive, second exposure is required. Thus, there is a need for a fast and accurate way of checking the compatibility of a large non-optimized region with the optimized source. SP-KCPM is well suited for this purpose, and was evaluated for such an application.

Tachyon SMO (courtesy of ASML-Brion) [62] was used to produce source and mask solutions for the representative Metal 1 SRAM layer shown in Figure 8.1. The cell has minimum half-pitch of 45nm and 193nm illumination was used, along with NA = 1.35 immersion imaging. Optimized sources were generated for several mask configurations and tested on a generic test layout shown in Figure 6.6.

Figure 8.2(a) shows the source solution for a binary mask blank with clear field transmission (i.e. dark features). Figures 8.2(b) and (c) show plots of SP-KCPM match factor

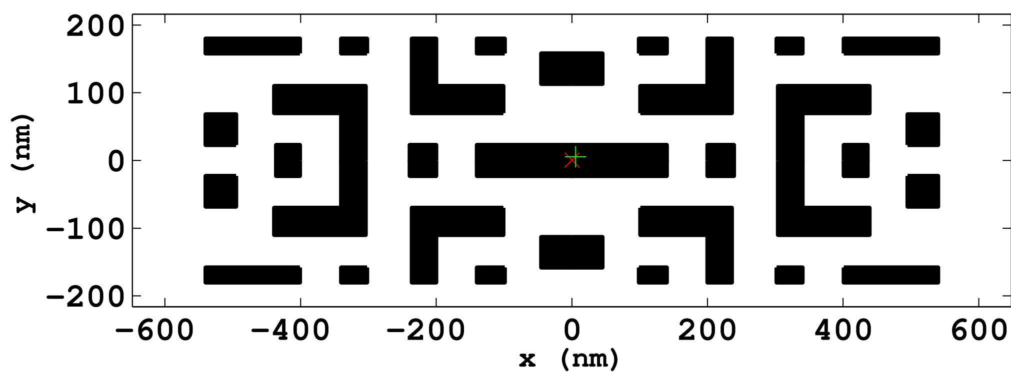

Figure 8.1: Metal 1 SRAM design target for SMO

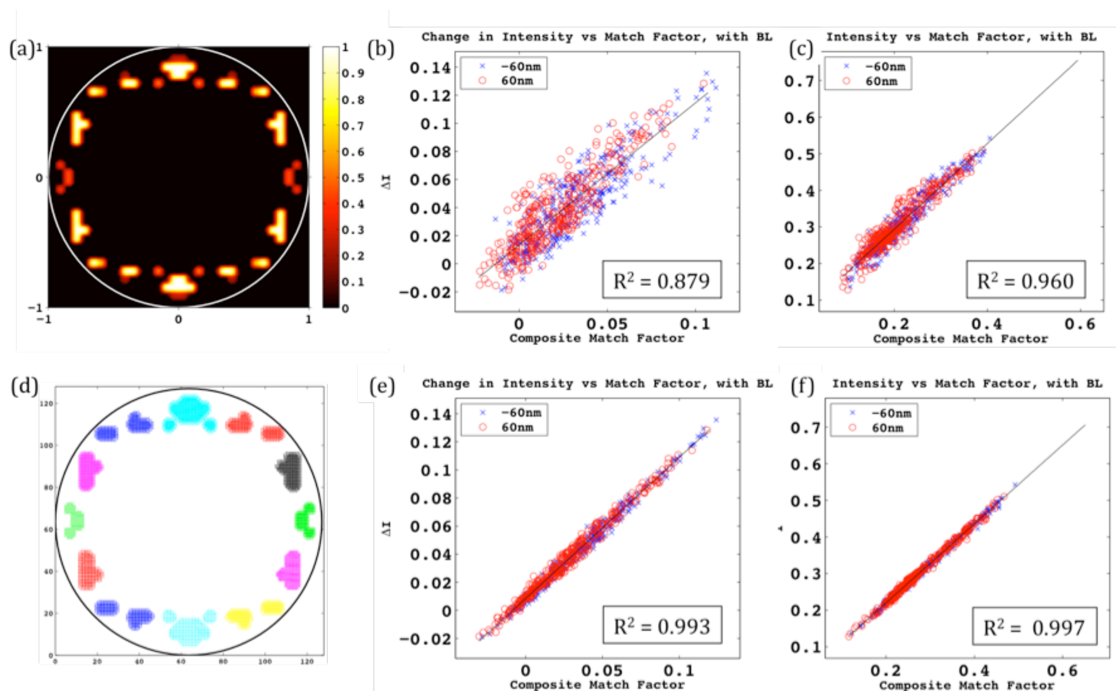

Figure 8.2: (a) SMO source solution for binary mask blank (b),(c) Change in intensity and Intensity vs. SP-KCPM with boundary layers for full source (d) SMO source split into 12 regions (e),(f) Change in intensity and Intensity vs. SP-KCPM with boundary layers for 12 kernels

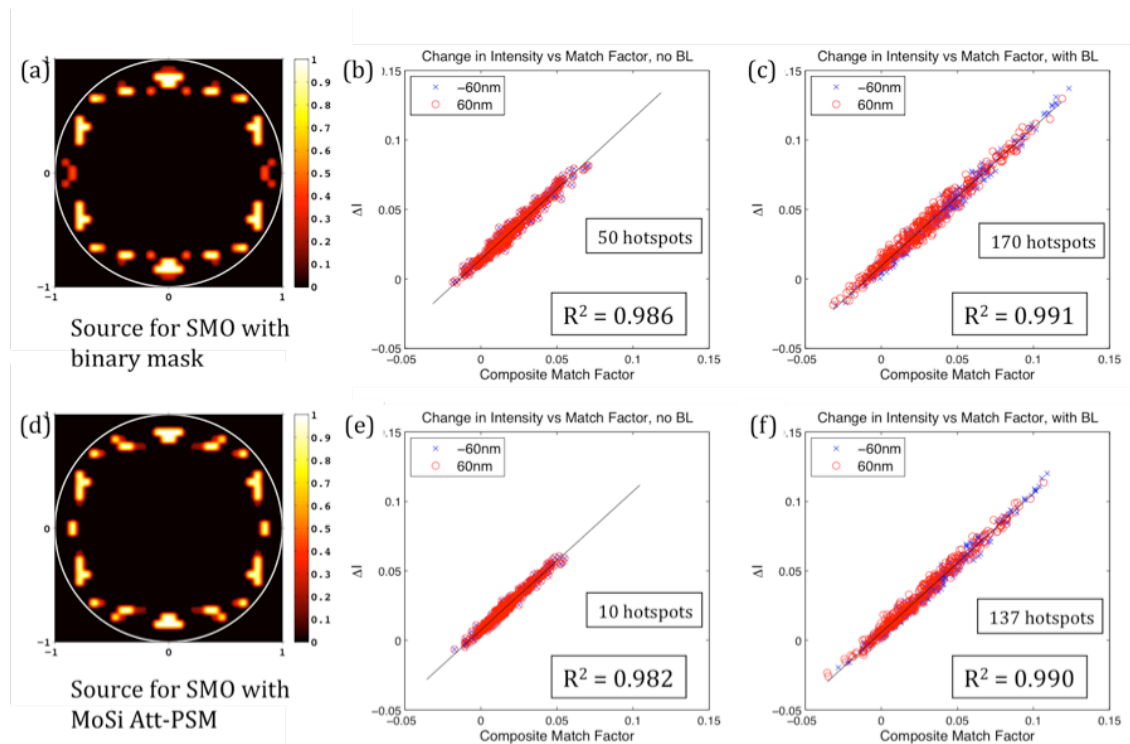

Figure 8.3: (a) SMO source solution for binary mask blank (b),(c) Change in intensity vs. SP-KCPM without and with boundary layers for 12 kernels (d) SMO source solution for attenuating (6.25%) PSM mask blank (e),(f) Change in intensity vs. SP-KCPM without and with boundary layers for 12 kernels

versus the same values calculated from full aerial image simulation for change in intensity and intensity respectively when using the full source for SP-KCPM. The R^2 correlation is 0.879 for predicting ΔI with defocus present. When looking at absolute intensity, SP-KCPM matches aerial imaging with R^2 correlation of 0.960. Intensity is predicted within 4% of the clear field value, which is useful in many applications, but there is still room for improvement.

For comparison, a source split scheme is shown in Figure 8.2(d), where the source is split into 12 regions, requiring 12 times the imaging kernels. This increases the computation time, but as shown in Figures 8.2(e) and (f), accuracy is increased as correlation for ΔI and I increase to 0.993 and 0.997. For the source split case, intensity is predicted within 1% of the clear field.

8.2 Source and Mask Blank Decision Making

With high accuracy demonstrated, we can explore potential applications for SP-KCPM. For this experiment, two solutions were chosen for comparison. The goal is to leverage the

speed of pattern matching to take a SMO source solution and scan for compatibility with other non-optimized regions of the layout. Figure 8.3(a) shows the source from a clear field binary mask optimization, while Figure 8.3(d) shows a source from optimization with a MoSi (6.25%) Attenuating phase shifting mask (Att-PSM) with clear field used as the mask blank. The pattern optimized is from Figure 8.1 and the image sensitivity was examined on the test pattern in Figure 6.6 using SP-KCPM with the source split into 12 regions.

Figures 8.3(b) and (c) show change in intensity through focus for the test pattern without and with boundary layers. For both cases the correlation remains more than 0.98. For an arbitrary tolerance of 5% change in intensity, out of a possible 720 points, the binary solution yields 50 hotspots with no EMF correction and 170 with. For the MoSi solution shown in Figures 8.3(d)-(f), 10 and 137 hotspots were detected for the two cases. For this case, the MoSi solution shows less sensitivity to focus and when solely looking at the focus effects on our test pattern offers better compatibility with the SMO solution than the binary version. In practice, the user can define what criteria determine a hotspot or other metric of compatibility. Because SP-KCPM can process large layouts rapidly, it is well suited for scans in this style to calculate the impact of a small optimized region over the rest of the layout.

8.3 Application: Tracking Image Quality with Mask Changes

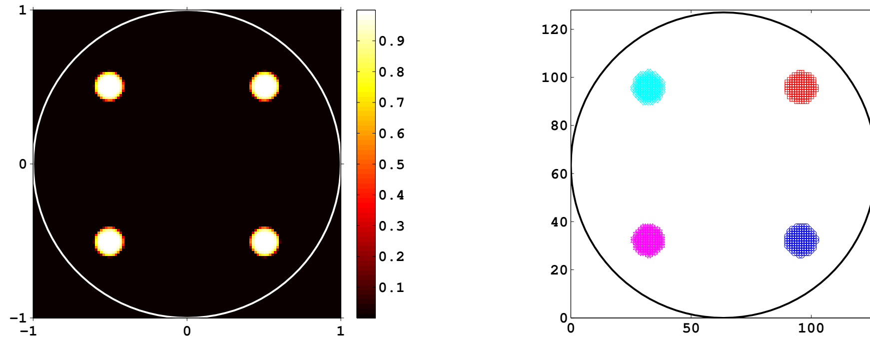

(a) Quadrapole source with $\sigma = 0.1$ poles (b) Quadrapole source split into four regions

Figure 8.4: Source Configurations for monitoring mask changes described in Figure 8.5

In addition to source decision on the back end of SMO, the improvements in accuracy of SP-KCPM enable real time application of image estimation even within an optimization routine. Optical proximity correction (OPC) is standard practice for pre-adjusting patterns to combat proximity effects and reduce aberration and focus sensitivity. Scanning a layout with SP-KCPM can be used for OPC style calculation and correction across large layouts.

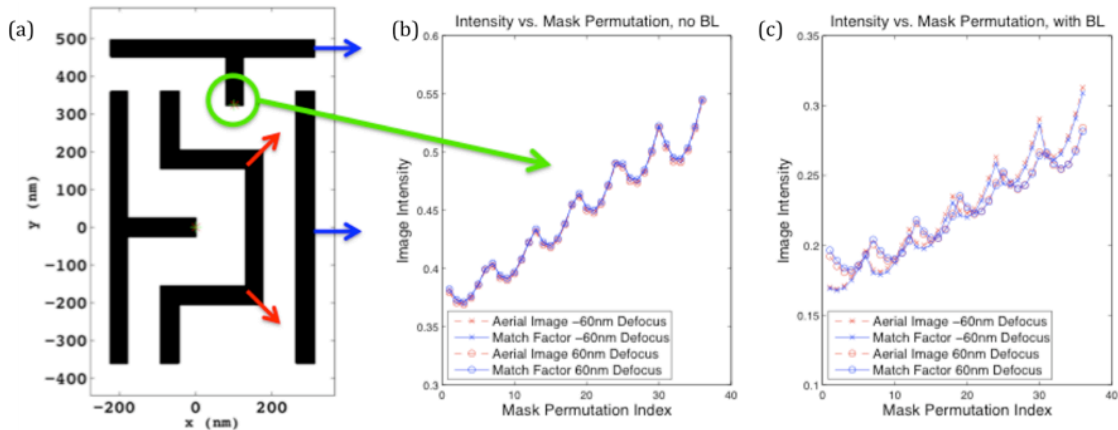

Figure 8.5: (a) 45nm layout altered into 36 permutations in six 8nm steps in directions of red and blue arrows (b),(c) Intensity vs. SP-KCPM for target point through 36 permutations without and with boundary layers

This example illustrates the ability and accuracy of SP-KCPM for monitoring focus effects in a changing mask. Here, a simple mask is shown in Figure 8.5(a). For this experiment, the mask was shifted at the arrows in 8nm steps in both x and y to create 36 mask permutations. Correlation and image values were calculated at 96 locations for a system with quadrapole illumination (Figure 8.4 with poles of size $\sigma = 0.1$, where $\sigma_x = \pm 0.5$ and $\sigma_y = \pm 0.5$. The source was split into 4 source regions for SP-KCPM.

Results for monitoring a line end in the center of the pattern are shown in Figures 8.5(b) and (c) without and with complex boundary layers. Here SP-KCPM is used to predict intensity at a given location. The red curve shows aerial image intensity values, while the blue are results from SP-KCPM. Additionally, x corresponds to negative defocus and o for positive defocus. Here we see very close agreement between aerial image and SP-KCPM as the red and blue curves are nearly overlapping. The intensity prediction is within 1%, relative to the clear field value. We also observe that for the binary case, as expected positive and negative defocus overlap because the mask is real leading to symmetry through focus. However for the boundary layer case, the imaginary transmission interacts with focus interaction leading to an asymmetry through focus [44]. SP-KCPM correctly captures this behavior.

8.4 Application: Tracking Image Quality with Mask Changes

The additional area where SP-KCPM offers an advantage is assisting SMO or MO by adding to the cost function for optimization. Because of the computational requirements in SMO, shortcuts are often taken to minimize runtime. It is standard practice to optimize for dose, focus, and mask error enhancement factor (MEEF). In the minimal case a

image calculation would take place three times for each condition (for example: negative defocus, nominal defocus, positive defocus). Simulating process corners would require nine calculations, but all combinations would be 27 calculations. Moving to five focus steps or adding additional lens aberrations would result in a massive computational increase. For this reason, the minimum types of variations (dose, focus, MEEF) are considered, often at process corners rather than at all combinations.

The speed of SP-KCPM creates an opportunity to add richness to optimized solutions by monitoring these often excluded process corners and including additional sources of variation such as electromagnetic edge effects and lens aberrations. SP-KCPM could easily be implemented as a flag to keep track of secondary effects which can reduce image quality, but perhaps not to the degree to merit the full computational burden of full image calculation. Depending on the accuracy constraints, SP-KCPM could be folded into existing algorithms as a piece of a cost function to be optimized, directly inserted into an optimization scheme.

8.5 Conclusions

With source splitting, R^2 correlation above 0.98 between aerial image and SP-KCPM was routinely achieved, and error within 1% of the clear-field value. For faster computation without source splitting, SP-KCPM still provides correlation > 0.85. Here the extremely fast scanning ability of pattern matching can evaluate the compatibility of a SMO source to a non-optimized layout to help determine which solution offers more compatibility with surrounding areas. SP-KCPM can also be used monitor real-time sensitivities to various process conditions to speed up the feedback loop to designers or to monitor effects which cannot be fully optimized due to runtime. Given the high degree of accuracy, SP-KCPM can be used for assisting OPC and enriching SMO or other optimization routines. In addition to focus, proximity effects, MEEF, dose and other process conditions can be monitored while minimizing the runtime consequences. The relationship between pre- and post-OPC layouts is dependent on the degree to which the mask changes. SP-KCPM can be used on pre- or post-OPC layouts, with or without boundary layers, and with any set of aberrations including, but not limited to defocus.

Chapter 9

Conclusions

This dissertation has addressed how to handle with the mismatch between a rigorous electromagnetic field (EMF) analysis and a thin mask model in a new paradigm that accurately analyzes full-chip behavior of aerial image quality in optical projection printing. Polarization aware boundary layer modeling offers a method for modeling transmission non-idealities to capture the important through focus consequences. Additional off-axis and cross-talk studies have shown that boundary layers can be used for general illumination schemes as long as edges are not interacting with one another. Once the topography behavior is described by generalized mask transmissions, Source-Pupil Kernel Convolution with Pattern Matching (SP-KCPM) can then be used to speed up image calculation. The result is the ability to compute electromagnetic field and other lithography variations orders of magnitude faster than conventional aerial imaging and thus enabling full-chip applications.

Two methodologies were presented for calculating boundary layer values for a given mask blank by looking at either 0th order transmission intensity or near-fields directly. It was shown that a simple grating based multiple duty cycle transmission experiment is capable of quantitatively determine both the magnitude and phase of mask edge effects. The phase errors induced by mask edges lead to an asymmetric behavior through focus, which when combined with polarization dependent effects can lead to significant loss in the process window. Though the actual magnitude is dependent on the mask blank and focus range, examples shown in Chapter 3 demonstrate reasonable scenarios where 40% of the process window is lost.

Observing the intensity of the rigorous mask diffraction orders was shown to be suitable for use in inexpensive, off-line approaches for calibrating mask edge behavior. Complex diffraction efficiencies go a step further to include the sign of the phase errors and cross-talk limitations. From the analysis of intensity and field errors, a MoSi attenuating phase shift mask was characterized in detail. Boundary layer values were about 20 nm in mask dimensions even for high off-axis illumination, making MoSi usable, but necessary to correct for edge errors. Adding a phase correction of 30x30 nm on exterior corners can be used to model line ends and jogs. Non-attenuating chromeless masks and complicated mask stacks such as $TaSiO_2$ showed significant electromagnetic errors. This sentiment has been supported by the abandonment of CPL technology for better behaving MoSi and thin binary

masks.

The big breakthrough in this dissertation is the development of SP-KCPM to leverage boundary layer modeling, and thus establishing a gapless flow from Maxwell's equations at a 10^4 speed-up in image calculation based on 40μs per kernel per match location metric. The development also contributed several important new capabilities for EMF modeling as well as general fast imaging. For example, moving to a pupil-based framework enables general imaging capabilities to simultaneously include defocus, zernike aberrations, measured aberrations, and potentially resist and polarization effects, while calculating their combined effects and relative strengths. Another benefit of switching to the pupil framework is that basic proximity effects are also included, removing the need for prior image calculation or placing an observation point on a given image contour. Imaging kernels are generated automatically, removing the need for a algebraic style perturbation approach for accounting for multiple effects. Incorporating complex mask transmissions brings edge effects into the pattern matching framework through boundary layers. The coherent source view in the new formulation, combined with source splitting brings a general source into the framework allowing for full flexibility for the source, mask, and pupil guaranteeing accuracy to impressive levels well those that were historically observed in KCPM. This enables even the most advanced optimized sources to be modeled accurately, and may be useful in helping other simulation tools model these sources.

The result of the source-pupil formulation combined with careful implementation considerations such as pattern size, gridding, normalization, and clustering lead to a very accurate system. For various examples with coherent, dipole, annular, quadrapole, and SMO sources correlation has been shown to be above 0.99. Additionally, effects of defocus, zernike aberrations, background aberrations, and asymmetric sources have all been shown to be accurate. This accuracy improvement unlocks myriad applications, some of which were explored in Chapter 8. SP-KCPM can be used with optimized sources to gather information about non-optimized layouts, facilitating decision making between different potential sources or mask blanks. By tracking a changing mask, SP-KCPM can assist optical proximity correction (OPC) or to enrich a SMO solution by investigating effects which are too computationally costly to calculate rigorously.

This dissertation created a seamless flow for including mask transmission errors via Maxwell's equations to modeling the through focus behavior of 1 billion transistors in a few hours. Despite the wide reach of the framework, the modular nature of many of the components developed along the way offer an immediate impact. Grating based field analysis can be used to quickly calibrate new mask materials and determine polarization dependent non-idealities. Source splitting, as described for SP-KCPM, has solved the long standing challenge of raising the correlation of KCPM with aerial image simulation from 0.90 to 0.99 with only a moderate reduction in speed. It can also be applied to general image simulation software, and can be smoothly integrated into existing fast methods like sum of coherent systems (SOCS). SP-KCPM itself offers a wide range of new features, such as proximity effects, M effects in the presence of N initial conditions, and full complex field interactions. With a demonstrated correlation of 0.99 with full image simulation, SP-KCPM is beneficial wherever fast imaging is needed, for both EMF and standard thin mask applications.

Bibliography

[1] K. Adam. Domain decomposition methods for the electromagnetic simulation of scattering from three-dimensional structures with applications in lithography. Ph.D. Dissertation, University of California, Berkeley, 2001.

[2] Konstantinos Adam. Modeling of electromagnetic effects from mask topography at full-chip scale. volume 5754, pages 498–505. SPIE, 2004.

[3] Konstantinos Adam, Shoji Hotta, and Andrew R. Neureuther. Characterization of phase defects in phase shift masks. volume 18, pages 3227–3231. AVS, 2000.

[4] Konstantinos Adam and Michael C. Lam. Hybrid hopkins-abbe method for modeling oblique angle mask effects in opc. volume 6924, page 69241E. SPIE, 2008.

[5] Konstantinos Adam and Andrew R. Neureuther. Simplified models for edge transitions in rigorous mask modeling. volume 4346, pages 331–344. SPIE, 2001.

[6] Konstantinos Adam and Andrew R. Neureuther. Domain decomposition methods for the rapid electromagnetic simulation of photomask scattering. *Journal of Microlithography, Microfabrication, and Microsystems*, 1(3):253–269, 2002.

[7] Konstantinos Adam and Andrew R. Neureuther. Methodology for accurate and rapid simulation of large arbitrary 2d layouts of advanced photomasks. volume 4562, pages 1051–1067. SPIE, 2002.

[8] Jaione Tirapu Azpiroz, Geoffrey W. Burr, Alan E. Rosenbluth, and Michael Hibbs. Massively-parallel fdtd simulations to address mask electromagnetic effects in hyper-na immersion lithography. volume 6924, page 69240Y. SPIE, 2008.

[9] Jaione Tirapu Azpiroz, Alan E. Rosenbluth, Ioana Graur, Geoffrey W. Burr, and Gustavo Villares. Isotropic treatment of emf effects in advanced photomasks. volume 7488, page 74882D. SPIE, 2009.

[10] Jaione Tirapu Azpiroz, Alan E. Rosenbluth, Kafai Lai, Carlos Fonseca, and Da Yang. Critical impact of mask electromagnetic effects on optical proximity corrections performance for 45 nm and beyond. *Journal of Vacuum Science and Technology B: Microelectronics and Nanometer Structures*, 25(1):164–168, 2007.

[11] Karen Badger, Yutaka Kodera, Emily Gallagher, and Mark Lawliss. Impact of the omog substrate on 32 nm mask opc inspectability, defect sensitivity, and mask design rule restrictions. volume 7122, page 71220A. SPIE, 2008.

[12] Min Bai, Lawrence S. Melvin III, Qiliang Yan, James P. Shiely, Bradley J. Falch, Chong-Cheng Fu, and Ruoping Wang. Approximation of three dimensional mask effects with two dimensional features. volume 5751, pages 446–454. SPIE, 2005.

[13] M. Born and E. Wolf. *Principles of Optics Second (revised) Edition*. Cambridge University Press, 1963.

[14] D. P. Ceperley. Simulation framework for electromagnetic effects in plasmonics, filter apertures, wafer scattering, grating mirrors, and nano-crystals. Ph.D. Dissertation, University of California, Berkeley, 2008.

[15] Daniel Ceperley, Andrew Neureuther, Marshall Miller, Michael Lieber, and Jeremy Kasdin. Stray-light sources from pupil mask edges and mitigation techniques for the tpf coronagraph. volume 6271, page 62711F. SPIE, 2006.

[16] Wen-Hao Cheng and Jeff Farnsworth. Control of polarization and apodization with film materials on photomasks and pellicles for high na imaging performance. volume 6520, page 65200O. SPIE, 2007.

[17] N. Cobb. Fast optical and process proximity correction algorithms for integrated circuit manufacturing. Ph.D. Dissertation, University of California, Berkeley, 1998.

[18] Nicolas B. Cobb, Avideh Zakhor, and Eugene A. Miloslavsky. Mathematical and cad framework for proximity correction. volume 2726, pages 208–222. SPIE, 1996.

[19] Vito Dai, Luigi Capodieci, Jie Yang, and Norma Rodriguez. Developing drc plus rules through 2d pattern extraction and clustering techniques. volume 7275, page 727517. SPIE, 2009.

[20] Andreas Erdmann. Topography effects and wave aberrations in advanced psm technology. volume 4346, pages 345–355. SPIE, 2001.

[21] Andreas Erdmann. Mask modeling in the low k[sub 1] and ultrahigh na regime: phase and polarization effects (invited paper). volume 5835, pages 69–81. SPIE, 2005.

[22] Andreas Erdmann and Christoph M. Friedrich. Rigorous diffraction analysis for future mask technology. volume 4000, pages 684–694. SPIE, 2000.

[23] C. M. Friedrich, L. Mader, A. Erdmann, S. List, R. L. Gordon, C. K. Kalus, U. A. Griesinger, R. Pforr, J. Mathuni, G. G. Ruhl, and W. Maurer. Optimizing edge topography of alternating phase-shift masks using rigorous mask modeling. In C. J. Progler, editor, *Society of Photo-Optical Instrumentation Engineers (SPIE) Conference Series*, volume 4000 of *Society of Photo-Optical Instrumentation Engineers (SPIE) Conference Series*, pages 1323–1335, July 2000.

[24] J. Gamelin, R. Guerrieri, and A. R. Neureuther. Exploration of scattering from topography with massively parallel computers. volume 7, pages 1984–1990. AVS, 1989.

[25] F. E. Gennari. Linking tcad and eda through pattern matching. Ph.D. Dissertation, University of California, Berkeley, 2004.

[26] F.E. Gennari and A.R. Neureuther. A pattern matching system for linking tcad and eda. In *Quality Electronic Design, 2004. Proceedings. 5th International Symposium on*, 2004.

[27] Frank E. Gennari and Andrew R. Neureuther. A pattern matching system for linking tcad and eda. *Quality Electronic Design, International Symposium on*, pages 165–170, 2004.

[28] Frank E. Gennari, Garth Robins, and Andrew R. Neureuther. Validation of the aberration-pattern-matching opc strategy. volume 4692, pages 444–453. SPIE, 2002.

[29] Bob Gleason and Wen-Hao Cheng. Optical properties of alternating phase-shifting masks. volume 6349, page 63491B. SPIE, 2006.

[30] Mentor Graphics, Accessed Dec 2010. `http://www.mentor.com/`.

[31] R. Guerrieri, K. Tadros, J. Gamelin, and A. R. Neureuther. Massively parallel algorithms for scattering in optical lithography. *IEEE Trans. CAD*, 10(9):1091–1100, 1991.

[32] Michael S. Hibbs and Timothy A. Brunner. Phase calibration for attenuating phase-shift masks. volume 6152, page 61521L. SPIE, 2006.

[33] Juliet Holwill, Gregory McIntyre, Wojtek Poppe, and Andrew R. Neureuther. Layout 'hot spots' for advancing optical technologies. volume 6154, page 61543M. SPIE, 2006.

[34] Juliet Holwill and Andrew R. Neureuther. Self-interferometric electrical image monitors. volume 6152, page 615215. SPIE, 2006.

[35] Shoji Hotta, Thomas V. Pistor, Konstantinos Adam, and Andrew R. Neureuther. Effects of shifter edge topography on through focus performance. volume 4186, pages 827–837. SPIE, 2001.

[36] Sangwook Kim, Young-Chang Kim, Sungsoo Suh, Sook Lee, Sungwoo Lee, Sukjoo Lee, Hanku Cho, Jootae Moon, Jonathan Cobb, and Sooryong Lee. Opc to account for thick mask effect using simplified boundary layer model. volume 6349, page 63493I. SPIE, 2006.

[37] Young-Chang Kim, Insung Kim, JeongGeun Park, Sangwook Kim, Sungsoo Suh, Yongjin Cheon, Sukjoo Lee, Junghyeon Lee, Chang-Jin Kang, Jootae Moon, Jonathan Cobb, and Sooryong Lee. Opc in memory-device patterns using boundary layer model for 3-dimensional mask topographic effect. volume 6520, page 65200T. SPIE, 2007.

[38] Michael Lam, Konstantinos Adam, and Andrew R. Neureuther. Domain decomposition methods for simulation of printing and inspection of phase defects. volume 5040, pages 1492–1501. SPIE, 2003.

[39] Ben Layet and Mohammad R. Taghizadeh. Electromagnetic analysis of fan-out gratings and diffractive cylindrical lens arrays by field stitching. *J. Opt. Soc. Am. A*, 14(7):1554–1561, Jul 1997.

[40] David Levenson, John S. Petersen, David J. Gerold, and Chris A. Mack. Phase phirst! an improved strong-psm paradigm. volume 4186, pages 395–404. SPIE, 2001.

[41] M. D. Levenson, N. S. Viswanathan, and R. A. Simpson. Improving resolution in photolithography with a phase-shifting mask. *IEEE Trans. Electr. Dev.*, pages 1828 – 1836, 29.

[42] Gregory McIntyre. Lithographic qualication of new absorbing mosi binary mask blank for the 32-nm node and beyond. volume 7122 of *SPIE Oral Presentation*, 2009.

[43] Gregory McIntyre, Andrew Neureuther, Steve Slonaker, Venu Vellanki, and Patrick Reynolds. Experimental verification of psm polarimetry: monitoring polarization at 193nm high-na with phase shift masks. volume 6154, page 61540D. SPIE, 2006.

[44] Marshal A. Miller and Andrew R. Neureuther. Analysis and modeling of photomask edge effects for 3d geometries and the effect on process window. volume 7274, page 727424. SPIE, 2009.

[45] Marshal A. Miller, Andrew R. Neureuther, Daniel P. Ceperley, Juliet Rubinstein, and Koji Kikuchi. Characterization and monitoring of photomask edge effects. volume 6730, page 67301U. SPIE, 2007.

[46] Marshal A. Miller, Kenji Yamazoe, and Andrew R. Neureuther. Extensions of boundary layer modeling of photomask topography effects to fast-cad using pattern matching. volume 7488, page 74883H. SPIE, 2009.

[47] W.G. Oldham, S.N. Nandgaonkar, A.R. Neureuther, and M.; O'Toole. A general simulator for vlsi lithography and etching processes: Part iapplication to projection lithography. *IEEE Trans. on Electron Devices*, 26(4):717–722, 1979.

[48] M. M. O'Toole. Simulation of optically formed image profiles in positive photoresist. Ph.D. Dissertation, University of California, Berkeley, 1979.

[49] C. Pierrat, A. Wong, and S. Vaidya. Phase-shifting mask topography effects on lithographic image quality. In *Electron Devices Meeting, 1992. Technical Digest., International*, pages 53 –56, December 1992.

[50] Christophe Pierrat. Proximity effects in alternating aperture phase-shifting masks. volume 4186, pages 325–335. SPIE, 2001.

[51] Christophe Pierrat and Alfred K. K. Wong. Mef revisited: low k[sub 1] effects versus mask topography effects. volume 5040, pages 193–202. SPIE, 2003.

[52] T. Pistor. Electromagnetic simulation and modeling with applications in lithography. Ph.D. Dissertation, University of California, Berkeley, 2001.

[53] Garth Robins and Andrew R. Neureuther. Illumination, mask, and tool effects on pattern and probe-based aberration monitors. volume 4691, pages 138–147. SPIE, 2002.

[54] Garth C. Robins. Interferometric pattern and probe-based aberration monitors. Ph.D. Dissertation, University of California, Berkeley, 2005.

[55] Garth C. Robins, Mircea Dusa, Bernd Geh, and Andrew Neureuther. Interferometric-probe aberration monitors: aerial image and in-resist performance. volume 5256, pages 309–317. SPIE, 2003.

[56] Garth C. Robins and Andrew R. Neureuther. Experimental assessment of pattern and-probe aberration monitors. volume 5040, pages 1420–1431. SPIE, 2003.

[57] Juliet Rubinstein and Andrew R. Neureuther. Post-decomposition assessment of double patterning layouts. volume 6924, page 69240O. SPIE, 2008.

[58] Juliet Rubinstein and Andrew R. Neureuther. Through-focus pattern matching applied to double patterning. volume 7274, page 72741A. SPIE, 2009.

[59] Juliet A. Rubinstein. Pattern matching for advanced lithographic technologies. Ph.D. Dissertation, University of California, Berkeley, 2010.

[60] Johannes Ruoff, Jens Timo Neumann, Emil Schmitt-Weaver, Eelco van Setten, Nicolas le Masson, Chris Progler, and Bernd Geh. Polarization-induced astigmatism caused by topographic masks. volume 6730, page 67301T. SPIE, 2007.

[61] R. R. Shannon and J. C. Wyant. *Applied Optics and Optical Engineering*. Academic Press Inc., 1992.

[62] Robert Socha, Tejas Jhaveri, Mircea Dusa, Xiaofeng Liu, Luoqi Chen, Stephen Hsu, Zhipan Li, and Andrzej J. Strojwas. Design compliant source mask optimization (smo). volume 7748, page 77480T. SPIE, 2010.

[63] A. Taflove and S. C. Hagness. *Computational Electrodynamics - The finite-difference-time-domain method*. Artech House, 1990.

[64] Panoramic Technologies, Accessed Dec 2010. `http://www.panoramictech.com/`.

[65] J. Tirapu-Azpiroz. Analysis and modeling of photomask near-fields in sub-wavelength deep ultraviolet lithography with optical proximity corrections. Ph.D. Dissertation, University of California, Los Angeles, 2004.

[66] Jaione Tirapu-Azpiroz and Eli Yablonovitch. Incorporating mask topography edge diffraction in photolithography simulations. *J. Opt. Soc. Am. A*, 23(4):821–828, Apr 2006.

[67] K. Toh. Two-dimensional images with effects of lens aberrations in optical lithography. M.S. Thesis, University of California, Berkeley, 1988.

[68] Lynn T. Wang, Anthony Yeh, Lilly Kem, and Andrew R. Neureuther. Illustration of illumination effects on proximity, focus spillover, and design rules. volume 7275, page 72750B. SPIE, 2009.

[69] A. K. Wong. Rigorous three-dimensional time-domain finite differend electromagnetic simulation. Ph.D. Dissertation, University of California, Berkeley, 1994.

[70] A. K. Wong and A. R. Neureuther. Massively parallel algorithms for scattering in optical lithography. *IEEE Trans. on Semiconductor Manufacturing*, 8(4):419–431, 1995.

[71] A.K. Wong and A.R. Neureuther. Mask topography effects in projection printing of phase-shifting masks. *Electron Devices, IEEE Transactions on*, 41(6):895 –902, June 1994.

[72] Alfred K. K. Wong and Andrew R. Neureuther. Polarization effects in mask transmission. volume 1674, pages 193–200. SPIE, 1992.

[73] Kenji Yamazoe. Computation theory of partially coherent imaging by stacked pupil shift matrix. *J. Opt. Soc. Am. A*, 25(12):3111–3119, Dec 2008.

[74] Kenji Yamazoe. Fast fine-pixel aerial image calculation in partially coherent imaging by matrix representation of modified hopkins equation. *Appl. Opt.*, 49(20):3909–3915, Jul 2010.

[75] Pei yang Yan. Understanding bossung curve asymmetry and focus shift effect in euv lithography. volume 4562, pages 279–287. SPIE, 2002.

[76] K. Yee. Numerical solution of initial boundary value problems involving maxwell's equations in isotropic media. *IEEE Trans. Ant. Propag.*, 1463:302–307, 1966.

[77] C.-M. Yuan. Calculation of one-dimensional lithographic aerial images using the vector theory. *Electron Devices, IEEE Transactions on*, 40(9):1604 –1613, September 1993.